1-1-1988

The distribution of the interstellar medium in the Scd galaxy NGC 6946 and in a sample of dwarf irregular galaxies.

Linda Tacconi
University of Massachusetts Amherst

THE DISTRIBUTION OF THE INTERSTELLAR MEDIUM IN THE Scd GALAXY NGC 6946 AND IN A SAMPLE OF DWARF IRREGULAR GALAXIES

A Dissertation Presented

by

LINDA JEAN TACCONI-GARMAN

Submitted to the Graduate School of the
University of Massachusetts in partial fulfillment
of the requirements for the degree of

DOCTOR OF PHILOSOPHY

May 1988

Department of Physics and Astronomy

The Distribution of the Interstellar Medium
in the Scd Galaxy NGC 6946 and
in a Sample of Dwarf Irregular Galaxies

A Dissertation Presented

by

Linda Jean Tacconi-Garman

Approved as to style and content by:

Judith S. Young, Chairperson of Committee

Suzan Edwards, Member

John Kwan, Member

Stephen E. Strom, Member

Robert V. Krotkov, Outside Member

Robert B. Hallock, Department Head
Department of Physics and Astronomy

ACKNOWLEDGEMENTS

Reflecting back on my years at UMass and FCRAO, I realize that one person has influenced my career more than any other, and that person is my advisor, Judy Young. From the time I started working with her during my senior year at Smith, she has always been there, providing advice and support every step of the way through my graduate career. She has allowed me the freedom and independence to pursue my own scientific interests, while offering guidance to help smooth out some of the rough edges. In this way and in many others, I consider Judy to be the ideal advisor. Her enthusiasm for astronomy and galaxies in particular is unsurpassed and has been an inspiration to me. Judy also provided me with financial support at a critical time, my last six months as a graduate student, so that I could focus my attention on finishing my thesis.

I would also like to thank the rest of my thesis committee, Steve Strom, John Kwan, Suzan Edwards, Bob Krotkov, and Jay Gallagher, for helpful comments and discussions on earlier drafts of this thesis. Steve Strom has been another supportive and encouraging force throughout my years at UMass. He has taught me much about galactic evolution, in particular the evolution of dwarf galaxies, from an optical observers perspective.

Graduate students at UMass have a unique opportunity to undertake large observing projects with one of the world's most sensitive millimeter wave radio telescopes, the FCRAO 14-meter antenna. I feel extremely fortunate to have been one

of those graduate students, and am grateful to Bill Irvine, the director of FCRAO, and the rest of the telescope scheduling committee for giving me the several hundred hours of observing time that were necessary to complete the CO observations for this thesis. I would also like to thank FCRAO for supporting me for many years as a research assistant. The staff at FCRAO has always been helpful and have made sure that the telescope and the observatory were kept in top working condition. Jackie Golonka, Sally Rule, and Denise Kuzmescus should be canonized for their ability to handle logistical problems efficiently, while remaining calm and amazingly cheerful. To them, I wish nothing but the best, and a world full of chocolate and blonde brownies.

There are also many scientists, both at UMass and elsewhere, who have contributed to this thesis in some manner. My husband, Lowell, Judy Young, and Jeff Kenney all helped with the CO observations of NGC 6946, while the FCRAO extragalactic survey crew helped with the observations of the dwarf galaxies. The scientists and staff at the VLA were very helpful in the calibration and reduction of the HI data and particular thanks in that regard go to Peggy Perley, Rick Perley, and Jacqueline van Gorkom. I also acknowledge Sigma Xi for a grant-in-Aid of Research, which provided partial support for a trip to the VLA to reduce the HI data. Debbie and Bruce Elmegreen kindly gave us access to B- and I-band images of NGC 6946. Very useful discussions were had with Nick Scoville, Jacqueline van Gorkom, Jeff Kenney, Bill Waller, Harley Thronson, Bruce Elmegreen, and Paul Viscuso.

I was able to produce this thesis in a (reasonably) trouble-free manner thanks to Susan Kleinmann. She kindly allowed me access to her computer to typeset this document. She also spent many hours in the last few months working to revive a sick printer daemon such that I could print the thesis in a timely fashion. I am very grateful to her for her generosity and patience with me in my use of her system.

During my graduate years at UMass, I have made many close friends who are going to be sorely missed. For all her emotional, as well as scientific, support I again thank Judy. Bev Smith, Sue Madden, and Carolyn Jordan did their best to get me to leave my desk and become a weight lifter. Sue Madden, Pat Knezek, and Sylvie Cabrit deserve particular recognition for their many hours of help with packing, moving, and other such trivial details, and for being the best of friends during the final crunch (and at other times too!). If I listed all of the people that I've met here who have provided moral support, I would need at least another five pages, so I will say thanks to everyone. I will miss you all!

I also thank my very special friend, Alison, for always presenting the lighter side of life and for being a constant source of encouragement during my undergraduate and graduate years.

Many thanks go to my family members: to my sister, Lorraine and brother-in-law, Dennis, for always being there and ready to listen; to my brother, Bo, for lending a sympathetic ear throughout the years; to my niece, Gina, for bringing so much laughter into all our lives; and to my grandparents, for providing the example that with

work and determination, almost anything is possible. Special thanks go to my parents for continuing with my grandparents' example and for their never ending supply of love and support (and cars) which have allowed me the luxury of staying in school for 22 years.

Finally, my infinite love and gratitude go to my husband, Lowell. Not only has he been incredibly loving and supportive during the past 4 years, he has also spent a great deal of his time (while he was also trying to write a thesis) critiquing and typing this work, and also checking it for my famous 2 AM grammar. For all his love and faith in me all during graduate school, it is to him that I dedicate this thesis.

ABSTRACT

THE DISTRIBUTION OF THE INTERSTELLAR MEDIUM
IN THE Scd GALAXY NGC 6946 AND
IN A SAMPLE OF DWARF IRREGULAR GALAXIES

May 1988

Linda Jean Tacconi-Garman, A.B., Smith College

Ph. D., University of Massachusetts

Directed by: Professor Judith S. Young

We have compared the atomic and molecular hydrogen distributions in the spiral galaxy NGC 6946 and in 15 dwarf irregular galaxies. We have made observations of the CO J = 1→0 transition to obtain a fully sampled map to a radius of 10 kpc in NGC 6946, using the 14-meter telescope of the Five College Radio Astronomy Observatory, and have also completely mapped the 21-cm line of neutral hydrogen with the Very Large Array. We have also made CO observations at FCRAO in 15 dwarf irregular galaxies spanning a wide range of infrared luminosity and color.

In NGC 6946 the CO and HI maps were used to investigate the radial and azimuthal variations in the atomic and molecular gas. The H_2 mass is found to dominate the ISM in the inner disk of this galaxy. The H_2, Hα, radio continuum, and blue light radial profiles are found to be centrally peaked with exponential falloffs, while the HI distribution is much flatter, with a central depression. We infer a constant efficiency of star formation with radius in NGC 6946 and suggest that HI plays only a passive role in the star formation process of this galaxy.

Spiral arm enhancements in the H_2 surface densities, Hα surface brightnesses, and $\sigma(H_2)/\mu(H\alpha)$ ratios are observed. The presence of these arm enhancements, as well as enhancements in the gas surface densities in interarm regions is consistent with a picture in which cloud-cloud collisions play an important role in the star formation process in NGC 6946. An observed strong increase in the $\mu(H\alpha)/\sigma(H_2)$ ratio with increasing arm amplitude indicates that the massive star formation efficiency is a sensitive function of spiral arm strength.

For the dwarf galaxies, high observed L_{IR}/L_{CO} ratios in the blue systems are indicative of a present burst of star formation, while the red systems exhibit low L_{IR}/L_{CO} ratios. The $M(H_2)/M(HI)$ ratios are smaller in the blue dwarfs than in either the red systems or in NGC 6946. We suggest that a low metallicity, low volume density, and an increased UV radiation field are responsible for the low H_2/HI ratios in active dwarf galaxies.

TABLE OF CONTENTS

LIST OF TABLES

LIST OF FIGURES

CHAPTER 1

INTRODUCTION

1.1 Preview

One of the critical elements in understanding the star formation history of a galaxy is a knowledge of the molecular gas distribution, since molecular clouds are the birthplaces of new stars. Until recently, however, observations of 21-cm neutral hydrogen and Hα emission have been the sole means of determining the amount of gas available for star formation, the gas depletion timescales, and the star formation rates and efficiencies in other galaxies without any information about the molecular gas contents. With the advent of sensitive millimeter receivers and large antennas, it is now possible to probe the molecular component of the interstellar medium (ISM) in a galaxy through observations of the $J = 1 \rightarrow 0$ rotational transition of ^{12}CO.

Within the past decade or so there have been many observing programs of the CO contents of external galaxies, with a sample of them listed here.(*e.g.* Rickard *et al.* 1977; Stark 1979; Young and Scoville 1982a, b; Verter 1983; Young *et al.* 1986a; Sanders *et al.* 1986; Kenney 1987; and Kenney and Young 1987; Stark, Elmegreen and Chance 1987). These programs and others have begun to provide valuable insight into the global CO properties of galaxies as a function of morphological type, galaxy environment, and luminosity. Furthermore, interferometric and large single dish observations have provided clues to the smaller scale structures of the molecular gas such as the presence of central molecular bars and molecular spiral structure

(*e.g.* Lo *et al.* 1984; Ball *et al.* 1985; Rydbeck, Hjalmarsen, and Rydbeck 1985; Lo *et al.* 1987; Sofue *et al.* 1987; see also references in Peimbert and Jugaku 1987).

Many important questions have been asked and addressed in studies of the CO contents of galaxies. Among these are:

• What is the radial distribution of CO in galaxies and how does it compare with the distributions of optical light and atomic gas?

• What is the total CO luminosity in a galaxy as a function of morphological type, galaxy mass, and galaxy environment, and how does it compare with the Hα, blue, and far infrared luminosities?

• How much mass is available to be incorporated into stars in galaxies of different morphological types?

• What is the star formation efficiency in individual galaxies, and how does it vary from galaxy to galaxy?

• What are the timescales for depletion of the gas based on the total mass available for star formation and star formation rates, assuming no infall of material?

1.2 Motivation

Because of the limitations in sensitivity and observing time, most studies of the CO contents of galaxies have consisted of observations along one or two position angles, and the above questions have been addressed with CO distributions and luminosities inferred from these data. Very few fully sampled ^{12}CO maps of galaxies covering a large fraction of the optical disk have been published to date, although they

have been made in M82 and M51 (*cf.* Young and Scoville 1984; Rydbeck, Hjalmarson, and Rydbeck 1985; Lord 1987; and Lord and Young 1987). Measuring the total distribution of molecular material in a galaxy is necessary for discerning any azimuthal structures (*e.g.* spiral arm-interarm contrasts) and radial fluctuations. Lord (1987) and Lord and Young (1987) have made one of the few detailed studies of the CO contents of a galaxy and have found a high Hα surface brightness to gas surface density ratio on the spiral arms in the grand design spiral galaxy, M51.

It is also critical to determine the atomic gas distribution on size scales similar to that of the molecular gas to gain insight into the role of HI in the star formation process. With the advent of sensitive aperture synthesis telescopes this is now possible, and a wealth of observations have been made using the Westerbork and VLA telescopes (see *e.g.* Bosma 1981a, b; Wevers 1984; van Driel 1987; and Athanassoula 1983 and references cited within these). While the traditional view has been that HI is the medium out of which molecular clouds form (Seiden 1983; Tacconi and Young 1986), it has been suggested that the HI emission in galaxies arises from the envelopes of molecular cloud cores where the molecules have been dissociated by the ambient UV radiation field (Shaya and Federman 1987).

In this thesis we present one of the few studies of the detailed distributions of both the molecular and atomic components of the ISM within an individual galaxy. To address many of the previously mentioned issues, we have completely mapped the CO contents of the inner 6'.75 of the nearly face-on, luminous Scd galaxy NGC 6946 at

45" resolution, and have also fully mapped the HI distribution at similar resolution. We wish to determine the relative amounts of molecular and atomic gas as a function of radius and azimuth to gain insight into the roles that the atomic and molecular gas have each played in the star formation history of this galaxy. Additionally, from comparisons of the molecular gas surface densities with Hα fluxes we will determine the constancy of the massive star formation efficiency on 2 kpc scales in this galaxy. We also compare the azimuthal variations of the ionized, atomic, and molecular gas with those of the optical surface brightnesses to determine the degree of confinement of the ISM to the spiral arms.

In addition to determining the detailed distribution of the ISM within individual galaxies, it is also critical to determine the total amount of molecular and atomic gas in galaxies of a wide range of masses to examine whether the star formation processes in a galaxy depend on its mass. Most of the studies of the CO contents of galaxies have concentrated on luminous high surface brightness spiral galaxies, with relatively little attention given to low luminosity, low mass objects. Dwarf galaxies may be the most abundant type of galaxy in the universe (de Vaucouleurs 1975), however, so it is important to understand the star formation histories of these systems. Moreover, dwarf irregular galaxies are known to contain considerable amounts of HI (*e.g.* Fisher and Tully 1975; Thuan and Seitzer 1979) and are often found to be very actively forming stars at the present epoch (*e.g.* Hunter 1982; Hunter, Gallagher and Rautenkranz 1982; Thuan and Martin 1983). Their colors span a wide range from red,

low surface brightness objects to extremely blue, compact galaxies. Their extreme metal deficiencies have led investigators to suggest that either the blue systems are relatively young, and have recently formed out of protogalactic gas clouds, or that the class of irregular dwarfs as a whole undergo cycles of intermittent bursts of star formation, followed by periods of quiescency during their lifetimes. In this thesis, we have chosen to study the CO contents of a sample of dwarf irregular galaxies spanning a wide range in color and star formation activity to gain insight into whether the amount of molecular gas present in these systems is correlated with the amount of current massive star formation.

Thus far, studies of the CO contents of both giant and dwarf irregular galaxies have shown these systems to be extremely CO deficient relative to more massive spiral galaxies, as determined by their CO/blue and CO/HI ratios (Elmegreen, Elmegreen, and Morris 1980; Young, Gallagher, and Hunter 1984; Tacconi and Young 1985; Israel *et al.* 1986; Israel and Burton 1986; Henkel, Wouterloot and Bally 1986; and Thronson and Bally 1987). To account for the paucity of CO emission it has been suggested that the metal deficiency of all irregular galaxies has resulted in the CO deficiency, but that the molecular hydrogen is not deficient in these systems (*e.g.* Israel *et al.* 1986), although Dickman *et al.* (1986) show that the CO luminosity of a galaxy does not depend directly on metallicity, but on the mean gas temperature. Other studies have suggested that low mass systems such as irregular galaxies do not form a large supply of molecular gas (*e.g.* Hunter, Gallagher, and Rautenkranz 1982;

Hunter and Gallagher 1985), although these authors have not searched for molecular gas in these systems. In a large scale study of the CO properties of spiral galaxies in the Virgo cluster, Kenney (1987) has discovered a class of CO-poor, HI-rich, low mass spirals with high massive star formation rates. He suggests that since both the HI-rich, CO-poor Virgo spirals and dwarf irregular galaxies are low mass systems, weak CO emission may be related to galaxy mass, and that the weak emission is indicative of an actual dearth of molecular gas.

The CO and IR properties of a sample of dwarf irregular galaxies studied in this thesis are consistent with a picture of star formation where the blue, compact galaxies are presently undergoing a burst of star formation, while the red systems are currently in a pre-burst state. Furthermore, we argue that the differences in the inferred relative amounts of molecular and atomic gas in the dwarf irregular galaxies and the more massive spiral galaxy NGC 6946 may be due to a decrease in the gas volume density and an increase in the ambient radiation field in the dwarf systems, thereby resulting in thick atomic hydrogen envelopes around molecular cloud cores (Shaya and Federman 1987).

1.3 Summary of Chapters

The complete HI map of NGC 6946 is presented in Chapter 2. Detectable HI emission is observed out to a radius of 30', with HI clumps found on a 2 kpc scale, and with HI spiral structure being most evident in the outer disk of the galaxy. The HI mean velocity field is also discussed; the kinematic major axis is found to change in

position angle by ~ 45° from the center to a radius of 2'. This is a characteristic which is often found in barred spiral galaxies and is consistent with the presence of the central CO bar discovered by Ball *et al.* (1985).

Some global properties of NGC 6946 are also discussed in Chapter 2. The azimuthally averaged radial distributions of HI, CO, Hα, radio continuum, B- and I-band emission are compared. Of these, the HI distribution is the only one which is decidedly different from the rest and we put forth that the atomic gas component plays only a passive role in the evolution of high luminosity, late type spiral galaxies such as NGC 6946.

In Chapter 3, a fully sampled ^{12}CO map of the inner 6'.75 of NGC 6946 is presented. From these data we infer H_2 masses and obtain a non-averaged CO radial distribution. In addition to CO integrated intensities, HI integrated fluxes, and B- and I-band surface brightnesses are all determined in 45" gaussian weighted apertures at the positions where CO observations were made[1] .

A detailed comparison of the molecular and atomic components of the ISM in NGC 6946 is presented in Chapter 4. First, we make global comparisons of the atomic and molecular gas surface densities with Hα, blue, and near-infrared surface brightnesses. The molecular gas is found to correlate well with the Hα, B- and I-band surface brightnesses, while no correlation is seen between the atomic gas and any of

1. B- and I-band data were kindly provided by Drs. B. Elmegreen and D. Elmegreen.

the three optical surface brightnesses. The variations of the $\mu(H\alpha)/\sigma(H_2)$ and $\sigma(H_2)/\sigma(HI)$ ratios with radius are then discussed. There are no radial trends in the $\mu(H\alpha)/\sigma(H_2)$ ratio, indicating that the massive star formation efficiency is constant with radius, while $\sigma(H_2)/\sigma(HI)$ is found to decrease sharply with radius.

A very important aspect of this study of the atomic and molecular components of the ISM in NGC 6946 is the comparison of the azimuthal variations of the gas surface densities with the optical spiral structure. The azimuthal variations of the H_2 and HI surface densities, B-, I-band, and Hα surface brightnesses and various ratios of these quantities is presented in Chapter 4. The spiral structure is observed to be quite complicated in NGC 6946 with well defined optical spiral arms in the northeast regions of the galaxy, and poorly defined spiral structure in the southwest. Correspondingly, azimuthal enhancements in the H_2 surface density, Hα flux, and $\mu(H\alpha)/\sigma(H_2)$, $\mu(H\alpha)/\mu(B)$, and $\sigma(H_2)/\sigma(HI)$ ratios are found on the northeast spiral arms. However, enhancements in $\sigma(H_2)$ on the southwestern arms are often not followed by enhancements in the Hα flux or the $\mu(H\alpha)/\sigma(H_2)$ ratio. The azimuthal variations of the stars and gas are discussed in light of various models of star formation, with emphasis given to models of spiral density waves gathering clouds, with subsequent cloud-cloud collisions (*e.g.* Scoville and Hersh 1979; Kwan and Valdes 1983, 1987).

Azimuthal variations as a function of radius are also determined. The arm-interarm contrasts in I- and B-band and Hα surface brightnesses and H_2 surface

density as well as the $\mu(H\alpha)/\sigma(H_2)$ and $\mu(H\alpha)/\mu(B)$ ratios all increase with radius. We propose the hypothesis that an increasing spiral arm amplitude may be responsible for an increase in the H_2 surface density and the massive star formation efficiency (inferred from the $\mu(H\alpha)/\sigma(H_2)$ ratio) as suggested by several authors (*e.g.* Kwan and Valdes 1987; Elmegreen 1988).

A small survey of the CO contents of dwarf irregular galaxies is presented in Chapter 5. The galaxies were selected to span a wide range in far infrared luminosity and color, and also presumably in star formation rate. The main thrust of the chapter is to discern whether the molecular gas contents lend evidence evidence for or against a bursting mode of star formation in dwarf galaxies. The CO emission is found to be extremely weak in these systems with 5 out of the 15 objects having $> 3\sigma$ detections. CO luminosities are compared with far infrared luminosities (as determined from IRAS 60 and 100 μm coadded survey data). The galaxies are classified according to their star formation properties and we find that the blue, actively star forming galaxies have the highest L_{IR}/L_{CO} ratios, while the red systems have the lowest values of this ratio. We suggest that these results are consistent with the hypothesis that dwarf galaxies experience bursts of star formation, and that the red systems are in a preburst state.

Chapter 6 deals with the differences in the interstellar media between NGC 6946 and the dwarf galaxies. Models of atomic and molecular gas distributions in galaxies of Federman, Glassgold, and Kwan (1979) and Shaya and Federman (1987), which

suggest that the atomic gas in galaxies is found largely in the envelopes around molecular clouds, are discussed. These authors calculate that HI column densities are determined by the gas volume density and the UV radiation field. Given the inferred H_2 and HI masses, the dwarf galaxies have a much smaller percentage of their interstellar medium in the molecular form than does NGC 6946. Differences in the relative amounts of molecular and atomic gas in the inner and outer parts of NGC 6946, and in the dwarf galaxies are discussed in light of these models.

The main conclusions of the thesis are summarized in Chapter 7.

CHAPTER 2

THE NEUTRAL HYDROGEN DISK IN THE Scd GALAXY NGC 6946

2.1 Introduction

Understanding the processes by which star forming material cycles from one phase of the interstellar medium to another is a key to understanding galactic evolution. Knowledge of the relative amounts of atomic, molecular and ionized hydrogen at particular locations in a galaxy are required to determine whether star and molecular cloud formation occur with a constant efficiency on the scale of a few kpc in galaxies, or proceeds in a succession of bursts. For example, a high abundance of molecular hydrogen relative to neutral or ionized hydrogen may be an indication that a region of a galaxy is ripe for star formation, while a large amount of ionized gas relative to the mass of neutral or molecular hydrogen may be indicative of the energy input from a recent burst of star formation. Consequently, if no variations in the relative amounts of molecular, neutral or ionized hydrogen are seen, one might infer that present epoch star formation and molecular cloud formation are proceeding with relatively constant efficiencies. A thorough investigation of the atomic, molecular and ionized components of the interstellar medium in a galaxy makes it possible to estimate total gas masses, molecular cloud formation efficiencies, star formation rates, star formation efficiencies, and gas depletion timescales at every location. These quantities can then be used to constrain models of the cycling of matter from one phase of the interstellar medium to the next.

To better understand the cycling of the interstellar medium and efficiency of star formation in a particular galaxy, we have undertaken a multi-wavelength investigation of the relatively face-on Scd galaxy, NGC 6946. NGC 6946 has been well-studied optically by a number of authors. It is included in *The Atlas of Peculiar Galaxies* (Arp 1966) because of a large, high surface brightness arm in the north-east quadrant of the galaxy. Photometric data from Ables (1971) and Elmegreen and Elmegreen (1984) indicate the exponential nature of the blue and I band luminosity profiles. Hα studies by DeGioia-Eastwood *et al.* (1984) and Hodge and Kennicutt (1983) have been used to infer the massive star formation rate in this galaxy. Infrared observations by Telesco and Harper (1980) show intense emission from the central 30". Complete maps of NGC 6946 at 120 μm and 170 μm (Smith, Harper and Lowenstein 1984) indicate the presence of significant amounts of cold dust; they suggest that at optical wavelengths the nucleus and disk of NGC 6946 suffer from considerable obscuration by this dust. They also find that 90% of the emission at wavelengths longward of 100 μm originates in the disk of the galaxy, and that only 10% is from the nucleus.

There are also numerous studies of NGC 6946 at radio wavelengths. The HI distribution has previously been determined by Rogstad, Shostak and Rots (1973) at 2' resolution, and shown to extend well beyond the optical image. Radio continuum emission has been observed at 2.8 cm (Klein *et al.* 1982) and at 6, 21 and 49 cm (van der Kruit, Allen and Rots 1977); all the nonthermal exponential distributions have

scale lengths which resemble the blue luminosity profile of Ables (1971). Klein *et al* find that the thermal emission at 2.8 cm is correlated with the optical HII distribution of Hodge (1969). Observations of the CO distribution have previously been made by several authors (Morris and Lo 1978; Rickard and Palmer 1981; Young and Scoville 1982a). Young and Scoville found that the radial behavior of the CO distribution resembles the blue luminosity profile of Ables (1971). From a comparison with the CO data of Young and Scoville (1982a), DeGioia-Eastwood *et al.* (1984) find a constant Hα/CO ratio as a function of radius in NGC 6946, implying a constant star formation efficiency with radius. Finally, an interferometric study of CO in the central 1' of NGC 6946 (Ball *et al.* 1985) has uncovered a molecular bar ~45" long.

Because NGC 6946 lies close to the galactic plane, and thus suffers from considerable extinction, its distance is very uncertain. Various authors give distances to this galaxy ranging from 5 Mpc (deVaucouleurs 1979) to 10.1 Mpc (Rogstad, Shostak and Rots 1973, and references therein). Since most of the previous optical and radio studies of NGC 6946 have used the latter distance, we adopt a distance of 10.1 Mpc to be consistent with these studies. The global properties of NGC 6946 are given in Table 2.1.

In this paper we present HI observations of NGC 6946 obtained at the VLA in the D configuration. At the assumed distance of 10.1 Mpc, the 40" resolution of the synthesized beam corresponds to a diameter of 2 kpc on the galaxy. In Chapter 3 we

Table 2.1

NGC 6946 Properties

R.A. (1959)[a]	$20^h33^m48^s.8$
Dec. (1950)[a]	59°58'50"
V_{sun}[b]	46 km s^{-1}
Classification[b]	Scd
Distance[c]	10.1 Mpc
Inclination[c]	30°
Position Angle[c]	62°
D_{25}[b]	10.97'

[a] Dressel and Condon 1976

[b] deVaucouleurs, deVaucouleurs, and Corwin 1976

[c] Rogstad and Shostak 1972

will present the results from a complete ^{12}CO study of this galaxy and a point by point comparison of the HI, H_2, blue and I band surface densities and fluxes over the entire optical disk of the galaxy. For the purposes of this discussion, we identify 3 distinct regions within NGC 6946, each of which has unique characteristics: 1) the central 1', where the CO bar is located, 2) the inner disk ($r \leq 4'$), where the galaxy is optically luminous and H_2 is abundant, and 3) the outer disk ($r > 4'$), where the extended HI component is found.

2.2 Observations

The 21-cm line data were obtained in 1984 October using the Very Large Array (VLA)[1] in the D configuration for 10 hours of observing time; the maximum and minimum antenna separations in this array are 1.03 and 0.04 km respectively. The resolution of the synthesized beam is 40"×37". A total bandwidth of 3.1 MHz, divided into 64 channels, was available, of which 31 narrow band channels and a broad-band channel of the central 2.4 MHz were useful. The resulting velocity resolution was 10.3 km s^{-1} and the rms noise per channel was ~2.5 mJy $beam^{-1}$ after subtraction of the continuum. Standard VLA Dec-10 programs were used in flagging bad data and for calibration.

1. The National Radio Astronomy Observatory is operated by Associated Universities Inc., under contract with the National Science Foundation.

All maps were made on the AIPS system at the VLA. The continuum emission was subtracted from the channel maps by first summing all the dirty channel maps and subtracting them from the broad-band continuum channel to produce a map of pure continuum emission. Finally, the average continuum emission was subtracted from each channel map to obtain continuum free maps. The difference maps were CLEANed and restored with a gaussian beam of 40"×37" (Clark 1980). For the final analysis of the data, a three-dimensional data cube was constructed from the channel maps. The zeroth and first moments of the cube were then taken to produce the two dimensional HI mean intensity and mean velocity maps.

2.3 Atomic Hydrogen Emission

2.3.1 HI Kinematics

Figures 2.1a and b show the HI emission in the individual velocity channels ranging from -79 to +168 km s^{-1}. Contours are in intervals of 10 mJy $beam^{-1}$, with the lowest level of 10 mJy $beam^{-1}$, representing a 4σ detection. The continuum emission has been subtracted from each channel map as described in § 2.2. In a global sense, the line channel maps indicate the systematic kinematics in the disk of NGC 6946 resulting from galactic rotation. However, on the smaller scale, there are kinks present in the individual maps which indicate the presence of non-circular velocities or warps in the disk of the galaxy. Since NGC 6946 lies close to the galactic plane

Figure 2.1a,b: HI intensity maps (not corrected for the response of the primary beam) for 25 of the 32 velocity channels with which observations were made. The contours for each map are in intervals of 10 mJy beam^{-1} with the lowest level at 10 mJy beam^{-1} (4σ). The 40" synthesized beam is shown at the bottom of Figure 2.1a.

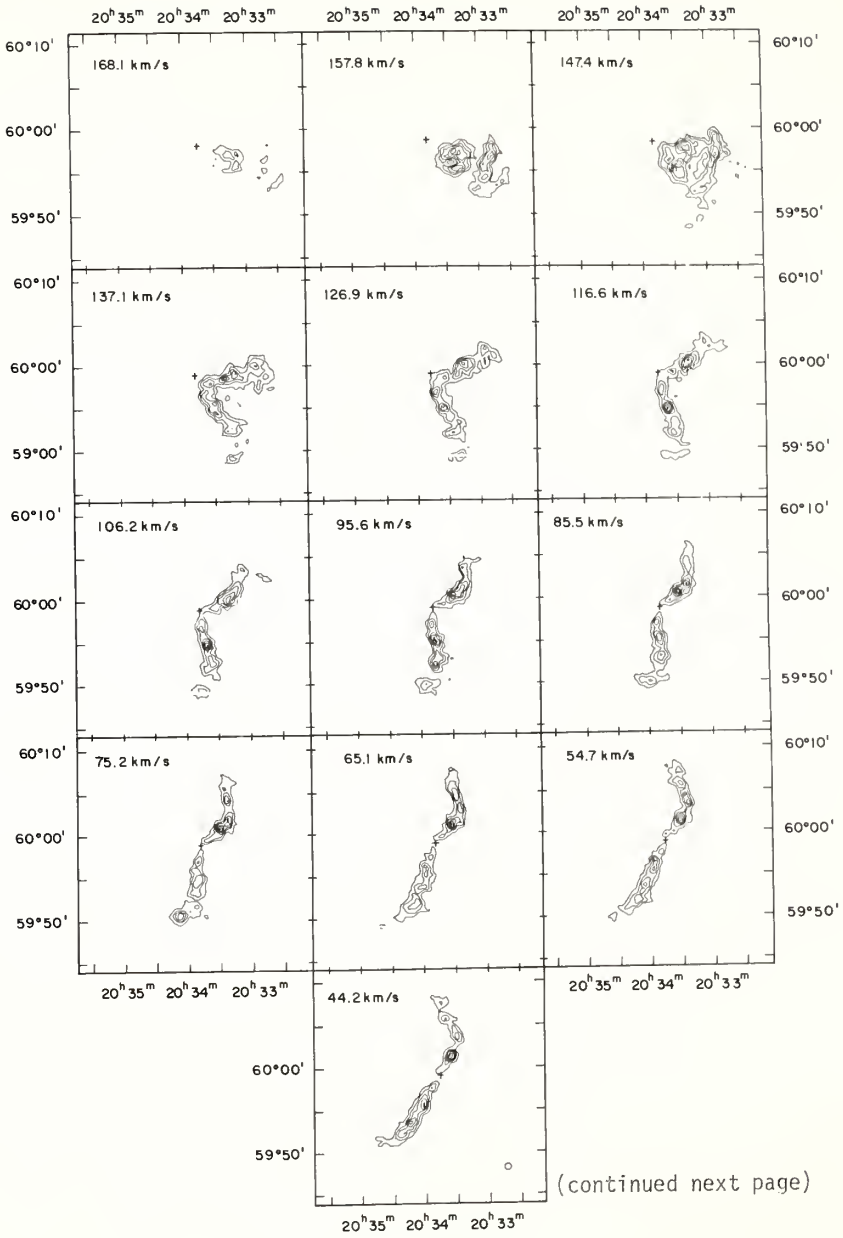

(continued next page)

(Figure 2.1 continued)

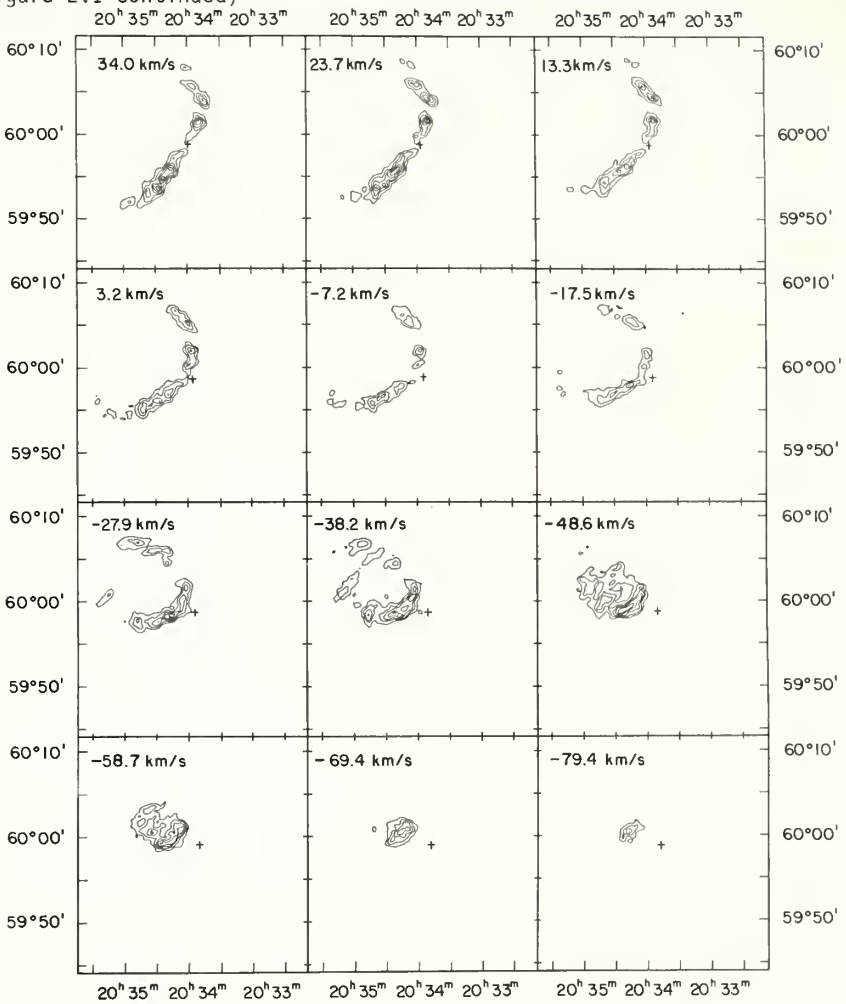

and has a low redshift, velocities corresponding to the range -12 to +8 km s^{-1} may be affected by galactic HI.

The mean HI velocity field is shown in Figure 2.2 superposed on a photograph of the galaxy. The contours of constant velocity, separated by 20 km s^{-1}, indicate both circular rotation and peculiar kinematics. In particular, the velocity contours in the center of NGC 6946 exhibit a rotation with respect to the velocity contours of the inner disk, a characteristic often found in the centers of barred spiral galaxies (*eg.* Van der Kruit and Allen 1978). The HI study of NGC 6946 at 2' resolution by Rogstad, Shostak and Rots (1973) also shows evidence for this effect to a small extent.

We note several other kinematic features. First, in the inner disk, the lowest velocity observed (-50 km s^{-1}) is found in only one location, coincident with the bright optical arm in the NE. Thus, the rotation curve rises and then falls on this side of the galaxy. Second, the gap in the velocity field found in the northern part of the galaxy between -30 and +30 km s^{-1} is due to an absence of HI emission from this region, since the velocity range is wider than would be expected for galactic absorption, although we cannot rule out foreground absorption as being partially responsible. Thirdly, as seen in Figure 2.2, many of the observed departures from pure circular rotation in the HI velocity field are coincident with spiral arms. In particular, there are 25 km s^{-1} deviations from circular motion which coincide with the HI spiral arms in the outer disk (see § 2.3.2).

Figure 2.2: The mean velocity field for NGC 6946 superposed on an enlargement of the Palomar Sky Survey blue print. The contour values range from -50 to 150 km s^{-1} in steps of 20 km s^{-1} as indicated. The HI synthesized beam is shown at this scale.

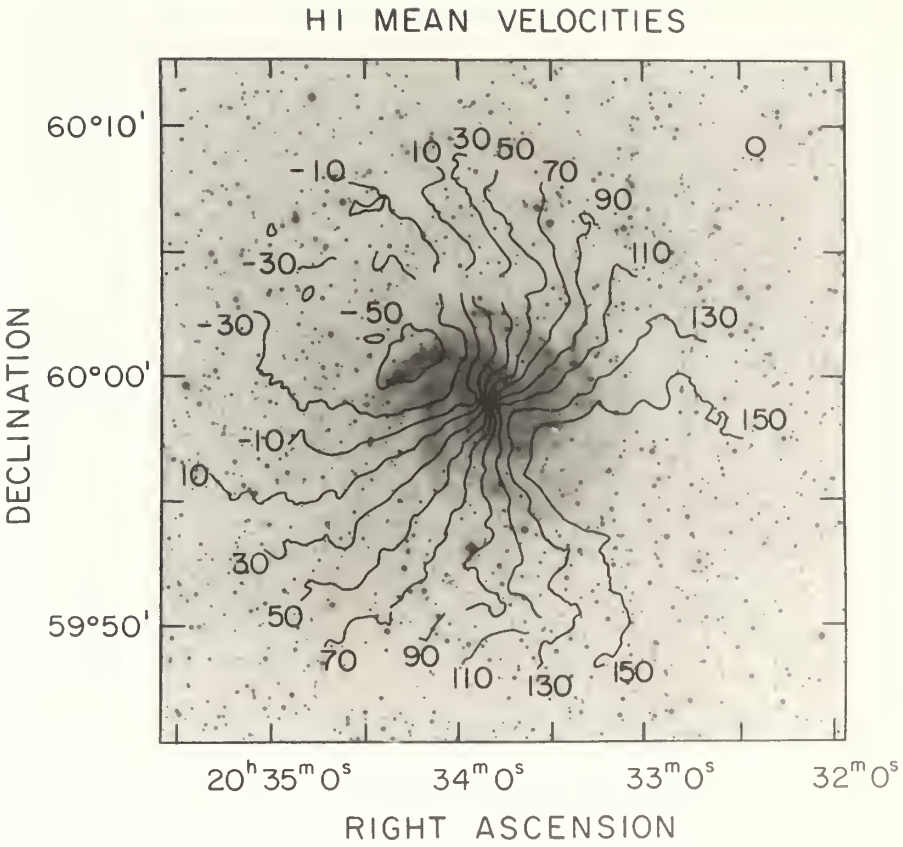
HI MEAN VELOCITIES
60°10'
60°00'
59°50'
DECLINATION
-10
10
30
50
70
90
110
130
150
0
-30
-50
20h35m0s
34m0s
33m0s
32m0s
RIGHT ASCENSION

We have determined the rotation curve in the plane of NGC 6946 along the major axis at 45" resolution (see Figure 2.3) from the mean velocity field, assuming a systemic velocity of 55 km s^{-1} and a constant inclination and position angle (see Table 2.1). Towards the NE part of the galaxy, there is a very steep rise in the rotation velocity up to a peak of V_{max} = 230 km s^{-1} at 11 kpc, followed by a decrease to V = 200 km s^{-1} at 18 kpc, and velocities which remain essentially flat at larger radii. To the SW, there is a much more gradual rise to a peak of V_{max} = 220 km s^{-1} at roughly 12 kpc, and a definite flattening with no decrease beyond that radius.

2.3.2 HI Distribution

A gray scale image of the total HI intensity distribution is shown in Figure 2.4a, and a contour representation of this image is shown superposed on an enlargement of the Palomar Sky Survey in Figure 2.4b. We observe HI emission at greater than the 3σ level out to a radius of ~30 kpc, roughly the Holmberg radius, with HI spiral structure apparent in the outer disk, well beyond R_{25}. The central surface density of HI (corrected to the plane of the galaxy) is 7×10^{20} H cm^{-2}, with extreme values over the entire HI disk of 2.1×10^{20} (3σ) to 2×10^{21} H cm^{-2}. The depression in the center of the galaxy is asymmetric in the sense that it is elongated with an axial ratio of 3:1, and has a position angle of 60°, which is close to the major axis determined for the outer disk. In contrast, the kinematic major axis in the central 1' has a position angle closer to 90° (see Figure 2.2).

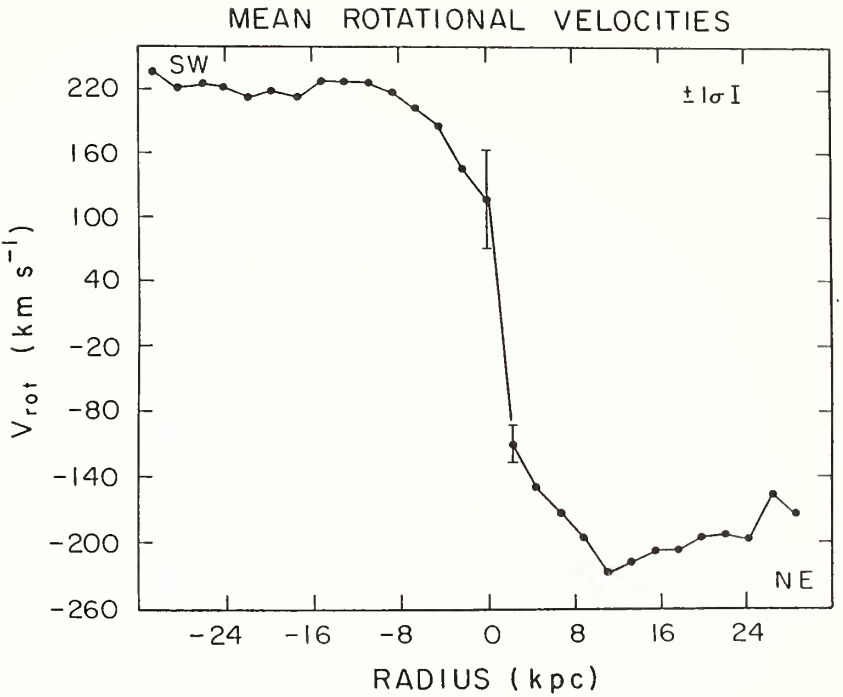

Figure 2.3: The mean rotation velocities as a function of radius along the major axis for NGC 6946 are illustrated, corrected to the plane of the galaxy. A typical 1σ uncertainty is illustrated. The two points closest to the kinematic center of the galaxy have large uncertainties as indicated. In this figure, 0 kpc is defined to be the central pixel (assigned to be the RC-2 coordinates of the galaxy) of the HI intensity map.

Figure 2.4a: A gray scale representation of the total HI integrated flux distribution.

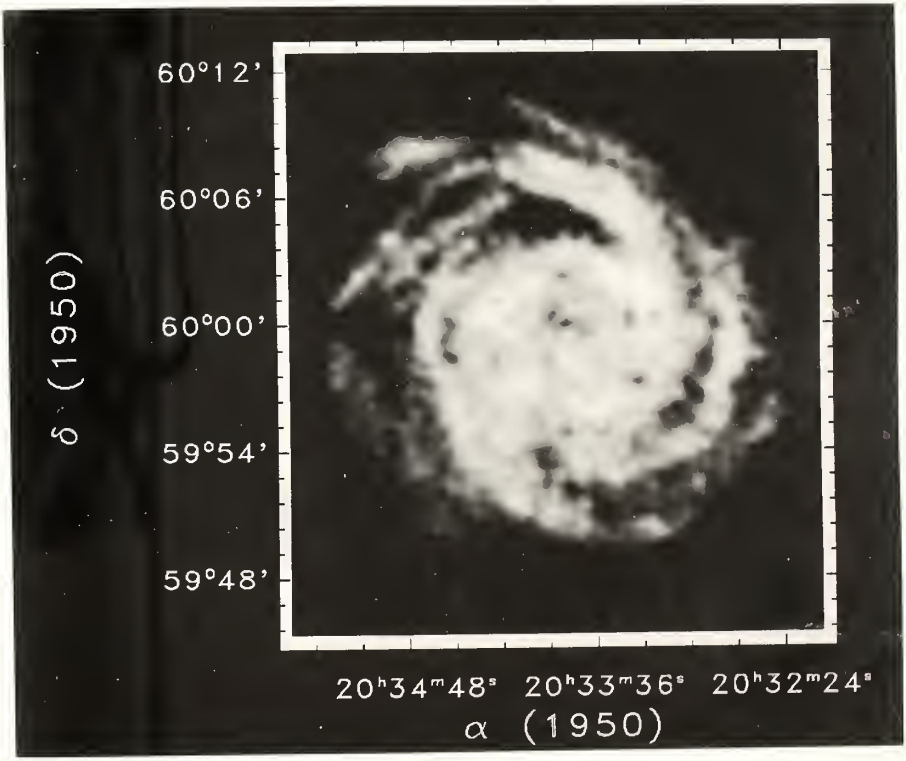
60°12'
60°06'
60°00'
59°54'
59°48'
δ (1950)
20h34m48s
20h33m36s
20h32m24s
α (1950)

Figure 2.4b: A contour representation of the HI flux distribution superposed on an enlargement of the blue Palomar Sky Survey print. The contour levels range from 0.2 to 3.0 Jy km s^{-1} and are separated by 0.4 Jy km s^{-1} intervals. Regions of HI scarcity are represented by tic marks on the contours. The HI synthesized beam is shown in the bottom left hand corner of the figure.

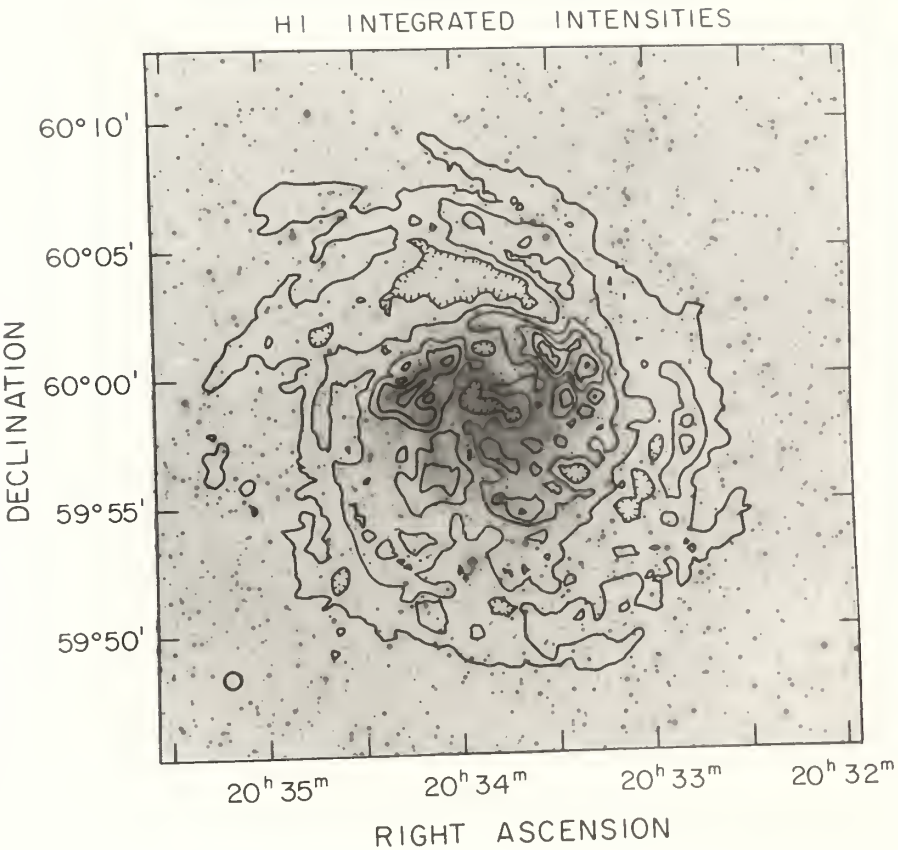
HI INTEGRATED INTENSITIES
60°10'
60°05'
60°00'
59°55'
59°50'
DECLINATION
20h35m
20h34m
20h33m
20h32m
RIGHT ASCENSION

HI structures are observed over a range of size scales. In the outer disk, where HI spiral structure is evident, there are HI spiral arms which are 9' long (26 kpc) and 2' across (6 kpc), as measured from the half peak intensity. There are two HI peaks located ~4' to the northwest and northeast of the center which are ~2'.5×2'.5. The peak to the northeast contains ~2.4×10^8 M_o of HI in an area of 1.9×10^7 pc^2, and is roughly coincident with the largest, high surface brightness spiral arm in the optical disk. The stronger peak to the northwest of the center contains ~3.8×10^8 M_o of neutral gas in a region of 2.8×10^7 pc^2, and is also coincident with an optical spiral arm. The HI surface densities in these regions are ~14 M_o pc^{-2}. We also observe several resolvable HI depressions larger than 45" (2.2 kpc) across to the north and southwest of the center of NGC 6946, as well as in the central region itself.

Figure 2.5 shows the individual HI surface densities in NGC 6946 for the entire disk sampled every 45". At a particular radius, there is a scatter of a factor of 2 relative to the mean value, which arises from the absence of azimuthal symmetry in the disk. We have computed the azimuthally averaged radial distribution of HI in NGC 6946 as indicated by the solid line (see also Table 2.2). The HI distribution has a central depression, a rise to the maximum at a radius of ~8 kpc, followed by a decrease with radius out to a plateau at 20 kpc, and finally a decrease out to a distance of 30 kpc where the emission falls below our sensitivity level. The features at 8 kpc

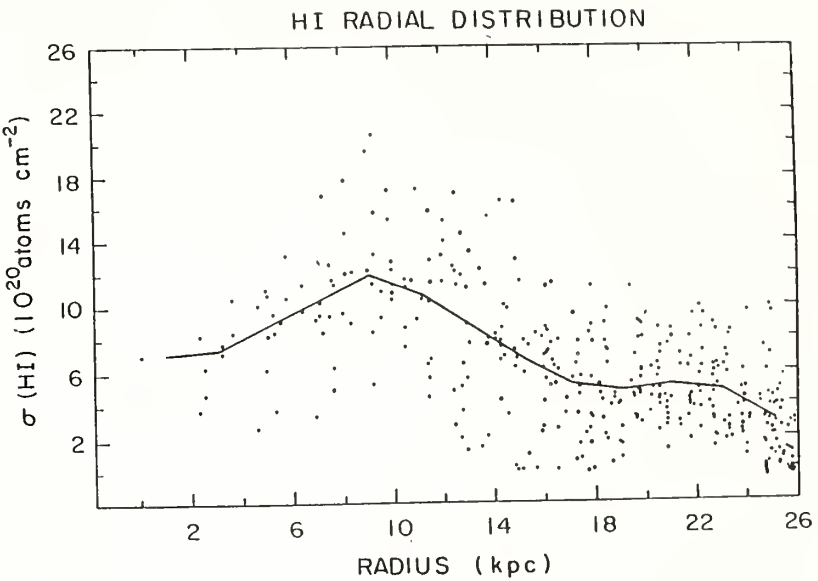

Figure 2.5: The total HI distribution for NGC 6946. The solid line represents the azimuthally averaged distribution over 2 kpc annuli in the plane of the galaxy.

Table 2.2

Face-On Radial Distributions

Notes to Table 2.2:

All distributions have been corrected to the plane of the galaxy.

[a] HI surface density at 40" resolution from this work and assuming $\sigma_{HI} = 1.85\times10^{18} (\cos i) \int T_B \, dv$.

[b] H_2 distribution from a fully sampled CO map at 45" resolution (Chapter 3) and assuming $N(H_2)/I_{CO} = 2.8\times10^{20} (\cos i)$ H_2 $cm^{-2}/(K \text{ km } s^{-1})$.

[c] Azimuthally averaged blue luminosity profile from Ables (1971).

[d] 49 cm radio continuum distribution from van der Kruit, Allen and Rots (1977).

[e] I band relative surface brightness from Elmegreen and Elmegreen (1984). I_5 is defined as the surface brightness at a radius of 5 kpc.

[f] SFR from Hα observations of DeGioia-Eastwood *et al.* (1984).

Table 2.2

Face-On Radial Distributions

Radius kpc	N(HI)[a] 10^{20} at/cm^2	N(H_2)[b] 10^{20} at/cm^2	L_B[c] mag/arcsec^2	S_ν(49 cm)[d] mJy/beam	I/I_5[e]	SFR[f] M_o/Gyr pc^2
1	7.2	240	21.80	159	1.72	156
2	7.3	140	22.10	132	1.45	132
3	7.4	97	22.30	100	1.32	108
4	8.2	63	22.47	87.1	1.12	84
5	9.0	45	22.65	69.2	1.00	63
6	9.6	37	22.85	57.5	0.90	43
7	10.5	28	23.07	46.8	0.83	37
8	11.2	23	23.30	38.0	.76	31
9	12.0	18	23.55	30.9	0.72	24
10	11.4	14	23.75	25.1	0.68	22
11	10.8	10	24.00	20.4	0.66	20
12	9.8	9.9	24.20	16.6	0.63	-
13	8.9	9.6	24.45	13.5	0.59	-
14	7.8	<9.0	24.67	11.0	0.53	-
15	6.8	-	24.90	8.91	0.48	-
16	6.0	-	25.10	7.59	-	-
17	5.2	-	25.35	6.03	-	-
18	4.9	-	25.60	4.79	-	-
19	4.7	-	25.83	3.98	-	-
20	4.9	-	26.07	3.16	-	-
21	5.1	-	26.30	-	-	-
22	4.9	-	26.60	-	-	-
23	4.8	-	26.80	-	-	-
24	4.0	-	27.00	-	-	-
25	3.0	-	-	-	-	-
26	3.1	-	-	-	-	-
27	2.8	-	-	-	-	-
28	2.5	-	-	-	-	-
29	2.1	-	-	-	-	-

and 20 kpc radius are coincident with the bright optical spiral arms in the inner disk, and the HI spiral arms in the outer disk.

Table 2.2 gives the face-on radial distributions in NGC 6946. Relative to the blue surface brightness which drops off by a factor of 13 between 8 and 20 kpc from the center of the galaxy (Ables 1971), the HI surface density decreases by only a factor of 2.4 over the same region. However, since there is evidence for faint optical spiral arms beyond R=20 kpc which follow the HI arms (*eg*. Rogstad, Shostak and Rots 1973), we infer that star formation must have occurred at some level in the outer disk of NGC 6946.

Shown in Figure 2.6a is the azimuthally averaged HI distribution along with the radial distribution of H_2, inferred from our fully sampled ^{12}CO map of the inner disk (Chapter 3). The H_2 distribution has a central peak with a continuous falloff in radius as found previously (Young and Scoville 1982a; Morris and Rickard 1982) in sharp contrast with the HI central depression and peak at 8 kpc. The mass of gas in molecular clouds compared to atomic clouds is thus much greater in the inner few kpc than at 10 kpc radius. These trends in the molecular and atomic gas distributions are common in luminous, late-type spiral galaxies (*eg*. Rogstad and Shostak 1972; Bosma 1978; Young and Scoville 1982a; Morris and Rickard 1982; Scoville and Young 1983; Kenney and Young 1987). Sensitivity limits on CO observations at the present

Figure 2.6a: The azimuthally averaged face-on radial distributions of HI and H_2 surface densities (this work).

b: The radial blue luminosity profile from Ables (1971) and total SFR's determined from Hα (DeGioia-Eastwood *et al.* 1984) corrected to the plane of the galaxy.

c: The 21 cm and 49 cm radio continuum radial distributions from van der Kruit, Allen and Rots (1977).

d: The total ISM (HI+H_2) and I band (Elmegreen and Elmegreen 1984) radial distributions. At radii greater than 12 kpc, the closed circles represent HI+H_2 upper limits and the open circles represent the HI lower limits to the total ISM surface density.

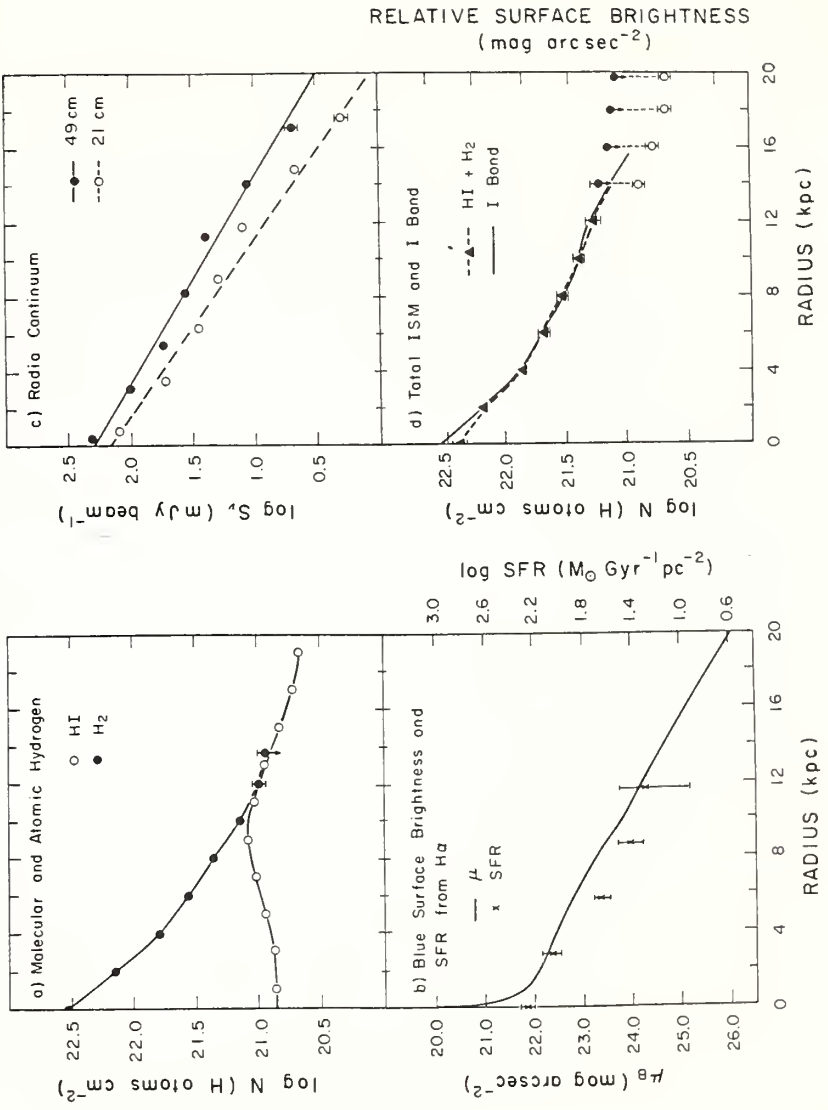
a) Molecular and Atomic Hydrogen
HI
H2
log N (H atoms cm-2)
b) Blue Surface Brightness and SFR from Hα
μ
SFR
μB (mag arcsec-2)
log SFR (M⊙ Gyr-1 pc-2)
RADIUS (kpc)
c) Radio Continuum
49 cm
21 cm
log Sν (mJy beam-1)
d) Total ISM and I Band
HI + H2
I Band
log N (H atoms cm-2)
RELATIVE SURFACE BRIGHTNESS
(mag arcsec-2)
RADIUS (kpc)

time make it difficult to determine the H_2 surface density in NGC 6946 beyond a radius of 12 kpc.

From the HI distribution we have determined a total HI mass for NGC 6946 of 1.1×10^{10} M_o out to a radius of 30 kpc compared to a mass of 2.1×10^{10} M_o from Rogstad, Shostak and Rots (1973).[2] We also find a total H_2 mass of 1.2×10^{10} M_o, which agrees quite well with the previously determined value (Young and Scoville 1982a). Thus, even though the molecular and atomic components of NGC 6946 are distributed quite differently throughout the galaxy, they each comprise roughly 50% of the mass in the ISM, with the molecular gas being dominant in the inner disk ($R\leq$8-10 kpc) and the atomic gas more prevalent in the outer disk.

2.4 Comparison of Mass and Light Distributions

2.4.1 Star Formation Efficiency

In this section we compare the measured HI and H_2 radial distributions with those determined previously in Hα (DeGioia-Eastwood *et al.* 1984), B and I band (Ables 1971; Elmegreen and Elmegreen 1984) and radio continuum (Van der Kruit, Allen and Rots 1977). The azimuthally averaged distributions of HI, H_2, total ISM, B and I band, 49 and 21 cm radio continuum emission, and the star formation rates determined

2. The difference between our total HI mass and that of Rogstad, Shostak and Rots may be due in part to the fact that their map shows detectable HI emission beyond a radius of 30 kpc. That is, because our maps were not corrected for the response of the primary beam, we may not be sensitive to this emission, or the D configuration may not be sensitive to very extended structures.

from Hα (DeGioia-Eastwood *et al.* 1984) are all shown in Figures 2.6a through 2.6d, where the straight line appearance of the profiles on these semi-log plots indicates the exponential nature of the distributions.

We have fitted the distributions in NGC 6946 (excluding R<2 kpc) with functions of the form

$$I = I_o e^{-R/R_o} \tag{2.1}$$

where I_0 is the central intensity and R_0 is the exponential scale length (see Table 2.3). The blue luminosity profile, radio continuum emission, H_2 and Hα distributions all have similar scale lengths with values between 4.1±0.3 and 5.0±0.3 kpc.[3] This result supports the finding of Young and Scoville (1982a) that the CO distribution follows the blue light in NGC 6946, and that of DeGioia-Eastwood *et al.* (1984) that the Hα and CO distributions are similar. In contrast, the HI distribution shows a much shallower falloff in radius from the peak in the HI profile outward, with a scale length of 14.4 kpc for radii beyond 10 kpc radius.

Also shown in Figure 2.6 is the total ISM (HI+H_2) radial distribution on the scale of 2 kpc along wth the I band disk light profile. The total ISM surface density scale length is similar to that of the I band over the region where H_2 is detected.

---

3. We note that the B luminosity profile of Ables and that of Elmegreen and Elmegreen suggest different scale lengths (R_0=4.3 kpc for Ables and 6.3 kpc for Elmegreen and Elmegreen) over the region of the disk which Elmegreen and Elmegreen measured. We have chosen to compare the B profile of Ables with the other components of NGC 6946 since it extends much farther out in the disk.

Table 2.3

Disk Scale Lengths

Component	R (kpc)
HI[a]	14.4±0.1
H_2[b]	4.3±0.1
Hα[c]	5.0±0.1
B[d]	4.3±0.1
I[e]	6.3±0.1
Radio Continuum[f] 49 cm	4.7±0.3
21 cm	4.1±0.3
HI+H_2[g]	5.6±0.1

[a] This work; fit from R = 10 kpc to 29 kpc

[b] Tacconi and Young (1986); fit from R = 2 kpc to 14 kpc

[c] Hα from DeGioia-Eastwood *et al.* (1984); fit from 2-12 kpc

[d] Ables (1971); fit from R = 2 kpc to 24 kpc

[e] Elmegreen and Elmegreen (1984); their fit

[f] van der Kruit, Allen and Rots (1977); their fit

[g] Total ISM; fit from R = 2 kpc to R = 14 kpc

Unfortunately, the I band distribution does not extend to sufficiently large radii to determine whether it flattens out to follow the HI+H_2 surface density, or falls more steeply. However, it is clear that the blue surface brightness profile does not resemble the sum of the HI+H_2 surface densities in the outer disk; this is primarily because the HI distribution in the outer disk is much flatter than the B luminosity profile.

The fact that the Hα, blue band, radio continuum and molecular distributions are similar can be understood in terms of the star formation history and star formation efficiency in NGC 6946. Based on the study by Searle, Sargent and Bagnuolo (1973), it is straightforward to show that ~50% of the blue light in a late type spiral galaxy originates from stars younger than 2×10^9 years old (*eg*. Young, Scoville and Brady 1985). Thus, the blue light distribution is indicative of the past star formation history in the galaxy integrated over ~2×10^9 years. The similarity of the CO and blue light distributions in NGC 6946 led Young and Scoville (1982a) to suggest that the star formation integrated over the past 2×10^9 years is proportional to the H_2 surface density, or that the star formation efficiency is constant with radius.

The radio continuum emission is contributed by both thermal and nonthermal components. Klein *et al.* (1982) find that ~19% of the radio continuum emission at 2.8 cm is of thermal origin, while 81% is nonthermal. The thermal component arises mainly from the ionizing flux of young O and B stars, while the nonthermal component is due to relativistic electrons spiraling in the galactic magnetic field (*cf.*

Lequeux 1971; Ekers 1981; Israel and Rowan-Robinson 1984). Supernova remnants are certainly one source of cosmic ray electrons (*eg*. Condon *et al*. 1982), although not the only source. For the cosmic ray nuclei, the isotopes of elements neon through nickel resemble those of the ambient ISM rather than supernova ejecta (Young *et al*. 1981). Since no cosmic ray acceleration mechanism is likely to accelerate nuclei and not electrons, an important source of cosmic ray electrons may be the ambient ISM. If the dominant source of cosmic ray electrons is the ambient ISM, then the correlation between H_2 and the radio continuum is not surprising, and indicates a constant cosmic ray production efficiency with radius relative to the ambient ISM. Therefore, the similarities among the blue, Hα, CO and radio continuum distributions may indicate a uniform efficiency with radius of the production of massive stars, cosmic rays, and all stars integrated over 2×10^9 years and averaged on a 2 kpc scale. The fact that the atomic gas distribution is different from all other components of the galaxy strongly indicates that although HI may be the reservoir from which molecular clouds form, it plays only a passive role in the actual star formation process of high luminosity, late type spiral galaxies such as NGC 6946. Recent work by Shaya and Federman (1987) indicates that a large fraction of the neutral hydrogen in a galaxy may be due to the dissociation of molecular hydrogen in the envelopes of molecular clouds by the UV radiation field.

Following the arguments of Schmidt (1959), we assume that the star formation rate depends on some power n of the gas volume density or

$$SFR = c\rho(gas)^n \qquad (2.2)$$

where c is a constant. From a comparison of HI observations of the Milky Way with the scale height of Cepheids and the overall stellar mass distribution, Schmidt concluded that n~2.

Writing the gas surface density as the product of the volume density and scale height, or $\sigma(gas) = \rho(gas)\, z\,(gas)$, equation 2.2 then becomes

$$SFR = c_1[\sigma(gas)/z\,(gas)]^n \qquad (2.3)$$

The results of Young and Scoville (1982a) and DeGioia-Eastwood *et al.* (1984) that the blue and Hα surface brightnesses are proportional to the CO surface density in a region where $\sigma(H_2) >> \sigma(HI)$ is equivalent to showing that the exponent n has a value of 1. If we define the star formation efficiency (SFE) as the star formation rate per unit molecular mass, and if the scale height of H_2 is constant over the inner 12 kpc radius so that the SFE ~ SFR/$\sigma(H_2$, then in NGC 6946 the SFE for O, B, and A stars is constant as a function of radius.

One consequence of a constant SFE with radius is that one expects a constant fraction of mass to be cycled into heavy elements and returned to the ISM. In the absence of radial mixing or infall of metal poor gas, there should be no radial metallicity gradient. While many galaxies have significant radial metallicity gradients (*e.g.* Pagel and Edmunds 1981), in NGC 6946 McCall (1982) finds a decrease of only

a factor of 1.4 in the [O/H] ratio over the inner 10 kpc. Thus the inferred constant SFE with radius is consistent with the small radial metallicity variation in this galaxy.

2.4.2 Molecular Cloud Formation Efficiency

If molecular clouds form from atomic gas clouds, then the ratio of $\sigma(H_2)/\sigma(HI)$ is a measure of the molecular cloud formation efficiency. Table 2.4 lists the ratio of H_2 to HI surface density, along with the ratio of the star formation rates to $\sigma(H_2)$. The distinct difference in the distributions of HI and H_2, as shown in Table 2.4, indicates that the molecular cloud formation efficiency is *not* constant as a function of radius, but decreases quite dramatically.

A better measure of the molecular cloud formation efficiency would be to compare the volume densities of HI and H_2. If the HI scale height increases in the outer disk of NGC 6946 as it does in the Milky Way (Kulkarni, Blitz and Heiles 1982, then the HI volume density must decrease more rapidly with radius than the HI surface density. A rapid drop in the HI volume density in the outer disk could cause the lower molecular cloud formation efficiency, whereby subsequent star formation would occur at a reduced rate relative to that in the inner disk. However, even though the cloud formation efficiency decreases with radius, once molecular clouds are formed, new stars appear to form from these clouds with a relatively constant efficiency as a function of radius.

Table 2.4

Molecular, Atomic and Ionized Gas Ratios

Radius kpc	$\sigma(H_2)/\sigma(HI)$	Star Formation[a] Efficiency
1	33±4	0.4±0.3
2	19±2	0.6±0.3
3	13±2	0.7±0.4
4	7.7±0.9	0.9±0.6
5	5.0±0.6	0.9±0.7
6	3.9±0.5	0.8±0.9
7	2.7±0.4	1.0±1.0
8	2.1±0.3	1.0±1.0
9	1.5±0.2	1.0±1.0
10	1.2±0.2	1.0±1.0
11	0.9±0.2	1.3±1.0

[a] Star formation efficiency is defined as SFR $/\sigma(H_2)$ Units are in Gyr^{-1}, and 1/SFE gives the depletion timescale.

2.5 Conclusions

From this study of the neutral hydrogen content of NGC 6946 we have found:

1) There is detectable HI emission observed out to a radius of 30 kpc. This emission exhibits a clumped structure on a scale of 2 kpc, with evidence for HI spiral structure in the outer disk.

2) The velocity field in the central 2' exhibits a rotation relative to the position angle of the major axis further out in the disk, a characteristic often found in barred spiral galaxies. The distortions of 25 km s^{-1} in the velocity field of the disk are coincident with the HI and optical spiral arms.

3) When compared to the optical, radio continuum, Hα, and molecular radial distributions of NGC 6946, we find that the HI distribution is the only one which is decidedly different from the rest. We infer from this that the atomic gas component plays only a passive role in the evolution of high luminosity, late type spiral galaxies.

4) While the star formation efficiency has been inferred to be constant with radius (DeGioia-Eastwood *et al.* 1984; Young and Scoville 1982a), we find that the molecular cloud formation efficiency decreases with radius. The optical edges of galaxies, therefore, may reflect the edges of the molecular disks in galaxies, where the formation of molecular clouds from atomic clouds is greatly reduced due to the increasing HI scale height and therefore decreasing HI volume density.

CHAPTER 3

THE CO DISTRIBUTION IN THE Scd GALAXY NGC 6946

3.1 Introduction

Since stars form in molecular clouds, the distribution and abundance of molecular clouds in a galaxy play an important role in the evolution of the disk. Measuring the total distribution of molecular material in a galaxy is necessary for determining any azimuthal structures (*e.g.* spiral arm-interarm contrasts) and radial fluctuations in the molecular gas, as well as kinematic structures. The fluctuations in the relative amounts of molecular gas with respect to the optical luminosity and atomic gas from position to position lend insight into the constancy of star formation efficiency and molecular cloud formation efficiency in a galaxy. We have previously discussed the efficiencies of star and molecular cloud formation as a function of radius in NGC 6946 (Tacconi and Young 1986; Chapter 2). In this chapter, we present observations of the total molecular gas distribution of this galaxy; the detailed discussion of the H_2 and HI distributions and their implications for the evolutionary history of NGC 6946 will be given in Chapter 4.

The most straightforward way to measure the molecular gas distribution in a galaxy at this time is through observations of the J=1→0 rotational transition of ^{12}CO. It is quite a time consuming process, however, to measure the total CO distributions for the large nearby galaxies. Integration times of 2 hours or longer per position are often necessary to achieve an acceptable signal-to-noise ratio in the disks of spiral

galaxies. Thus, to observe in CO a significant fraction of the disk of a luminous, spiral galaxy often requires more than 100 hours of integration time. Because of limitations in sensitivity and observing time, most studies of the CO contents of galaxies have consisted of observations along one or two position angles, from which the total molecular gas mass has been inferred. Few fully sampled ^{12}CO maps covering a large fraction of the optical disks of galaxies have been published to date (*cf* Young and Scoville 1984; Rydbeck, Hjalmarson and Rydbeck 1985; Lord 1987; Lord and Young 1987). Here, we present CO observations at 110 locations, comprising a fully sampled ^{12}CO map of the inner 6'.75 of NGC 6946. In addition, we present the HI, B, and I band fluxes (Chapter 2; Elmegreen and Elmegreen 1984), smoothed to the same resolution as the CO data, are presented.

3.2 The Data

3.2.1 CO Observations

Observations of the J=1→0 transition of ^{12}CO were obtained between 1984 November and 1985 June using the 14-meter millimeter wave telescope of the Five College Radio Astronomy Observatory (FCRAO).[1] The telescope was equipped with a 3-mm cooled Schottky diode mixer receiver with a single sideband temperature of ≅170 K. At the frequency of the CO J=1→0 transition (115.271203 GHz), the half-

1. The FCRAO is operated with support from the National Science Foundation under grant AST-82-12252 and with permission of the Metropolitan District Commission, Commonwealth of Massachusetts.

power beam width of the telescope is 45", which corresponds to a diameter of 2.2 kpc at the adopted distance of 10.1 Mpc for NGC 6946 (Rogstad and Shostak 1972; Chapter 2, see Table 2.1). Telescope pointing and focus were checked at the beginning of each run by observing planets and the center of NGC 6946; pointing was found to have an accuracy of ±5" rms.

The CO data were obtained by position switching every 30 seconds to locations 12' east and west of the center, beyond the detectable CO disk, for a total of 1-2 hours of integration per point. That is, for observations where T_R^*(peak)≥0.1 K, an rms of 0.02 K was achieved, whereas for those spectra where T_R^*<0.1 K, and rms of 0.01 K was obtained. Antenna temperatures were calibrated using the chopper wheel method, switching between sky and an ambient load. Velocity resolution was provided by a 256 × 1 MHz filterbank yielding a total bandwidth of 665 km s^{-1} in 2.6 km s^{-1} channels, which were then smoothed to a final resolution of 10 km s^{-1}. The data were corrected to a T_R^* scale (Kutner and Ulich 1981) by scaling the data by the forward scattering and spillover efficiency (η_{fss} = 0.70), such that the center of the Orion Nebula (KL) has T_R^*=72 K. Each spectrum has been further corrected for the elevation dependence of the opacity, although this correction is small (~5-7%) because NGC 6946 was rarely observed below an elevation of 45°. Finally, to account for any systematic effects due to the fact that the galaxy was observed over many months, we observed the center of NGC 6946 at the beginning of each run, and scaled the data such that the center of the galaxy had I_{CO}=47±5 K km s^{-1}, a value for the

galaxy that was determined by averaging all the observations of the central position taken over a three month period.

To determine the azimuthal as well as radial distribution of CO in NGC 6946, we have mapped the galaxy in a series of concentric annuli centered at R=22".5, 45", 1'.5, 2'.25, and 3'. Observations were spaced by 90° in azimuth for the the 22".5 ring (4 positions), 45° for the 45" ring (8 positions), 22.5° for the 1'.5 ring (16 positions), and 11.25° for the 2'.25 and 3'.0 rings (32 positions each ring), producing an azimuthally oversampled ^{12}CO map. Figure 3.1 illustrates how the CO emission was mapped in the inner 5'.00 of this galaxy. To probe the CO contents in the outer disk of this galaxy, we have also made observations out to a radius of 7'.5 along the N-S strip, and out to a radius of 4'.5 at position angles of 45° and 225°. Thus, a total of 110 CO spectra have been obtained for NGC 6946. Line parameters for all of the CO observations are given in Table 3.1, and the smoothed spectra for the inner 6'.75 of the galaxy are shown in Figure 3.2, arranged by annulus. Each spectrum listed in Table 3.1 has been assigned a position number ordered by increasing radius (in the plane of the sky), and increasing position angle at a particular radius, for easy reference. Observation number 3-1, for example, refers to the spectrum at a radius of 1'.5 (*i.e.* the third annulus), and a position angle of 0°, while spectrum 4-5 is located at a radius of 2'.25 (4th annulus) and a position angle of 45°.

The uncertainties in the individual integrated intensities are contributed by both calibration and the rms noise in each spectrum. We have estimated that calibration

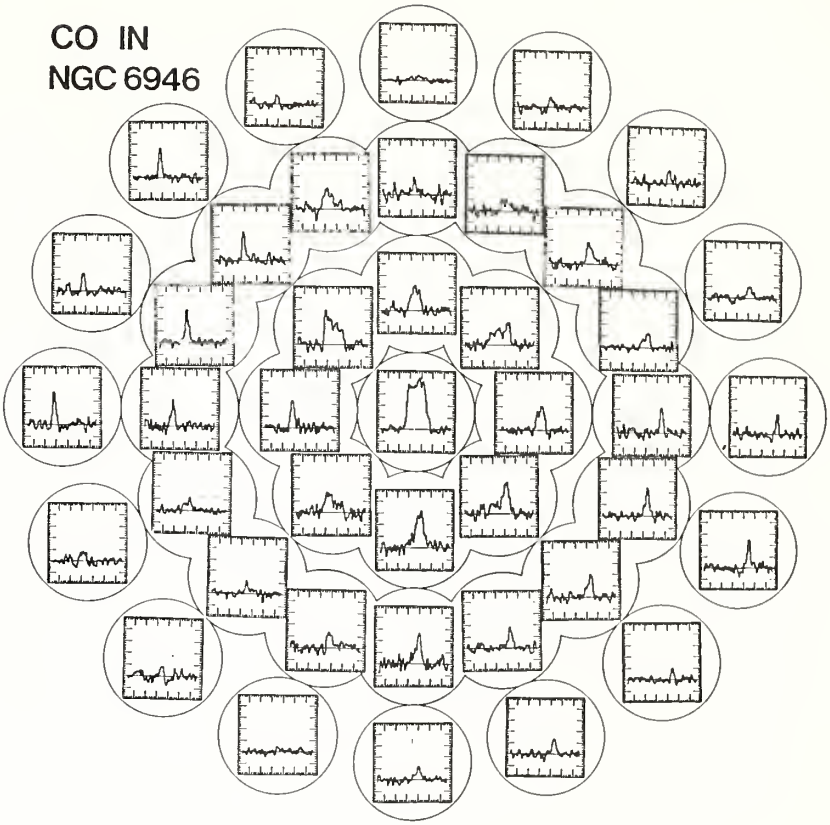

Figure 3.1: A sample of the CO spectra in NGC 6946, illustrating the observing scheme. The annuli shown here are at radii of 0'.75, 1'.50, and 2'.25; only half of the data in the 2'.25 annulus are represented. The V_{LSR} is plotted on the x-axis and runs from -300 to 400 km s^{-1} with each large tic mark representing 100 km s^{-1} increments. T_R^* is plotted on the y-axis and runs from -0.1 to 0.3 K km s^{-1} in steps of 0.05 K km s^{-1}. North is up on this figure.

Table 3.1

CO Observations

Explanation of columns in Table 3.1:

(1) The designation given to each spectrum by ring number and position angle as explained in the text.

(2) The RA and Dec offsets from the center of NGC 6946, center taken to be $20^h33^m48^s.8$ and +59°58'50" (Dressel and Condon 1976).

(3) The position angle of the observation measured from north through east.

(4) The peak antenna temperature measured in each spectrum after smoothing to 10 km s^{-1}. Values in parentheses are marginal (~3σ) detections. Upper limits are 2σ.

(5) The rms noise per channel in the smoothed spectra.

(6) The CO integrated intensity scaled as explained in the text. 3σ detections are given in parentheses, upper limits are 2σ.

(7) The estimated error in the CO integrated intensity.

(8) The measured mean velocity with respect to the sun.

Table 3.1

CO Observations

Observation Number (1)	$\Delta\alpha$ $\Delta\delta$ arcmin (2)	P.A. ° (3)	T_R^*(peak) mK (4)	rms mK (5)	$\int T_R^* dv$ K km s^{-1} (6)	$\sigma\int_I$ K km s^{-1} (7)	V_{mean} km s^{-1} (8)
0-0	0.00 0.00	0.00	310	9	48.4	3.9	42
1-1	0.00 0.38	0.00	200	36	26.7	2.6	35
1-2	0.38 0.00	90.00	260	37	26.3	2.6	25
1-3	0.00 -0.38	180.00	120	32	14.5	1.6	58
1-4	-0.38 0.00	270.00	180	33	21.9	2.2	59
2-1	0.00 0.75	0.00	150	14	12.0	1.1	21
2-2	0.53 0.53	45.00	200	14	21.1	1.7	29
2-3	0.75 0.00	90.00	160	13	7.04	1.06	-23
2-4	0.53 -0.53	135.00	120	16	12.8	1.9	38
2-5	0.00 -0.75	180.00	220	15	18.8	1.8	67
2-6	-0.53 -0.53	225.00	190	16	16.6	1.8	72
2-7	-0.75 0.00	270.00	140	10	9.68	1.30	96
2-8	-0.53 0.53	315.00	130	12	17.0	1.4	41
3-1	0.00 1.50	0.00	110	18	4.38	0.66	11
3-2	0.57 1.39	22.50	140	12	12.1	1.8	25
3-3	1.06 1.06	45.00	230	13	9.01	1.35	-12
3-4	1.39 0.57	67.50	190	11	7.34	1.10	-32
3-5	1.50 0.00	90.00	160	14	5.33	0.80	-24
3-6	1.39 -0.57	112.50	90	8	5.64	0.85	5
3-7	1.06 -1.06	135.00	110	11	4.44	0.67	51
3-8	0.57 -1.39	157.50	110	14	5.86	0.88	77
3-9	0.00 -1.50	180.00	190	18	11.4	1.7	65
3-10	-0.57 -1.39	202.50	140	13	6.42	0.96	111
3-11	-1.06 -1.06	225.00	140	14	7.39	1.11	109
3-12	-1.39 -0.57	247.50	170	11	7.42	1.11	119
3-13	-1.50 0.00	270.00	150	15	4.64	0.70	123
3-14	-1.39 0.57	292.50	90	10	5.52	0.83	98
3-15	-1.06 1.06	315.00	140	14	9.56	1.43	95
3-16	-0.57 1.39	337.50	90	16	7.17	1.08	57

(continued on next page)

Table 3.1
(continued)

Observation Number (1)	Δα Δδ arcmin (2)	P.A. ° (3)	T_R^*(peak) mK (4)	rms mK (5)	$\int T_R^* dv$ K km s^{-1} (6)	$\sigma\int I$ K km s^{-1} (7)	V_{mean} km s^{-1} (8)
4-1	0.00 2.25	0.00	(40)	13	(3.48)	0.73	(29)
4-2	0.44 2.21	11.25	100	13	6.21	0.93	4
4-3	0.86 2.08	22.50	60	9	2.37	0.36	-29
4-4	1.25 1.87	33.75	210	13	10.3	1.6	-37
4-5	1.59 1.59	45.00	180	11	5.68	0.85	-36
4-6	1.87 1.25	56.25	160	14	6.37	0.96	-39
4-7	2.08 0.86	67.50	120	13	3.90	0.59	-39
4-8	2.21 0.44	78.75	90	11	2.95	0.44	-40
4-9	2.25 0.00	90.00	190	14	5.99	0.90	-32
4-10	2.21 -0.44	101.25	130	10	4.19	0.63	-25
4-11	2.08 -0.86	112.50	70	12	3.52	0.53	-5
4-12	1.87 -1.25	123.75	110	12	4.62	0.69	16
4-13	1.59 -1.59	135.00	60	14	2.10	0.75	34
4-14	1.25 -1.87	146.25	80	10	2.47	0.37	37
4-15	0.86 -2.08	157.50	(30)	10	(1.28)	0.40	(44)
4-16	0.44 -2.21	168.75	40	8	1.59	0.24	58
4-17	0.00 -2.25	180.00	80	11	4.13	0.62	82
4-18	-0.44 -2.21	191.25	140	13	7.11	1.07	99
4-19	-0.86 -2.08	202.50	90	10	4.00	0.60	111
4-20	-1.25 -1.87	213.75	90	11	2.82	0.42	126
4-21	-1.59 -1.59	225.00	70	9	1.77	0.27	127
4-22	-1.87 -1.25	236.25	130	13	4.37	0.66	132
4-23	-2.08 -0.86	247.50	170	11	6.76	1.01	133
4-24	-2.21 -0.44	258.75	160	12	5.76	0.86	127
4-25	-2.25 0.00	270.00	120	13	3.07	0.46	115
4-26	-2.21 0.44	281.25	110	10	6.13	0.92	108
4-27	-2.08 0.86	292.50	80	11	4.49	0.67	100
4-28	-1.87 1.25	303.75	140	14	8.34	1.25	72
4-29	-1.59 1.59	315.00	90	13	3.42	0.51	71
4-30	-1.25 1.87	326.25	40	10	2.64	0.40	36
4-31	-0.86 2.08	337.50	60	11	2.58	0.39	32
4-32	-0.44 2.21	348.75	40	9	1.95	0.29	-8

(continued on next page)

Table 3.1
(continued)

Observation Number (1)	Δα Δδ arcmin (2)	P.A. ° (3)	T_R^* (peak) mK (4)	rms mK (5)	$\int T_R^* dv$ K km s^{-1} (6)	$\sigma\int_I$ K km s^{-1} (7)	V_{mean} km s^{-1} (8)
5-1	0.00 3.00	0.00	<20	10	<1.09	0.55	---
5-2	0.59 2.94	11.25	<20	10	<0.96	0.49	---
5-3	1.15 2.77	22.50	80	14	4.50	0.68	-31
5-4	1.67 2.49	33.75	<20	10	<0.82	0.41	---
5-5	2.12 2.12	45.00	50	12	2.34	0.39	-51
5-6	2.49 1.67	56.25	70	8	2.77	0.42	-51
5-7	2.77 1.15	67.50	160	12	5.66	0.85	-56
5-8	2.94 0.59	78.75	140	10	3.99	0.60	-52
5-9	3.00 0.00	90.00	80	13	3.41	0.53	-39
5-10	2.94 -0.59	101.25	90	9	3.90	0.59	-39
5-11	2.77 -1.15	112.50	(40)	13	(1.63)	0.68	(-18)
5-12	2.49 -1.67	123.75	(40)	10	(0.87)	0.23	(-13)
5-13	2.12 -2.12	135.00	60	10	2.64	0.40	26
5-14	1.67 -2.49	146.25	60	11	2.40	0.36	37
5-15	1.15 -2.77	157.50	(40)	13	(0.79)	0.24	66
5-16	0.59 -2.94	168.75	<40	20	<1.16	0.58	---
5-17	0.00 -3.00	180.00	<20	10	<1.74	0.87	---
5-18	-0.59 -2.94	191.25	50	9	1.34	0.22	119
5-19	-1.15 -2.77	202.50	80	13	1.31	0.23	124
5-20	-1.67 -2.49	213.75	50	8	1.97	0.30	135
5-21	-2.12 -2.12	225.00	70	8	2.94	0.44	153
5-22	-2.49 -1.67	236.25	90	7	3.14	0.47	134
5-23	-2.77 -1.15	247.50	70	8	2.46	0.37	140
5-24	-2.94 -0.59	258.75	100	11	3.77	0.57	137
5-25	-3.00 0.00	270.00	50	10	2.61	0.39	130
5-26	-2.94 0.59	281.25	(50)	16	(1.13)	0.35	(104)
5-27	-2.77 1.15	292.50	110	11	6.70	1.01	92
5-28	-2.49 1.67	303.75	(50)	13	(1.55)	0.52	(69)
5-29	-2.12 2.12	315.00	60	15	2.30	0.40	63
5-30	-1.67 2.49	326.25	60	10	2.38	0.36	48
5-31	-1.15 2.77	337.50	50	10	2.10	0.36	27
5-32	-0.59 2.94	348.75	(30)	9	(0.85)	0.30	(25)

(continued on next page)

Table 3.1
(continued)

Observation Number (1)	$\Delta\alpha$ $\Delta\delta$ arcmin (2)	P.A. ° (3)	T_R^* (peak) mK (4)	rms mK (5)	$\int T_R^* dv$ K km s^{-1} (6)	$\sigma\int_I$ K km s^{-1} (7)	V_{mean} km s^{-1} (8)
6-1	0.00 3.75	0.00	(40)	16	(1.14)	0.38	(-6)
6-2	2.65 2.65	45.00	<30	15	<0.72	0.36	---
6-3	0.00 -3.75	180.00	60	18	1.35	0.22	89
6-4	-2.65 -2.65	225.00	(40)	13	(0.89)	0.30	(164)
6-5	0.00 4.50	0.00	<20	10	<0.59	0.29	---
6-6	3.18 3.18	45.00	<30	15	<0.88	0.44	---
6-7	0.00 -4.50	180.00	<20	10	<0.52	0.26	---
6-8	-3.18 -3.18	225.00	<40	13	<0.70	0.35	---
6-9	0.00 5.25	0.00	<30	15	<0.50	0.25	---
6-10	3.71 3.71	45.00	<20	10	<0.72	0.36	---
6-11	0.00 -5.25	180.00	<20	10	<0.38	0.19	---
6-12	-3.71 -3.71	225.00	<20	10	<0.59	0.29	---
6-13	0.00 6.00	0.00	<30	15	<0.42	0.21	---
6-14	0.00 -6.00	180.00	<20	10	<0.58	0.29	---
6-15	0.00 6.75	0.00	<20	10	<0.38	0.19	---
6-16	0.00 -6.75	180.00	<30	15	<0.80	0.40	---
6-17	0.00 7.50	0.00	40	6	0.93	0.15	101

Figures 3.2a-l: CO spectra for each annulus in NGC 6946 smoothed to a velocity resolution of 10 km s^{-1}. The velocities have all been corrected to a heliocentric reference frame. Position angles are indicated every 45° where possible.

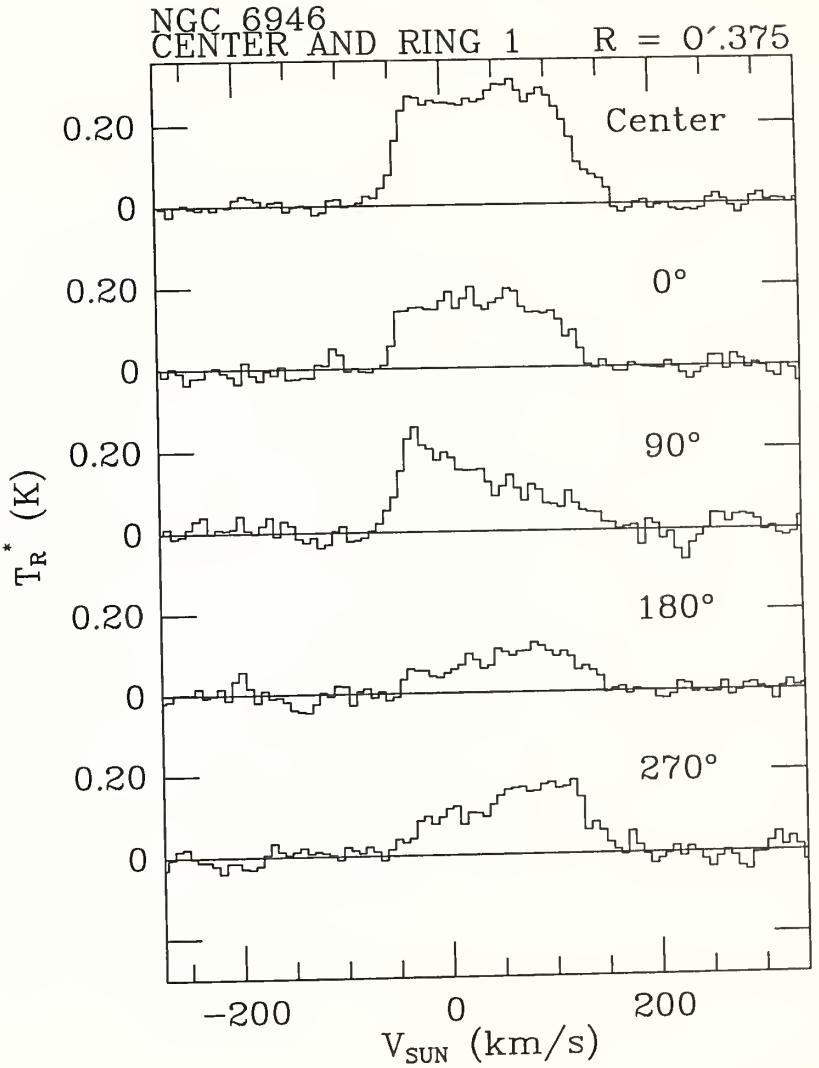

(continued on next page)

(Figure 3.2 continued)

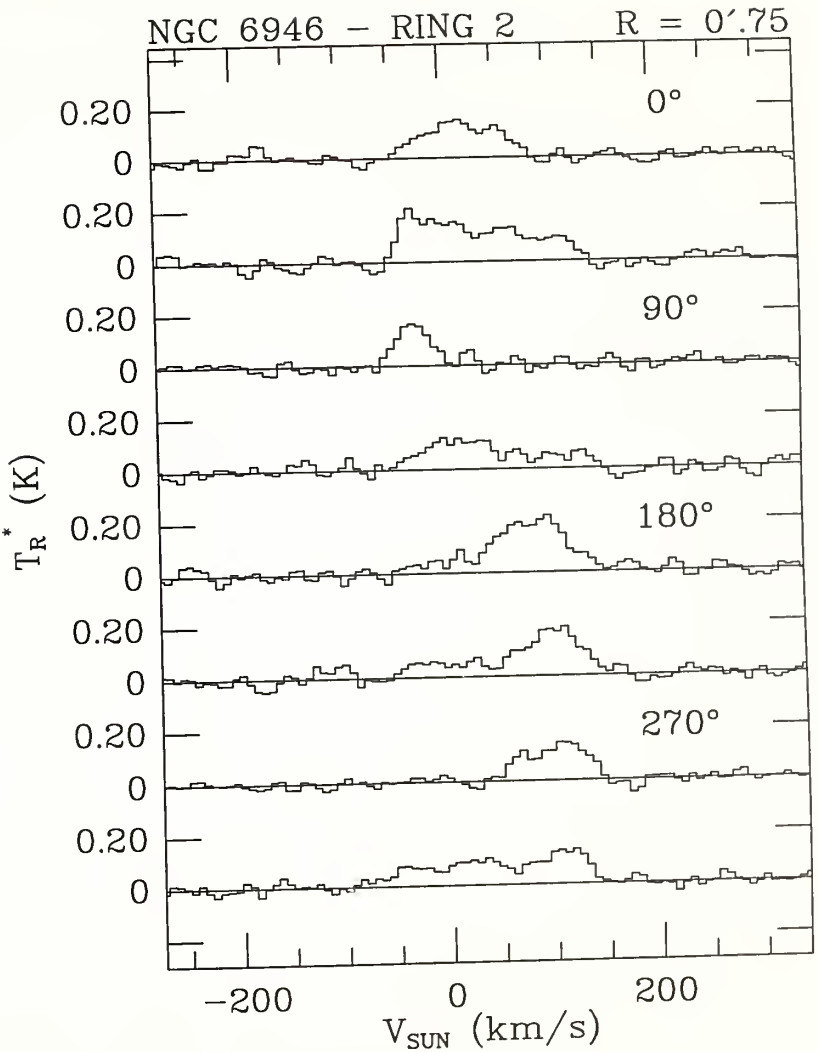

(continued on next page)

(Figure 3.2 continued)

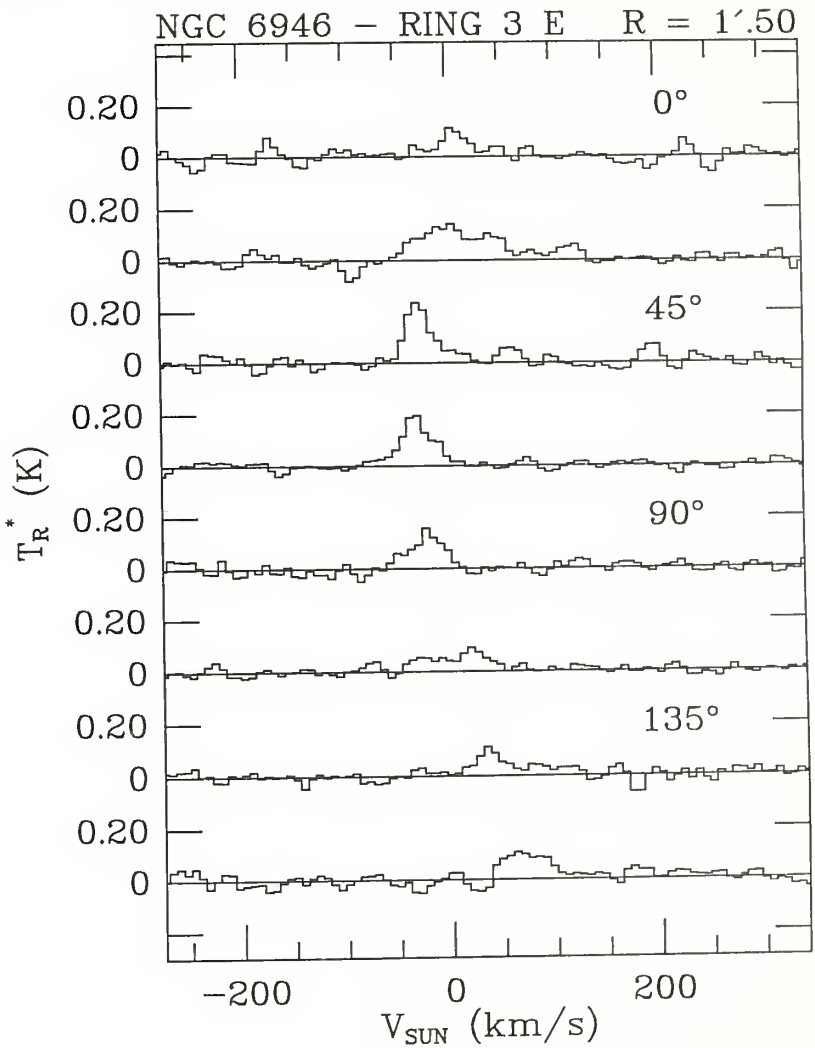

(continued on next page)

(Figure 3.2 continued)

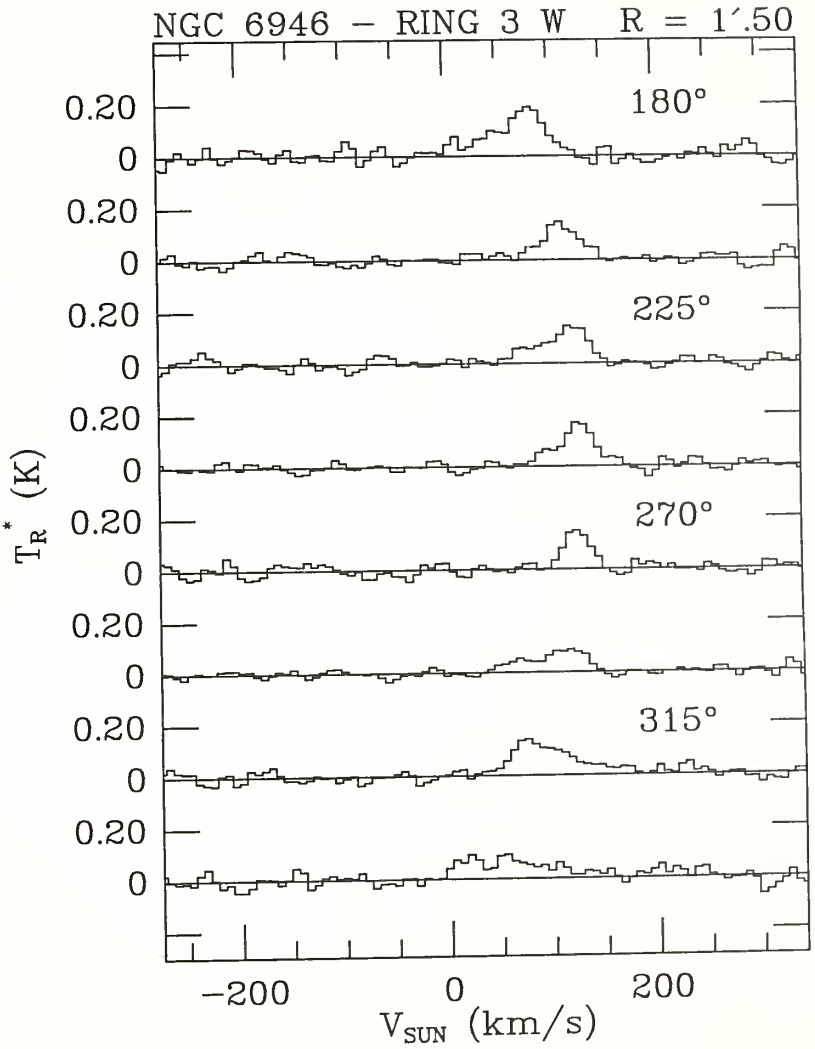

(continued on next page)

(Figure 3.2 continued)

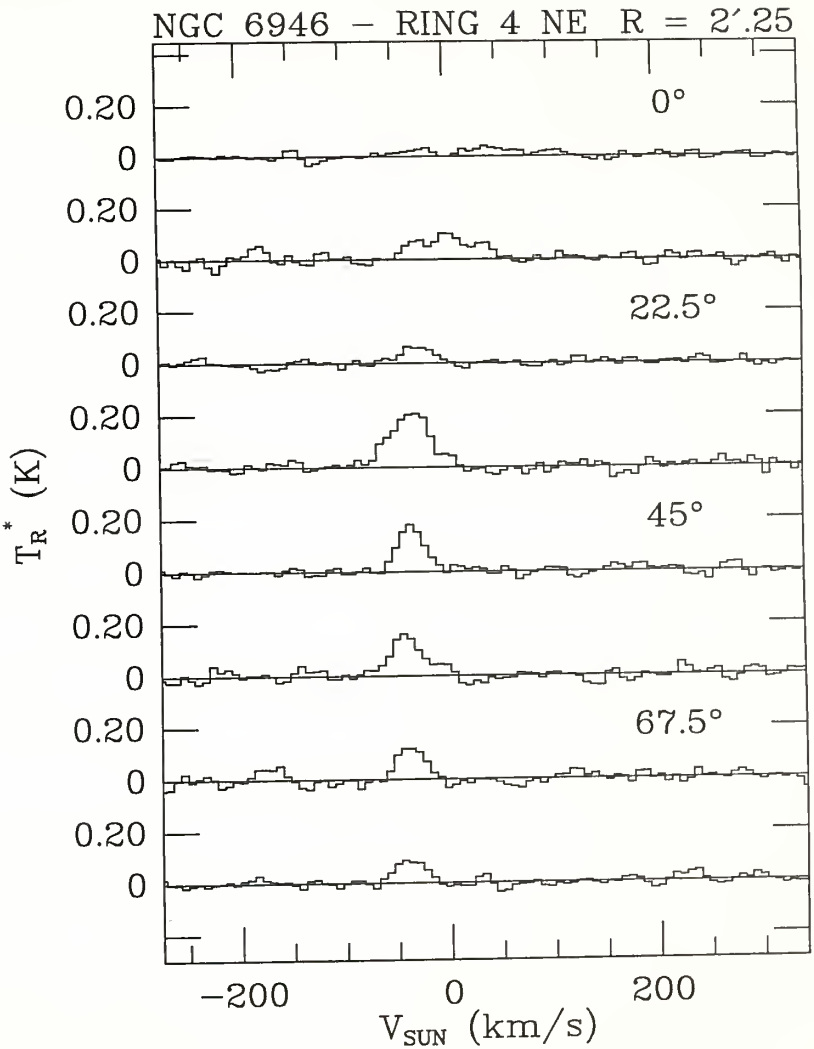

(continued on next page)

(Figure 3.2 continued)

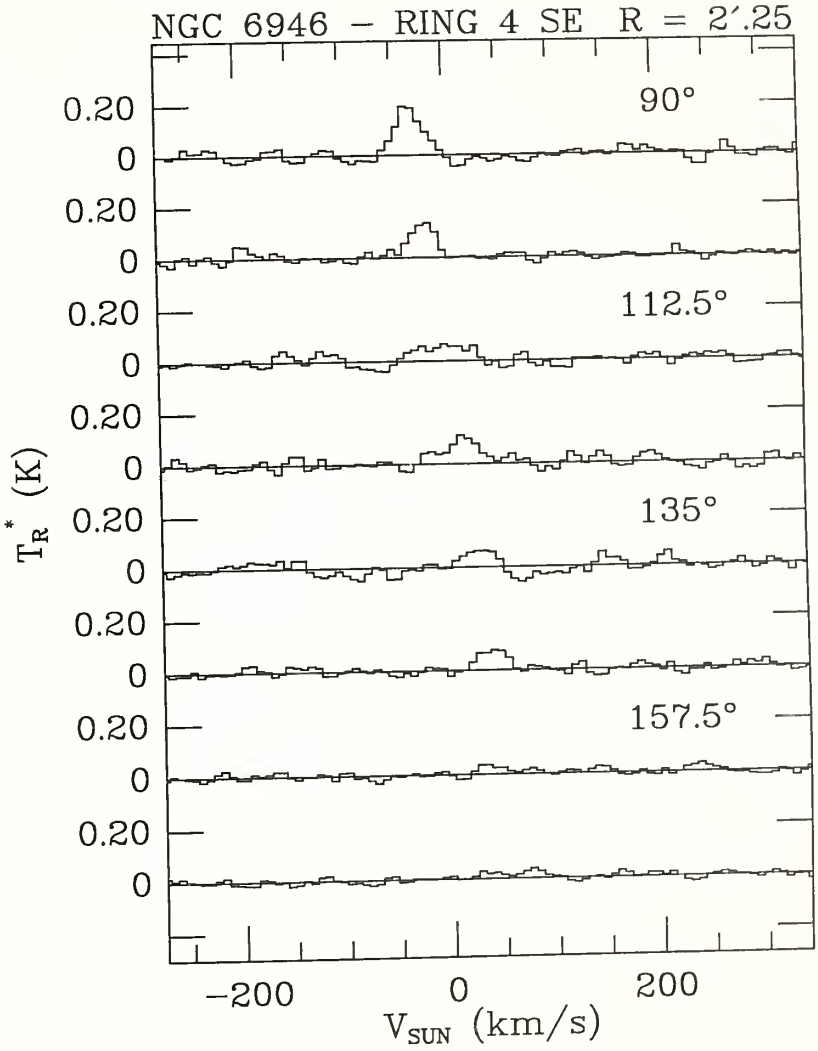

(continued on next page)

(Figure 3.2 continued)

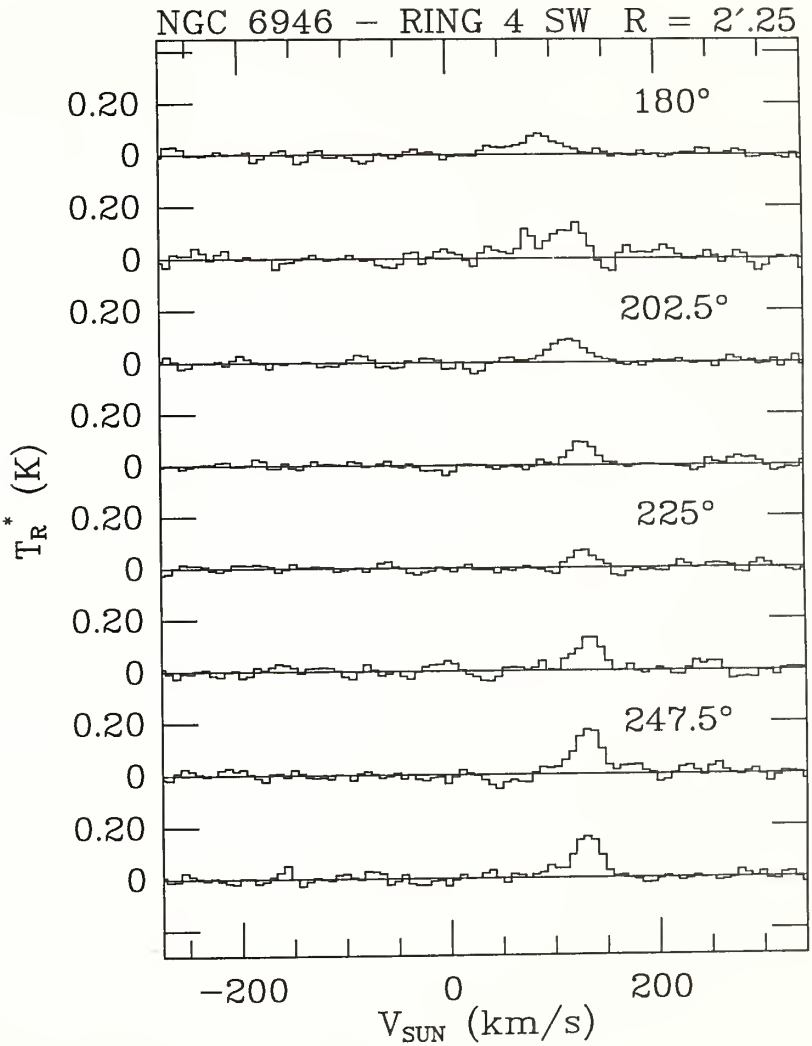

(continued on next page)

(Figure 3.2 continued)

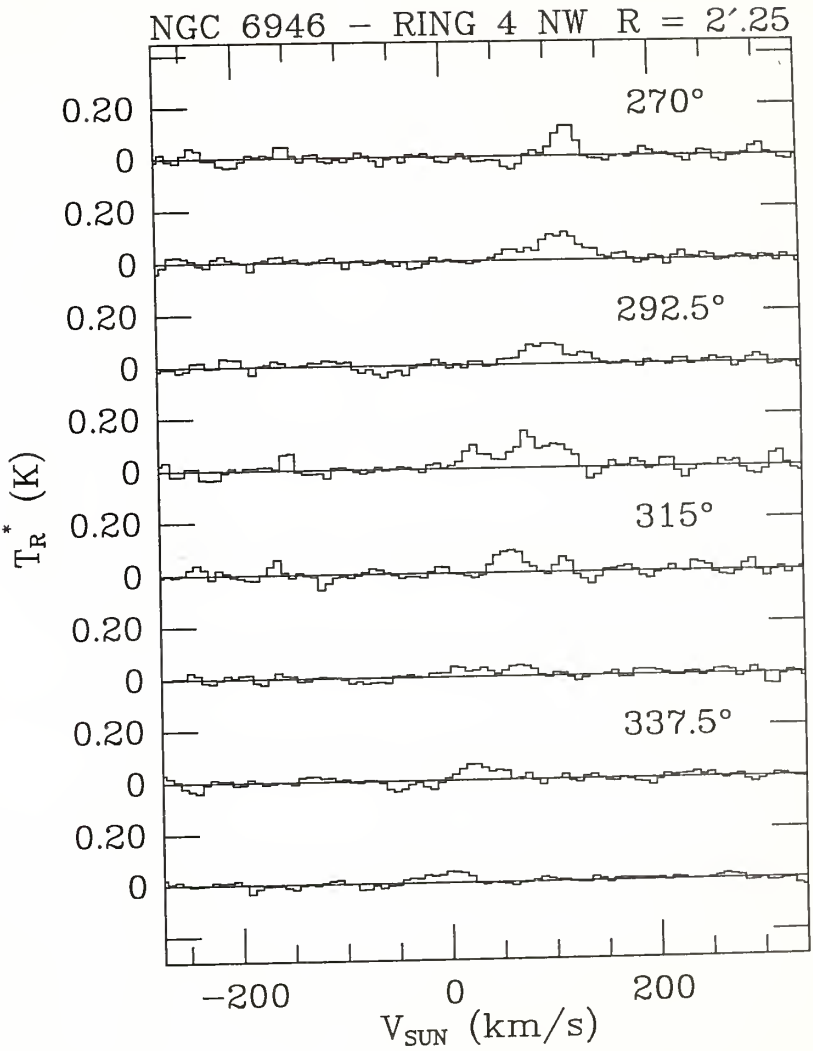

(continued on next page)

(Figure 3.2 continued)

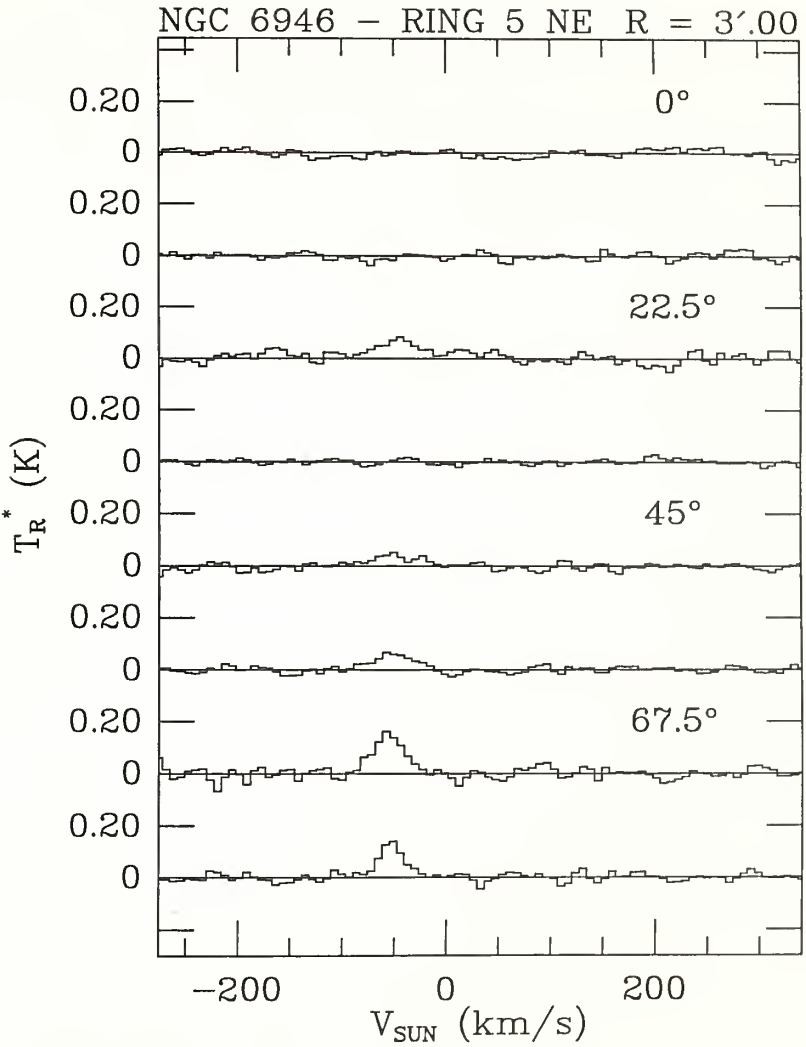

(continued on next page)

(Figure 3.2 continued)

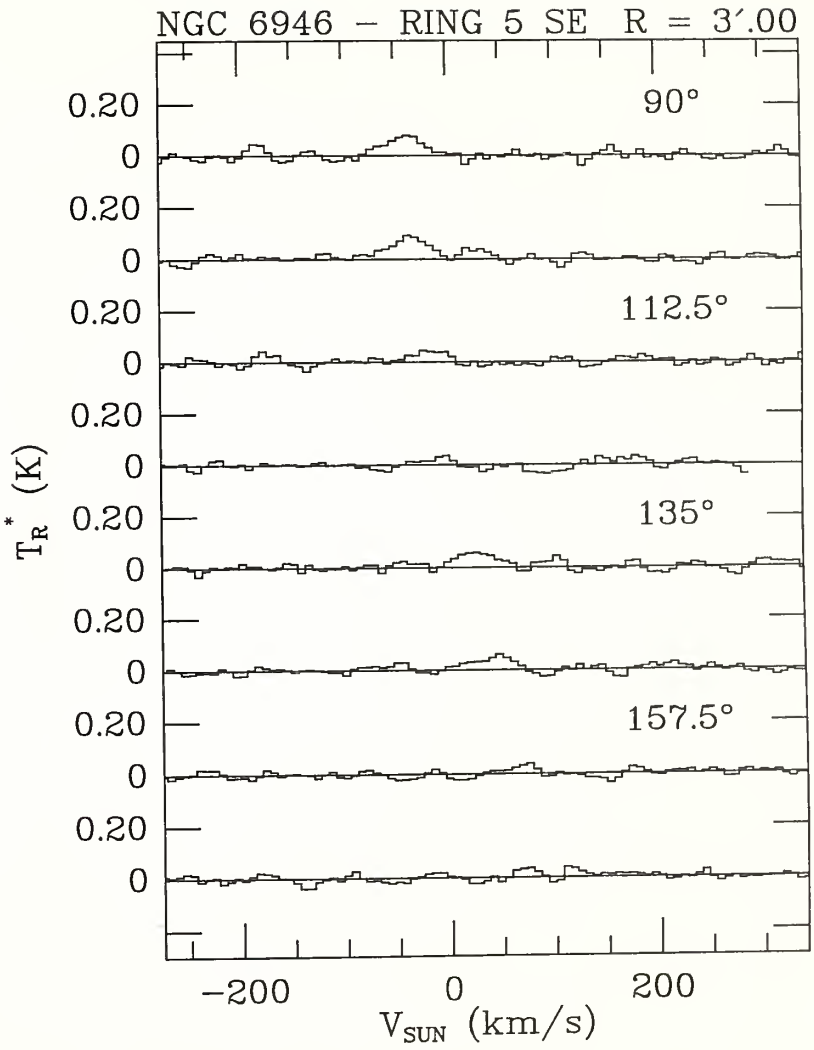

(continued on next page)

(Figure 3.2 continued)

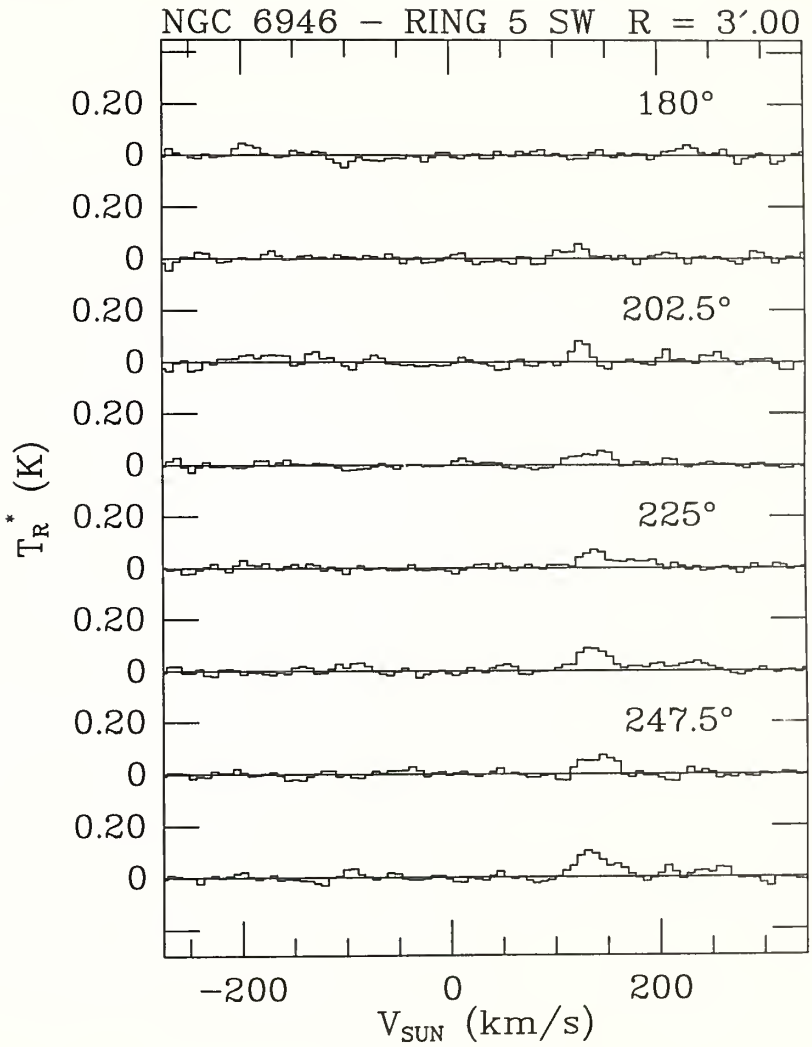

(continued on next page)

(Figure 3.2 continued)

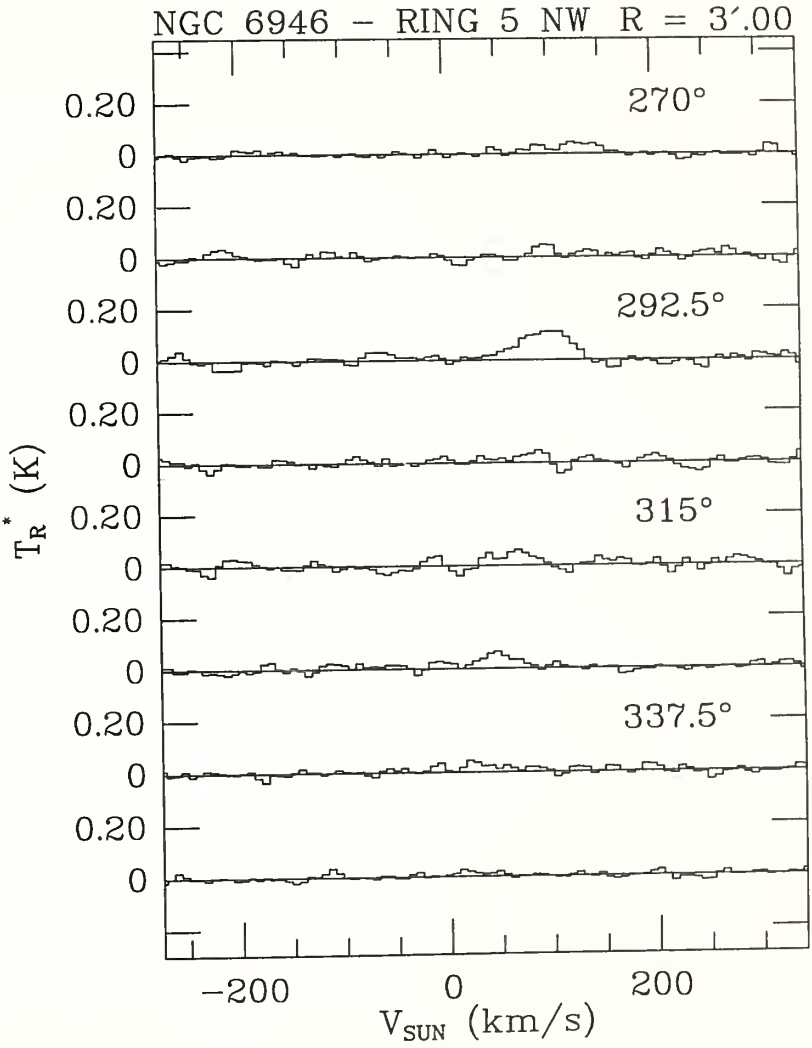

uncertainties are ±8% based on repeated observations of Orion KL. This is consistent with the observed dispersion in the central integrated intensities in NGC 6946. The uncertainties due to the rms noise (T_{rms}) depend not only on T_{rms}, but also on the linewidth of the spectrum by

$$\sigma\int_I = T_{rms}\sqrt{W_{20}\Delta V} \tag{3.1}$$

where W_{20} is the measured linewidth of the spectrum at the 20% level, and ΔV is the velocity resolution of one channel (10 km s^{-1} for our observations). The uncertainties which are quoted in Table 3.1 are the quadrature sum of the 8% calibration and the 1σ rms uncertainties.

3.2.2 HI Data

The HI observations have been described fully in Chapter 2. The data have been further reduced here for comparison with the CO map. The HI image was corrected for the primary beam attenuation of the 25-meter antennas used at the VLA. In order to compare the HI and CO data, the HI spectral line cube was convolved with a 45" circular gaussian beam using a 2D FFT algorithm written for the AIPS data reduction package. HI integrated fluxes and mean velocities were then calculated from the 45" resolution data base; HI fluxes quoted here will thus differ slightly from those given in Chapter 2. The HI integrated flux, rms, and mean velocity for each of the 110 positions at which CO observations were made are presented in Table 3.2.

Table 3.2

HI Observations

Explanation of columns in Table 3.2:

(1)-(3) are the same as those in Table 3.1.

(4) The integrated HI flux. 3σ detections are given in parentheses; upper limits are 2σ.

(5) The rms in the HI integrated flux.

(6) HI mean velocities with respect to the sun.

Table 3.2

HI Observations

Observation Number (1)	$\Delta\alpha$ $\Delta\delta$ arcmin (2)	P.A. ° (3)	S_{HI} Jy km s^{-1} (4)	ΔS_{HI} Jy km s^{-1} (5)	V_{mean} km s^{-1} (6)
0-0	0.00 0.00	0.00	0.51	0.087	93
1-1	0.00 0.38	0.00	0.99	0.092	66
1-2	0.38 0.00	90.00	0.41	0.092	21
1-3	0.00 -0.38	180.00	1.07	0.092	84
1-4	-0.38 0.00	270.00	0.70	0.080	116
2-1	0.00 0.75	0.00	1.29	0.079	51
2-2	0.53 0.53	45.00	0.70	0.092	16
2-3	0.75 0.00	90.00	0.63	0.090	-2
2-4	0.53 -0.53	135.00	1.00	0.077	39
2-5	0.00 -0.75	180.00	1.47	0.093	86
2-6	-0.53 -0.53	225.00	0.75	0.078	126
2-7	-0.75 0.00	270.00	0.82	0.074	121
2-8	-0.53 0.53	315.00	1.30	0.085	86
3-1	0.00 1.50	0.00	1.09	0.070	26
3-2	0.57 1.39	22.50	1.23	0.087	8
3-3	1.06 1.06	45.00	0.94	0.074	-12
3-4	1.39 0.57	67.50	1.16	0.067	-22
3-5	1.50 0.00	90.00	0.97	0.074	-8
3-6	1.39 -0.57	112.50	1.10	0.075	16
3-7	1.06 -1.06	135.00	1.35	0.070	43
3-8	0.57 -1.39	157.50	1.69	0.089	72
3-9	0.00 -1.50	180.00	1.90	0.086	98
3-10	-0.57 -1.39	202.50	1.56	0.084	126
3-11	-1.06 -1.06	225.00	1.36	0.068	143
3-12	-1.39 -0.57	247.50	1.36	0.072	146
3-13	-1.50 0.00	270.00	1.31	0.087	129
3-14	-1.39 0.57	292.50	1.41	0.082	101
3-15	-1.06 1.06	315.00	1.32	0.077	74
3-16	-0.57 1.39	337.50	1.06	0.071	41

(continued on next page)

Table 3.2
(continued)

Observation Number (1)	$\Delta\alpha$ $\Delta\delta$ arcmin (2)	P.A. ° (3)	S_{HI} Jy km s^{-1} (4)	ΔS_{HI} Jy km s^{-1} (5)	V_{mean} km s^{-1} (6)
4-1	0.00 2.25	0.00	0.78	0.069	12
4-2	0.44 2.21	11.25	0.63	0.065	0
4-3	0.86 2.08	22.50	1.05	0.075	-16
4-4	1.25 1.87	33.75	1.73	0.078	-26
4-5	1.59 1.59	45.00	2.09	0.075	-31
4-6	1.87 1.25	56.25	1.80	0.075	-33
4-7	2.08 0.86	67.50	1.51	0.075	-33
4-8	2.21 0.44	78.75	1.44	0.075	-32
4-9	2.25 0.00	90.00	1.60	0.073	-24
4-10	2.21 -0.44	101.25	1.65	0.076	-8
4-11	2.08 -0.86	112.50	1.28	0.071	11
4-12	1.87 -1.25	123.75	1.52	0.078	31
4-13	1.59 -1.59	135.00	1.46	0.069	41
4-14	1.25 -1.87	146.25	1.00	0.069	54
4-15	0.86 -2.08	157.50	1.09	0.075	75
4-16	0.44 -2.21	168.75	1.42	0.075	91
4-17	0.00 -2.25	180.00	1.73	0.072	107
4-18	-0.44 -2.21	191.25	1.95	0.071	123
4-19	-0.86 -2.08	202.50	1.87	0.076	136
4-20	-1.25 -1.87	213.75	1.46	0.070	144
4-21	-1.59 -1.59	225.00	1.22	0.072	151
4-22	-1.87 -1.25	236.25	1.63	0.068	159
4-23	-2.08 -0.86	247.50	1.80	0.075	155
4-24	-2.21 -0.44	258.75	1.39	0.093	141
4-25	-2.25 0.00	270.00	1.31	0.078	127
4-26	-2.21 0.44	281.25	1.41	0.094	116
4-27	-2.08 0.86	292.50	1.44	0.071	105
4-28	-1.87 1.25	303.75	1.44	0.076	90
4-29	-1.59 1.59	315.00	1.33	0.075	78
4-30	-1.25 1.87	326.25	1.65	0.093	63
4-31	-0.86 2.08	337.50	1.51	0.088	40
4-32	-0.44 2.21	348.75	1.17	0.072	26

(continued on next page)

Table 3.2
(continued)

Observation Number (1)	$\Delta\alpha$ $\Delta\delta$ arcmin (2)	P.A. ° (3)	S_{HI} Jy km s^{-1} (4)	ΔS_{HI} Jy km s^{-1} (5)	V_{mean} km s^{-1} (6)
5-1	0.00 3.00	0.00	1.31	0.075	12
5-2	0.59 2.94	11.25	1.29	0.081	-5
5-3	1.15 2.77	22.50	1.26	0.077	-26
5-4	1.67 2.49	33.75	1.56	0.069	-41
5-5	2.12 2.12	45.00	2.06	0.084	-48
5-6	2.49 1.67	56.25	1.91	0.070	-47
5-7	2.77 1.15	67.50	2.22	0.070	-43
5-8	2.94 0.59	78.75	2.10	0.077	-40
5-9	3.00 0.00	90.00	1.89	0.080	-28
5-10	2.94 -0.59	101.25	2.00	0.070	-11
5-11	2.77 -1.15	112.50	1.21	0.080	7
5-12	2.49 -1.67	123.75	1.37	0.068	24
5-13	2.12 -2.12	135.00	1.74	0.067	37
5-14	1.67 -2.49	146.25	1.90	0.077	54
5-15	1.15 -2.77	157.50	1.57	0.069	69
5-16	0.59 -2.94	168.75	1.26	0.074	86
5-17	0.00 -3.00	180.00	1.38	0.068	102
5-18	-0.59 -2.94	191.25	1.63	0.077	123
5-19	-1.15 -2.77	202.50	1.61	0.083	146
5-20	-1.67 -2.49	213.75	1.33	0.068	155
5-21	-2.12 -2.12	225.00	1.61	0.079	160
5-22	-2.49 -1.67	236.25	1.36	0.080	164
5-23	-2.77 -1.15	247.50	1.52	0.082	162
5-24	-2.94 -0.59	258.75	1.59	0.081	149
5-25	-3.00 0.00	270.00	0.86	0.086	137
5-26	-2.94 0.59	281.25	0.93	0.067	118
5-27	-2.77 1.15	292.50	2.03	0.075	109
5-28	-2.49 1.67	303.75	3.00	0.076	95
5-29	-2.12 2.12	315.00	3.06	0.082	79
5-30	-1.67 2.49	326.25	2.54	0.077	62
5-31	-1.15 2.77	337.50	1.85	0.064	45
5-32	-0.59 2.94	348.75	1.49	0.065	30

(continued on next page)

Table 3.2
(continued)

Observation Number (1)	$\Delta\alpha$ $\Delta\delta$ arcmin (2)	P.A. ° (3)	S_{HI} Jy km s^{-1} (4)	ΔS_{HI} Jy km s^{-1} (5)	V_{mean} km s^{-1} (6)
6-1	0.00 3.75	0.00	1.08	0.056	14
6-2	2.65 2.65	45.00	1.28	0.052	-55
6-3	0.00 -3.75	180.00	1.88	0.054	97
6-4	-2.65 -2.65	225.00	0.86	0.074	157
6-5	0.00 4.50	0.00	(0.21)	0.053	(25)
6-6	3.18 3.18	45.00	0.70	0.052	-49
6-7	0.00 -4.50	180.00	1.19	0.053	94
6-8	-3.18 -3.18	225.00	0.95	0.048	162
6-9	0.00 5.25	0.00	0.21	0.042	24
6-10	3.71 3.71	45.00	0.37	0.044	-40
6-11	0.00 -5.25	180.00	0.72	0.045	93
6-12	-3.71 -3.71	225.00	1.27	0.047	165
6-13	0.00 6.00	0.00	0.97	0.049	20
6-14	0.00 -6.00	180.00	1.10	0.046	98
6-15	0.00 6.75	0.00	1.29	0.057	28
6-16	0.00 -6.75	180.00	0.91	0.047	103
6-17	0.00 7.50	0.00	0.99	0.050	37

3.2.3 Optical Data

Sky subtracted B and I band images of NGC 6946 have been kindly provided to us by Drs. B. Elmegreen and D. Elmegreen. In their program, Elmegreen and Elmegreen observed observed 34 spiral galaxies, including NGC 6946, in the blue (B, λ_{eff}~4360 Angstroms) and near IR (I, λ_{eff}~8250 Angstroms) passbands with the Palomar 1.2 meter Schmidt telescope. The I-band is nearly free of radiation from HII regions and OB stars, and is thus sensitive to the old stellar population. I-band images are thus useful to trace out the old stellar spiral arms in a galaxy; such spiral structure presumably represents regions of enhanced mass surface density. The B-band emission arises from both the old stellar population and stars $\leq 10^9$ years old (see Chapter 4). A full description of the reduction of the B- and I-band images is given in Elmegreen and Elmegreen (1984).

Since the sky background is bright in the I-band, long exposures are necessary to achieve a good signal-to-noise ratio. Typical exposure times of 1.5 to 2 hours were necessary for Elmegreen and Elmegreen's I-band plates, in order to discern whether spiral structure was evident in the disks of these galaxies. In contrast, exposure times of 10 to 12 minutes were generally sufficient for the blue plates.

Elmegreen and Elmegreen digitized the plates into a density position raster of dimension 512×512 pixels with a microdensitometer, using apertures which ranged from 20μm to 80μm. For NGC 6946, the resulting resolution of both the B and I band images is 2 arcsec pixel^{-1}. They then converted the photographic densities to relative

B and I intensities using calibration wedges which were photographed in the same passbands as the galaxy. We have determined the B- and I-band surface brightnesses in 45" apertures with gaussian weighting at the same positions where CO observations were made, such that the B and I fluxes could be directly compared with the CO and HI fluxes described above. These surface brightnesses are given in Table 3.3.

3.3 Results

3.3.1 CO Integrated Intensities

The distribution of CO integrated intensity with galactic radius in NGC 6946 for all 110 CO positions is shown in Figure 3.3. The true central 45" integrated intensity is plotted off scale to highlight the CO emission in the disk. The CO integrated intensities peak in the center of the galaxy and then fall off fairly smoothly with radius as found previously (Young and Scoville 1982a; Morris and Rickard 1982). At a particular radius, however, there is a scatter of up to a factor of three relative to the mean value, which shows that the CO emission , like HI (see Chapter 2), is *not* azimuthally symmetric in the disk of NGC 6946. We have computed the azimuthally averaged radial distribution of CO in NGC 6946 as indicated by the dashed line in Figure 3.3; the average CO integrated intensity in each annulus is indicated by an ×.

Figure 3.4a shows a contour map of the CO integrated intensities observed in NGC 6946 superposed on the blue image (Elmegreen and Elmegreen). The CO map was made by interpolating a regularly spaced grid from our irregularly spaced data, using an interpolation scheme written for the NCAR data reduction package. The grid

Table 3.3

CO, HI and Optical
Surface Densities and Surface Brightnesses

Explanation of columns in Table 3.3:

(1) The observation designation as given in the previous tables.

(2) and (3) The H_2 surface densities and associated 1σ uncertainties calculated using the $CO \rightarrow H_2$ conversion factor of Bloemen *et al.* (1986), and $\nu_c = 0.7$. Upper limits are 2σ.

(4) and (5) The HI surface densities and associated 1σ uncertainties.

(6) and (7) Relative Blue and I band surface brightnesses. B_0 and I_0 are defined to be the surface brightnesses of the central 45" of the B and I images respectively.

Table 3.3

CO, HI, and Optical
Surface Densities and Surface Brightnesses

Observation Number	N_{H_2}	σ_{H_2}	N_{HI}	σ_{HI}	B/B_o	I/I_o
		(10^{21} atoms cm^{-2})				
(1)	(2)	(3)	(4)	(5)	(6)	(7)
0-0	33.5	5.0	0.355	0.060	1.00	1.00
1-1	18.5	2.8	0.688	0.064	0.967	0.823
1-2	18.2	2.7	0.285	0.064	0.804	0.824
1-3	10.0	1.5	0.744	0.065	0.852	0.890
1-4	15.2	2.3	0.487	0.056	0.926	0.834
2-1	8.34	1.3	0.897	0.055	0.900	0.633
2-2	14.7	2.2	0.487	0.064	0.749	0.626
2-3	4.88	0.73	0.438	0.063	0.659	0.571
2-4	8.85	1.33	0.695	0.054	0.668	0.591
2-5	13.0	2.0	1.02	0.07	0.760	0.668
2-6	11.5	1.7	0.521	0.054	0.718	0.664
2-7	6.71	1.01	0.570	0.051	0.730	0.586
2-8	11.8	1.8	0.904	0.059	0.804	0.548
3-1	3.04	0.46	0.758	0.049	0.703	0.352
3-2	8.38	1.26	0.855	0.060	0.707	0.406
3-3	6.24	0.94	0.654	0.051	0.655	0.425
3-4	5.09	0.76	0.807	0.047	0.576	0.392
3-5	3.69	0.55	0.674	0.051	0.465	0.343
3-6	3.91	0.59	0.765	0.052	0.406	0.314
3-7	3.08	0.46	0.939	0.049	0.456	0.326
3-8	4.06	0.61	1.18	0.06	0.542	0.381
3-9	7.86	1.18	1.32	0.06	0.655	0.435
3-10	4.45	0.67	1.09	0.06	0.689	0.438
3-11	5.12	0.77	0.945	0.047	0.577	0.403
3-12	5.14	0.77	0.945	0.050	0.596	0.403
3-13	3.22	0.49	0.911	0.061	0.594	0.372
3-14	3.82	0.58	0.980	0.057	0.481	0.299
3-15	6.62	0.99	0.918	0.054	0.420	0.257
3-16	4.97	0.75	0.737	0.049	0.532	0.278

(continued on next page)

Table 3.3
(continued)

Observation Number	N_{H_2}	σ_{H_2}	N_{HI}	σ_{HI}	B/B_o	I/I_o
		(10^{21} atoms cm^{-2})				
(1)	(2)	(3)	(4)	(5)	(6)	(7)
4-1	(2.41)	0.36	0.542	0.048	0.302	0.172
4-2	4.30	0.64	0.438	0.045	0.371	0.198
4-3	1.64	0.25	0.730	0.052	0.410	0.225
4-4	7.14	1.07	1.20	0.05	0.510	0.267
4-5	3.94	0.59	1.45	0.05	0.597	0.315
4-6	4.41	0.67	1.25	0.05	0.536	0.313
4-7	2.70	0.41	1.05	0.05	0.520	0.305
4-8	2.04	0.31	1.00	0.05	0.562	0.316
4-9	4.15	0.62	1.11	0.05	0.536	0.309
4-10	2.90	0.44	1.15	0.05	0.464	0.291
4-11	2.44	0.37	0.890	0.049	0.378	0.254
4-12	3.20	0.48	1.06	0.05	0.324	0.230
4-13	(1.46)	0.52	1.02	0.05	0.293	0.211
4-14	1.71	0.26	0.695	0.048	0.253	0.202
4-15	(0.89)	0.17	0.758	0.052	0.263	0.211
4-16	1.10	0.17	0.987	0.052	0.293	0.221
4-17	2.86	0.43	1.20	0.05	0.331	0.239
4-18	4.93	0.74	1.36	0.05	0.388	0.273
4-19	2.77	0.42	1.30	0.05	0.477	0.335
4-20	1.95	0.29	1.02	0.05	0.565	0.364
4-21	1.23	0.19	0.848	0.050	0.503	0.310
4-22	3.03	0.46	1.13	0.05	0.487	0.303
4-23	4.68	0.70	1.25	0.05	0.546	0.311
4-24	3.99	0.60	0.966	0.065	0.507	0.288
4-25	2.13	0.32	0.911	0.054	0.483	0.281
4-26	4.25	0.64	0.980	0.065	0.523	0.289
4-27	3.11	0.46	1.00	0.05	0.512	0.288
4-28	5.78	0.87	1.00	0.05	0.393	0.246
4-29	2.37	0.35	0.925	0.052	0.307	0.208
4-30	1.83	0.28	1.15	0.07	0.246	0.180
4-31	1.79	0.27	1.05	0.06	0.203	0.158
4-32	1.35	0.20	0.813	0.050	0.227	0.159

(continued on next page)

Table 3.3
(continued)

Observation Number	N_{H_2}	σ_{H_2}	N_{HI}	σ_{HI}	B/B_o	I/I_o
		(10^{21} atoms cm^{-2})				
(1)	(2)	(3)	(4)	(5)	(6)	(7)
5-1	<0.76	0.38	0.911	0.052	0.224	0.135
5-2	<0.67	0.34	0.897	0.056	0.219	0.143
5-3	3.12	0.47	0.876	0.05	0.206	0.134
5-4	<0.57	0.28	1.09	0.05	0.276	0.153
5-5	1.62	0.27	1.43	0.06	0.463	0.214
5-6	1.92	0.29	1.33	0.05	0.591	0.281
5-7	3.92	0.59	1.54	0.05	0.506	0.253
5-8	2.76	0.42	1.46	0.05	0.387	0.221
5-9	2.36	0.37	1.31	0.06	0.334	0.202
5-10	2.70	0.41	1.39	0.05	0.248	0.182
5-11	(1.13)	0.47	0.841	0.056	0.210	0.160
5-12	(0.60)	0.16	0.952	0.047	0.269	0.169
5-13	1.83	0.28	1.21	0.05	0.277	0.174
5-14	1.66	0.25	1.32	0.05	0.216	0.160
5-15	(0.55)	0.17	1.11	0.05	0.181	0.149
5-16	<0.80	0.40	0.876	0.051	0.206	0.157
5-17	<1.21	0.60	0.959	0.047	0.280	0.176
5-18	0.93	0.15	1.13	0.05	0.326	0.195
5-19	0.91	0.16	1.12	0.06	0.250	0.185
5-20	1.37	0.21	0.925	0.047	0.269	0.198
5-21	2.04	0.31	1.12	0.06	0.282	0.198
5-22	2.18	0.33	0.945	0.056	0.314	0.202
5-23	1.70	0.26	1.06	0.06	0.432	0.224
5-24	2.61	0.40	1.11	0.06	0.361	0.194
5-25	1.81	0.27	0.598	0.060	0.313	0.183
5-26	(0.78)	0.15	0.647	0.047	0.337	0.187
5-27	4.64	0.70	1.41	0.05	0.411	0.216
5-28	(1.07)	0.19	2.09	0.05	0.383	0.209
5-29	1.59	0.28	2.13	0.06	0.322	0.180
5-30	1.65	0.25	1.77	0.05	0.250	0.154
5-31	1.46	0.25	1.29	0.05	0.221	0.152
5-32	(0.59)	0.34	1.04	0.05	0.243	0.154

(continued on next page)

Table 3.3
(continued)

Observation Number	N_{H_2}	σ_{H_2}	N_{HI}	σ_{HI}	B/B_o	I/I_o
		(10^{21} atoms cm^{-2})				
(1)	(2)	(3)	(4)	(5)	(6)	(7)
6-1	(0.79)	0.17	0.751	0.039	0.189	0.101
6-2	<0.50	0.25	0.890	0.036	0.132	0.104
6-3	0.94	0.15	1.31	0.04	0.187	0.142
6-4	(0.62)	0.21	0.598	0.051	0.191	0.146
6-5	<0.41	0.20	0.146	0.037	0.064	0.054
6-6	<0.61	0.31	0.487	0.036	0.074	0.063
6-7	<0.36	0.18	0.827	0.037	0.085	0.087
6-8	<0.49	0.24	0.661	0.033	0.157	0.124
6-9	<0.35	0.17	0.146	0.029	0.060	0.054
6-10	<0.50	0.25	0.257	0.031	0.056	0.050
6-11	<0.26	0.13	0.501	0.031	0.099	0.075
6-12	<0.41	0.20	0.883	0.033	0.128	0.104
6-13	<0.29	0.15	0.674	0.034	0.060	0.044
6-14	<0.40	0.20	0.765	0.032	0.134	0.084
6-15	<0.26	0.13	0.897	0.040	0.063	0.045
6-16	<0.55	0.28	0.633	0.033	0.080	0.077
6-17	0.64	0.10	0.688	0.035	0.046	0.039

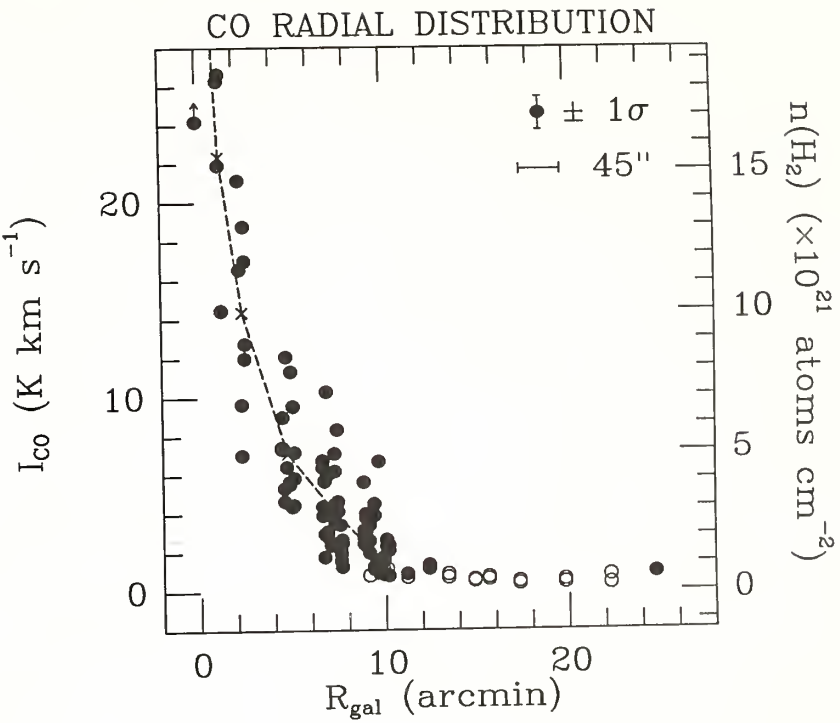

Figure 3.3: The distribution of CO integrated intensity with galactic radius in NGC 6946. The dashed line shows the azimuthally averaged CO distribution, and the ×'s indicate the mean integrated intensity in each annulus. Open circles indicate CO 2σ upper limits. The inferred H_2 surface density scale is shown on the right axis.

was obtained by triangulating the irregularly spaced data and spline fitting at each regularly spaced grid point.

In addition to the strong central peak in the emission obvious in Figure 3.4a, there are smaller peaks to the northeast and southwest of the center, along a position angle of ~40°. All three small peaks lie very close to optical spiral arms. The most interesting of the three peaks is the long CO extension observed to the northeast, which lies in the direction of the largest, high surface brightness spiral arm in the galaxy. The coincidence of CO peaks with blue spiral arms will be discussed in Chapter 4. It is interesting that the CO contours are extended in a direction that is nearly perpendicular to that of the CO bar (P.A. = 160°) detected in the central 45" by Ball *et al.* (1985). There is also a weak extension of the CO contours to the northwest, but no corresponding extension to the southeast of the galactic center.

In Figure 3.4b, we present a contour map of the inner 6'.75 of the 45" resolution HI integrated flux distribution. As previously discussed in Chapter 2 the most obvious difference between the CO and HI maps is the presence of a large HI depression in the central region where the CO integrated intensity is at a maximum. An interesting similarity between the two maps is the general alignment of the position angles of the CO extensions and the HI hole. Finally, we note that although the two CO extensions to the northeast and northwest of the galaxy center lie in the same directions as two bright HI peaks, they are interior to those peaks in both cases.

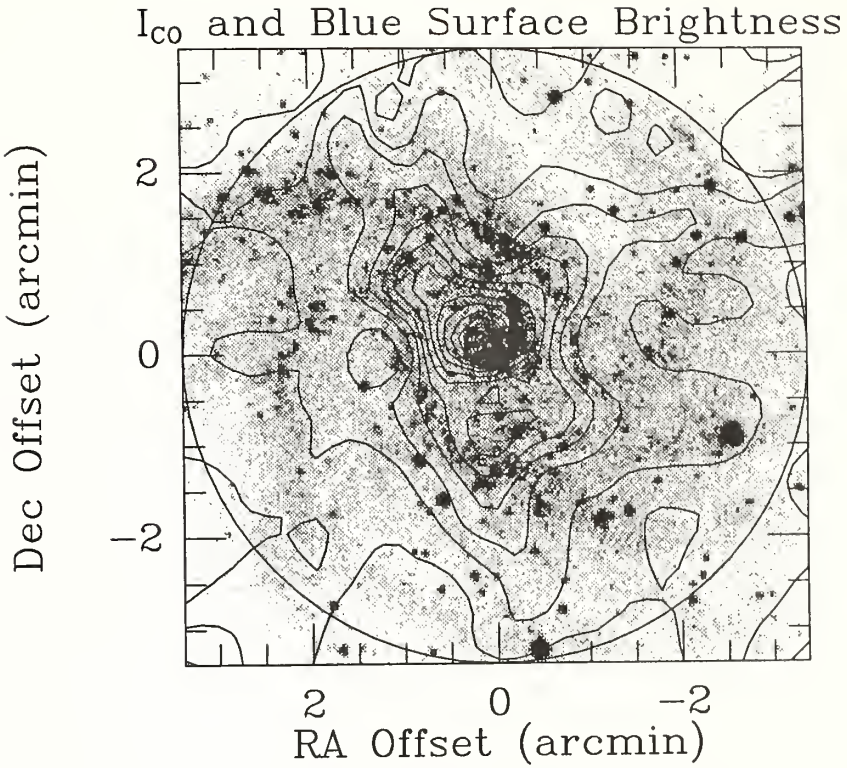

Figure 3.4a: A contour map of the CO integrated intensities observed in NGC 6946 superposed on the blue image (Elmegreen and Elmegreen). Contours range from 2 to 44 K km s^{-1} in intervals of 3 K km s^{-1}. Any features present outside of the circle are artifacts of the interpolation scheme.

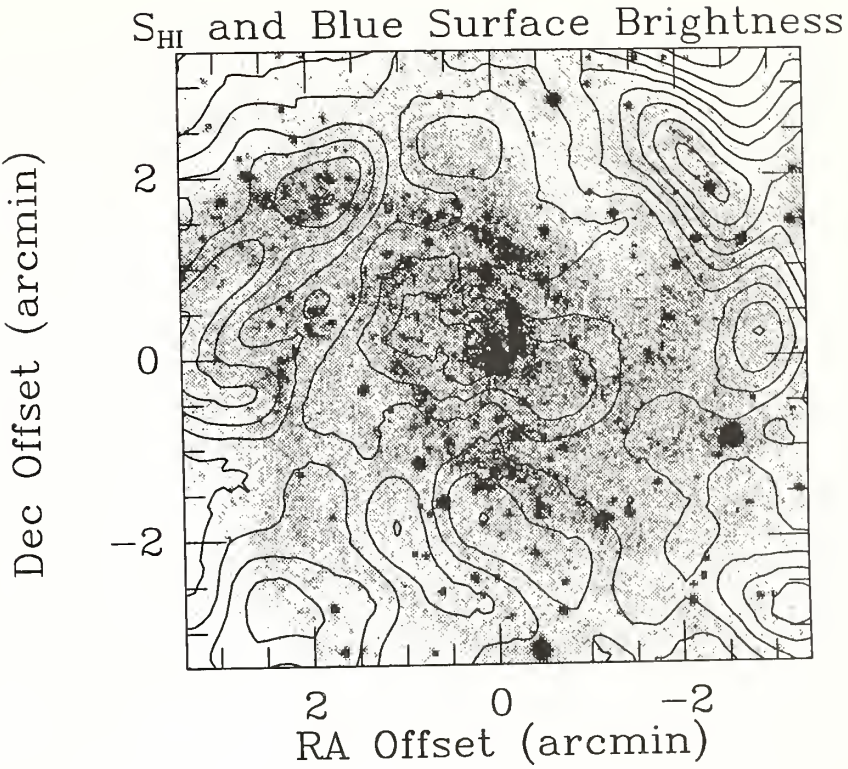

Figure 3.4b: A contour map of the HI distribution in the inner 6'.75 of NGC 6946 superposed on a grayscale of the B-band data (Elmegreen and Elmegreen). The contours are in intervals of 0.3 Jy km s^{-1}, with extremes of 0.3 and 3.3 Jy km s^{-1}.

3.3.2 Gas Surface Densities

We have calculated H_2 and HI surface densities from the CO and HI intensity maps at all 110 CO positions, as shown in Table 3.3. HI surface densities were calculated by the method described in Chapter 2. H_2 surface densities were obtained from the CO integrated intensities using a constant conversion factor (*e.g.* Young and Scoville 1982a; Bloemen *et al.* 1986) of 2.8×10^{20} H_2 $cm^{-2}/K(T_R)$ km s^{-1}. In addition, to convert the CO integrated intensities to H_2 surface densities, the data must be corrected to a T_R scale, to account for the coupling of the main beam to the source. To do this, the I_{CO} values must be divided by η_c, the beam coupling efficiency. The source-beam coupling efficiency is roughly unity for observations of Milky Way molecular clouds taken at FCRAO such that $T_R = T_R^*$. For extragalactic observations, η_c has been found to be about 0.7 (Lord 1987). The central surface density of H_2 corrected to the plane of the galaxy) is 3.4×10^{22} atoms cm^{-2} with values of $<2\times10^{20}$ atoms cm^{-2} in the outer disk of NGC 6946, as compared to the HI densities, which are nearly a factor of 100 lower than H_2 in the center of the galaxy, and peak at radii >6'.

CHAPTER 4

A COMPARISON OF THE MOLECULAR AND ATOMIC COMPONENTS OF THE ISM IN NGC 6946

4.1 Introduction

The process of star formation plays a critical role in the evolutionary history of a galaxy. A major focus in the recent studies of galaxies has been to understand this process through studies of the various components of the interstellar medium. There have been many studies of the CO contents of galaxies in the past several years which have discussed correlations of the CO emission with the blue light, Hα and far-infrared emission in spiral galaxies. These studies have linked the molecular gas with the past and present star formation histories of the galaxies (*e.g.* Young and Scoville 1982a, 1982b; Solomon *et al.* 1983; Rydbeck, Hjalmarsen, and Rydbeck 1985; Tacconi and Young 1986; Kenney 1987; Lord 1987).

The role of the atomic component of the ISM in the star formation picture, as we understand it, is much less clear. The emission at 21 cm may arise in several ways. First, this emission may be from a separate medium which could eventually become molecular clouds (Seiden 1983; Tacconi and Young 1986). It has also been argued that, some of the emission may arise from the outer parts of molecular clouds where the molecules have been dissociated into atoms by the ambient radiation field (Shaya and Federman 1987). With the advent of sensitive aperture synthesis telescopes, it is now possible to determine the distribution of HI in other galaxies on giant molecular

cloud size scales to gain insight into the role which atomic gas plays in the star formation process.

Another area of interest in the study of star formation in galaxies is the possible relationship between spiral density waves and the star and molecular cloud formation efficiencies. It is believed that in our galaxy most of the massive star formation occurs in spiral arms (Georgelin and Georgelin 1976). In the original theory of Lin and Shu (1964) spiral density waves act as a trigger for cloud and star formation. However, recent calculations indicate that the primary effect of density waves may be to organize gas clouds into a global spiral pattern, while the triggering of molecular cloud and star formation may be a secondary effect (*e.g.* Elmegreen 1987 and references therein). These studies suggest that the latter effect should become important in those galaxies with the strongest density waves, such as M51. Observations are urgently needed to test these predictions.

Complete maps of both the molecular and atomic components of the ISM in many different types of galaxies are necessary to begin to address the above issues. Lord (1987) and Lord and Young (1987) have made one of the few detailed studies of the CO contents of a galaxy and have found a high ratio of $\mu(H\alpha)/\sigma_{gas}$ on the spiral arms in the grand design spiral, M51. However, since the data were radially averaged to improve the signal-to-noise ratio, any information about the azimuthal amplitude variations with radius is lost.

Several high resolution interferometric studies of the molecular contents of the central 1 arcminute of several nearby spiral galaxies have also been made (Ball *et al.* 1985; Lo *et al.* 1987 ; Lo *et al.* 1984), however the current sensitivity and the small field of view make the interferometric determination of the total molecular gas distribution of a galaxy quite difficult. CO observations of the disks of galaxies with large single aperture telescopes offer the best alternative since it is possible to obtain moderate resolution (~20") data without a loss of sensitivity. However, the time needed to obtain a fully sampled map over a significant fraction of the optical disk of a galaxy is unrealistically large. Our CO map (see Chapter 3) represents a compromise between resolution and coverage: we have been able to fully sample the inner 6'.75 at 45" resolution. Although higher resolution would be desirable to more accurately determine the spiral arm-interarm contrasts of the molecular gas, our map has the advantage of being able to determine the azimuthal fluctuations over the entire disk of the galaxy.

In this chapter, we make point-to-point comparisons among the molecular, atomic, and ionized components of the ISM in NGC 6946, and also compare the various components of the ISM with B- and I-band images to determine the effects of spiral structure on the gas in this galaxy. Section 4.2 briefly describes the data used in this study; global properties of the gas and optical light distributions are discussed in Section 4.3; the azimuthal variations in the ISM are analyzed and point-to-point

comparisons of the different components are made in Section 4.4; and our results are summarized in Section 4.5.

4.2 The Data

To estimate the star formation efficiencies as a function of position in NGC 6946, we have determined the distribution of the ionized gas by convolving Hα fluxes from the HII region catalogue of Bonnarel, Boulesteix, and Marcelin (1986) with a 45" gaussian beam. This HII region catalogue consists of 643 different HII regions, which were counted from a deep Hα plate taken with the 6-meter Soviet telescope. It should be kept in mind that the HII region catalogue consists of discrete flux regions, and we are therefore missing all of the diffuse Hα emission which is not associated with HII regions. (If the diffuse emission is uniformly distributed, the effect of the missing diffuse emission will be to enhance the spiral arm-interarm contrasts of the Hα emission, since most of the HII regions are found in the spiral arms.) In their study of the diffuse ionized gas in the center of M31, Jacoby, Ford and Ciardullo (1985) find that the diffuse Hα emission in the central has a filamentary structure and also follows the light distribution of the central bulge of this galaxy. They suggest that this Hα emission arises from evolved stars and shock heating rather than from recent star formation. If the diffuse Hα emission from NGC 6946 is also due to evolved stars, then the missing diffuse flux from the Bonnarel *et al.* is not important for the purpose of estimating the star formation efficiencies in this galaxy. To get an estimate of how much diffuse flux is missing, we have compared the uncorrected convolved fluxes

with uncorrected Hα fluxes from DeGioia-Eastwood *et al.* (1984). Their data were sampled with a square aperture which was 40" on a side, so there is some uncertainty in comparing the two sets of fluxes. A second source of uncertainty arises from the fact that the data were not sampled at identical positions. We have chosen to compare only those fluxes whose positional offsets from one another were less than 15". We estimate that typically 30%-40% of the total Hα flux may be missing from the convolved HII region fluxes that we use from the Bonnarel, Boulesteix, and Marcelin catalogue. The Hα fluxes given in the catalogue also have not been corrected for the background continuum light. However, Bonnarel, Boulesteix, and Marcelin estimate that this light would account for less than 10% of the total flux.

We have corrected the given Hα fluxes for extinction both due to our own galaxy and internal to NGC 6946. To correct for the internal extinction we have followed the method of DeGioia-Eastwood *et al.* (1984) and computed one half of the surface densities of HI and H_2 at each position. From a comparison with the Bohlin, Savage, and Drake (1978) empirical relationship between the number of hydrogen atoms and color excess, $\langle N(HI+H_2)\rangle/E(B-V) = 5.8\times10^{21}$ atoms cm^{-2} mag^{-1}, we derive the color excess to the central plane of the galaxy at each position. Then, assuming $A_V/E(B-V) = 3.0$ (Mihalas and Binney 1981), the visual extinction to the central plane is obtained, and is interpolated to get the extinction at 6563 Å.

The CO, HI, B- and I-band data reduction have all been previously discussed in Chapters 2 and 3 and will not be discussed further here. We note that the B-band data

of Elmegreen and Elmegreen used in this study have not been corrected for extinction internal to NGC 6946, as have the Hα fluxes.

4.3 Global Properties of the Gas and Optical Light

In this section we compare the global H_2 and HI surface densities with the Hα, blue, and near infrared surface brightnesses. These comparisons are important because each of the different optical light distributions represents a different epoch in a galaxy's evolution. The Hα flux is known to come predominantly from the HII regions surrounding young, hot stars, thus representing $\tau < 10^7$ years. It has been estimated that 50-70% of the blue light in a late-type galaxy arises from stars which are less than 2×10^9 years old (*e.g.* Searle, Sargent, and Bagnuolo 1973; Schweizer 1976). The near infrared light (I-band) from a galaxy is presumably dominated by a population of old K and M giants (*e.g.* Schweizer 1976; Boroson, Strom and Strom 1983). Therefore, comparisons of the atomic and molecular components with the optical light should lend insight into the galaxy's evolutionary history.

4.3.1 A Comparison of H_2 and HI

In Figure 4.1 the log of the H_2 surface densities is plotted as a function of the log of the HI surface densities in order to determine whether the atomic and molecular gas components are correlated in a global sense in NGC 6946. Figure 4.1 shows little correlation between the H_2 and HI surface densities. This is consistent with the result shown in Figure 2.6 that the azimuthally averaged distribution of H_2 decreases with radius while the HI peaks in the disk. The points are coded according to distance from

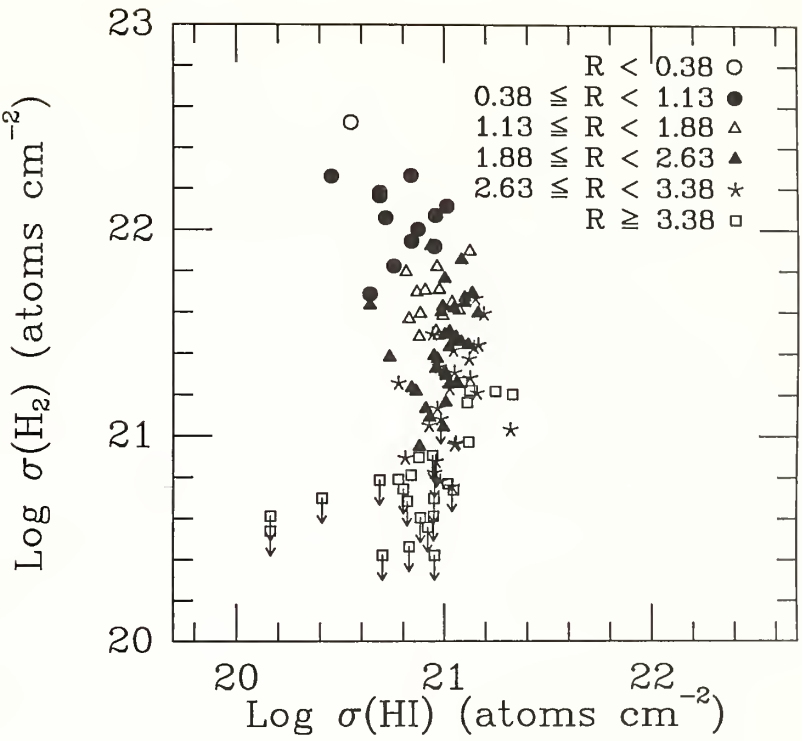

Figure 4.1: The H_2 surface densities as a function of the HI surface densities for all 110 positions in which CO was observed. The data points are coded by their radial distance from the assumed central position. H_2 2σ upper limits are indicated by arrows.

the nucleus in the plane of the galaxy in order to isolate different regions in the radial distributions of H_2 and HI.

The observation that the H_2 and HI densities are not correlated in NGC 6946 is very interesting, since it is believed that H_2 forms from HI on the surfaces of interstellar grains (Hollenbach, Werner, and Salpeter 1971). If molecular clouds do form from atomic clouds then a lack of correlation between the atomic and molecular gas would imply that the molecular clouds are either no longer associated with their parent atomic clouds, or that molecular cloud formation from atomic clouds has been a very efficient process in some regions of NGC 6946. Based on the apparently uncoupled distributions of HI and H_2 in galaxies, Shaya and Federman (1987) have suggested that much of the HI emission in a galaxy may arise from the envelopes of molecular clouds. Since beyond some critical density the atomic gas will become molecular, this leads to HI distributions which are flat as a function of radius, while H_2 increases towards the center. They also suggest that central HI holes in this picture would be regions of enhanced density of H_2. These ideas will be further discussed in Chapter 6.

4.3.2 The Relationship of H_2 and HI with the Optical Light

A lack of a correlation between H_2 and HI surface densities is also evident when comparing each gas component to the optical light. In Figures 4.2-4.4 we have plotted the H_2 and HI surface densities as functions of Hα, B-, and I-band surface brightnesses. Formal least squares linear fits to the data have been made in each case;

Figure 4.2a: The HI surface density plotted against Hα surface brightness for all 110 positions in which CO was observed. The data points are coded by their radial distance from the central position of the galaxy.

Figure 4.2b: The H_2 surface density plotted against Hα surface brightness for the same 110 positions. Each position is coded as in Figure 4.2a. H_2 2σ upper limits are indicated by arrows.

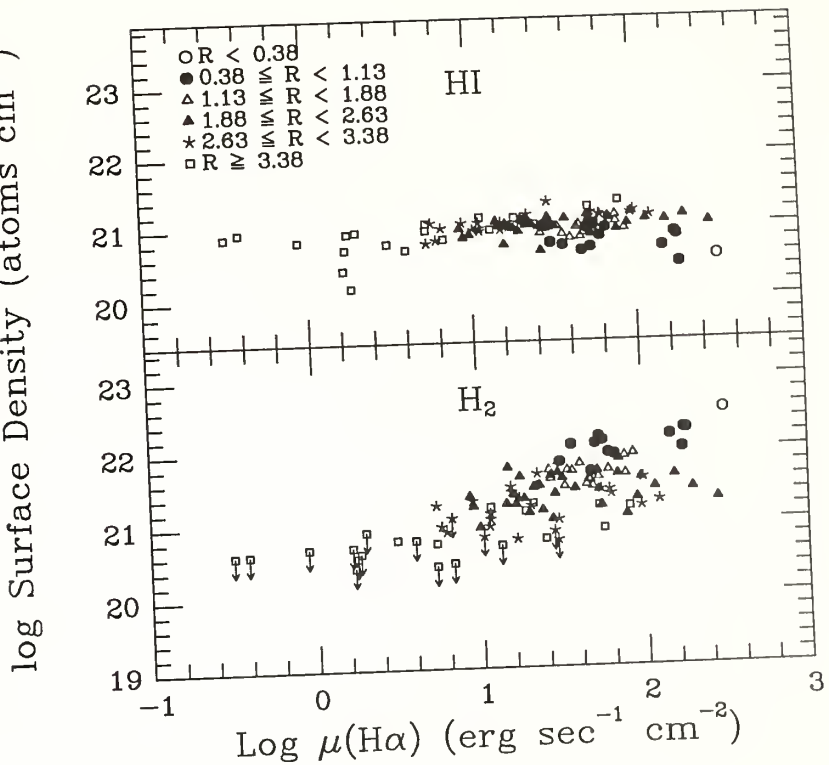
R < 0.38
0.38 ≤ R < 1.13
1.13 ≤ R < 1.88
1.88 ≤ R < 2.63
2.63 ≤ R < 3.38
R ≥ 3.38
HI
H2
log Surface Density (atoms cm-2)
Log μ(Hα) (erg sec-1 cm-2)
23
22
21
20
19
-1
0
1
2
3

Figure 4.3a: The HI surface density plotted against relative blue surface brightness for the 110 positions in which CO was observed. The data points are coded by their radial distance from the central position of the galaxy.

Figure 4.3b: The H_2 surface density plotted against relative blue surface brightness for the same 110 positions. Each position is coded as in Figure 4.3a. H_2 2σ upper limits are indicated by arrows.

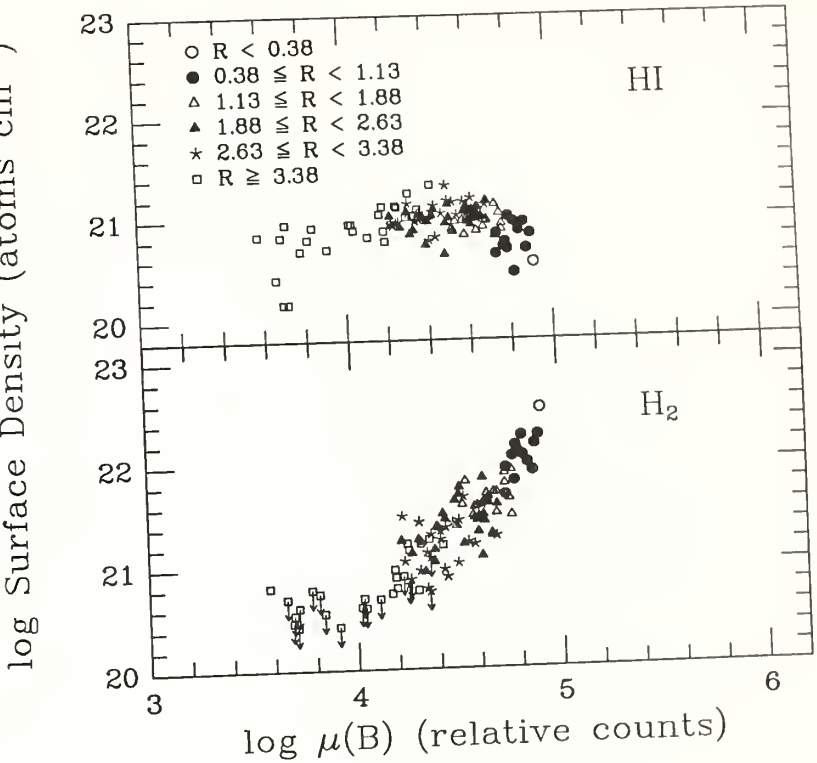
log Surface Density (atoms cm^{-2})
log μ(B) (relative counts)
R < 0.38
0.38 ≦ R < 1.13
1.13 ≦ R < 1.88
1.88 ≦ R < 2.63
2.63 ≦ R < 3.38
R ≧ 3.38
HI
H_2
23
22
21
20
3
4
5
6

Figure 4.4a: The HI surface density plotted against relative I-band surface brightness for all 110 positions in which CO was observed. The data points are coded by their radial distance from the central position of the galaxy.

Figure 4.4b: The H_2 surface density plotted against relative I-band surface brightness for the same 110 positions. Each position is coded as in Figure 4.4a. H_2 2σ upper limits are indicated by arrows.

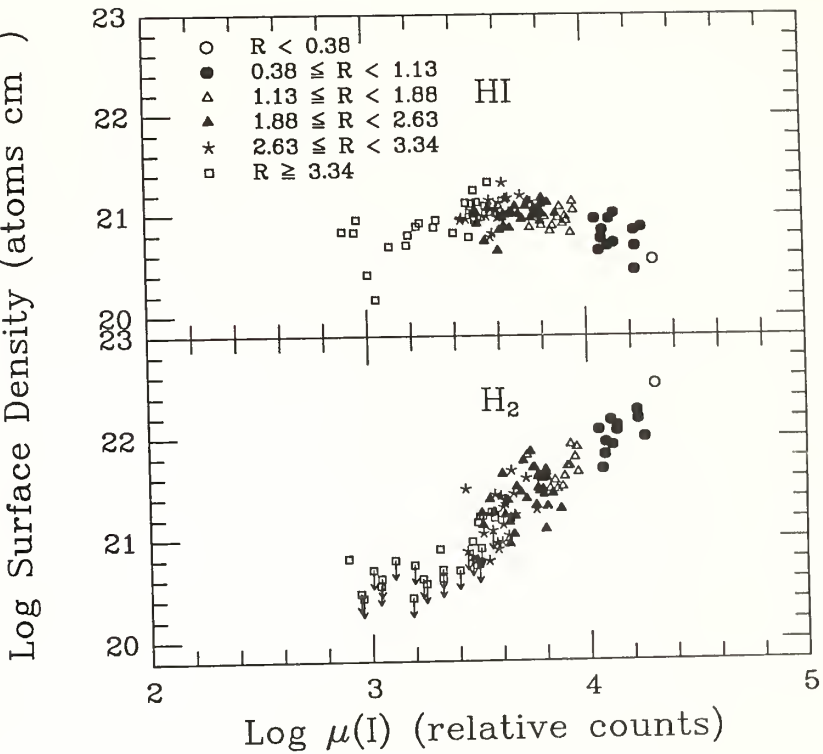
Log Surface Density (atoms cm^{-2})
R < 0.38
0.38 ≦ R < 1.13
1.13 ≦ R < 1.88
1.88 ≦ R < 2.63
2.63 ≦ R < 3.34
R ≧ 3.34
HI
H_2
23
22
21
20
2
3
4
5
Log μ(I) (relative counts)

the results of these fits are given in Table 4.1. The comparison of H_2 with Hα, B-, and I-band fluxes (Figures 4.2b-4.4b) shows a fairly good correlation in all three cases. There is a large amount of scatter in the H_2 vs. Hα plot, which is most easily interpreted as an effect of the short (~10^6 year) lifetimes of HII regions. Many of the HII regions which were once associated with molecular clouds no longer exist, thus all regions with H_2 peaks will not have corresponding peaks in the Hα flux. Another interpretation for the observed scatter in the H_2 vs. Hα relationship is that some HII regions could be heavily obscured by dust, and thus not detectable at Hα, even though the H fluxes have been corrected for internal extinction.

When comparing the HI surface densities with Hα, B-, and I-band surface brightnesses (Figures 4.2a-4.4a) we find that the atomic gas is *not* correlated with any of the optical fluxes. The strikingly different appearances of the HI vs. optical flux and the H_2 vs. optical flux relationships can be thought of in terms of a global galaxy evolutionary picture. Since the flux from the Hα, B-, and I-band each represents a different epoch in the star formation history of a galaxy, the observation that the molecular gas correlates with all three is an indication that the star formation efficiency has remained roughly constant on a scale of 2 kpc over at least the past several billion years. Since the I-band light is dominated by a population of K and M giants, the above time scale may be extended to the lifetime of the galaxy. The result that the HI surface densities are not correlated with the Hα, blue, and near infrared light from NGC 6946 supports our conclusion in Chapter 2 that the atomic gas has not

Table 4.1

Least Squares Fits

X	Y	Slope	r
HI	H_2	-0.778±0.045	-0.335
Hα	H_2	0.391±0.013	0.568
Hα	HI	0.084±0.0027	0.454
B	HI	0.150±0.0081	0.275
B	H_2	1.34±0.032	0.805
I	H_2	1.33±0.030	0.854
I	HI	0.096±0.0091	0.157

played an active role in this galaxy's star formation history. In Chapter 2 we based this conclusion on the differences in the radial distributions of HI and all other components of the galaxy. Here, we are making the comparison over identical 2 kpc regions in the galaxy, and we are led to the same conclusion.

4.3.3 The Efficiency of Star and Molecule Formation

One of the most important quantities to determine in the study of galactic evolution is the star formation efficiency, which we define as the star formation rate per unit gas mass. It is useful to think of the star formation histories of galaxies in terms of star formation efficiencies rather than star formation rates, since the former quantity has been normalized by the available gas supply. Although two galaxies, or two regions within a galaxy, might have similar star formation rates, they could have much different star formation efficiencies, if they also have different amounts of gas. Assuming that stars form from molecular clouds, the massive star formation efficiency, in a qualitative sense, is given by the Hα flux to H_2 surface density ratio; in this section we discuss the star formation efficiency in terms of this ratio.

From azimuthally averaged radial distributions of Hα and the CO radial distribution of Young and Scoville (1982a), DeGioia-Eastwood *et al.* (1984) determined that the azimuthally averaged massive star formation efficiency was constant with radius in NGC 6946. This result can now be tested at each position with our fully sampled CO map and the Hα data of Bonnarel, Boulesteix, and Marcelin (1986). In Figure 4.5, the Hα/H_2 ratios for NGC 6946 are plotted as a function of

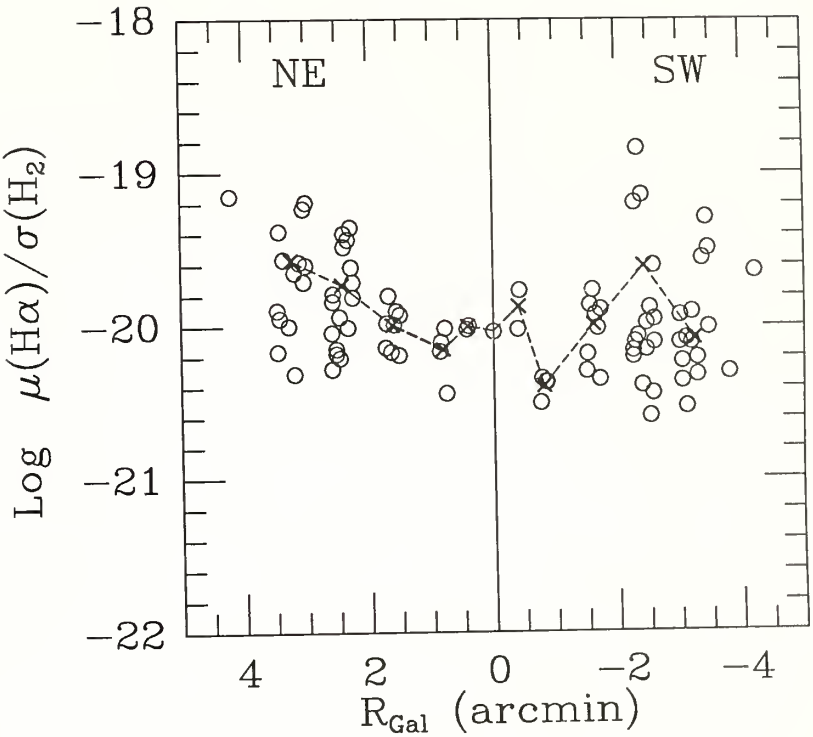

Figure 4.5: The log of the $H\alpha/H_2$ ratios as a function of radius corrected to the plane of the galaxy in NGC 6946 for all 110 CO positions. The galaxy was bisected along the minor axis to search for any asymmetries in the ratio. Positions lying in the eastern half of the galaxy have been assigned positive radial distances, and those in the western half have been assigned negative radial distances as indicated. The ×'s represent the averages in each half ring and have been connected by a dashed line to illustrate the average radial behavior of the $H\alpha/H_2$ ratio.

galactocentric radius. The galaxy has been divided along the kinematic minor axis to show whether any asymmetries are present. The data were also binned in radii, and mean star formation efficiencies were calculated for each bin; these are denoted by ×'s in the Figure. The mean value of $(H\alpha)/(H_2)$ shows peak-to-peak scatter of a factor of 6 about a constant value, while the values of $\mu(H\alpha)$ and (H_2) decrease by a factor of 100 as a function of radius. No trends are evident in Figure 4.5, thus we are led to the same conclusion as DeGioia-Eastwood *et al.* that the massive star formation efficiency is roughly constant as a function of radius in NGC 6946. At a particular radius there is as much as an order of magnitude of scatter about the mean with more scatter and higher peak values in the outer disk; this scatter may be due in part to variations in the star formation efficiency with azimuth, and will be discussed in the next section.

It is also of interest to study the molecule production efficiencies at different locations in a galaxy, and to compare these with the measured star formation efficiencies. Since it is believed that H_2 molecules form from atomic hydrogen on the surfaces of dust grains, one interpretation of the ratio $\sigma(H_2)/\sigma(HI)$ is as a molecule production efficiency. In regions of sufficient optical depth, where the destruction of molecules has been prevented by self-shielding, one expects to have a high H_2/HI ratio relative to a region where H_2 was not able to form from HI, or where a strong UV radiation field has dissociated H_2 into HI. We have plotted the unaveraged H_2/HI ratios as a function of galactocentric radius in Figure 4.6, again bisecting the galaxy along the minor axis. The ×'s and dotted lines indicate the mean in each radius bin.

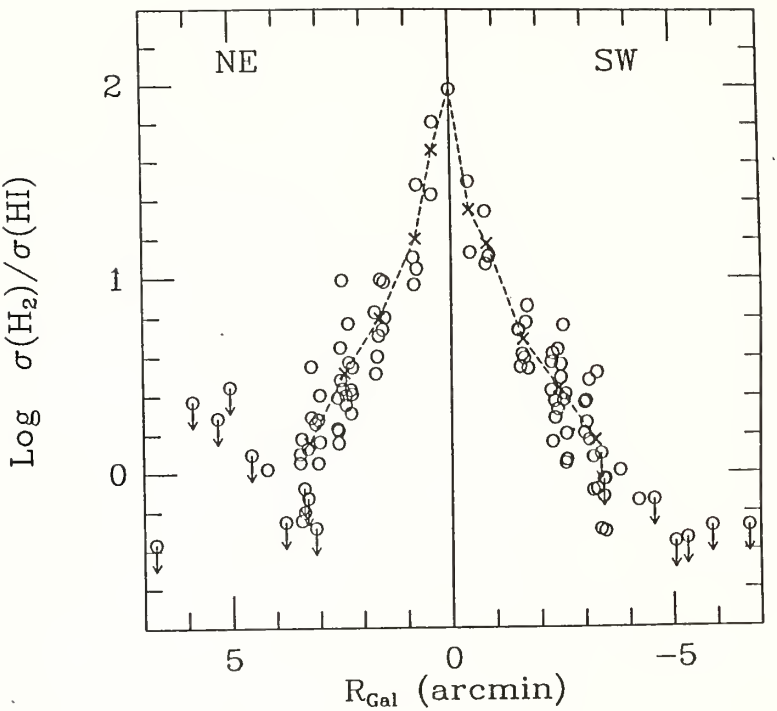

Figure 4.6: The log of the H_2/HI ratios as a function of radius corrected to the plane of the galaxy in NGC 6946 for all 110 CO positions. The galaxy was bisected along the minor axis to search for any asymmetries in the ratio. Positions lying in the eastern half of the galaxy have been assigned positive radial distances, and those in the western half have been assigned negative radial distances as indicated. The ×'s represent the averages in each half ring and have been connected by a dashed line to illustrate the average radial behavior of the H_2/HI ratio. H_2/HI 2σ upper limits are indicated by arrows.

There is a sharp monotonic decrease in the H_2/HI ratio with radius in NGC 6946, with no apparent differences in the radial distribution between the NE and SW halves of the galaxy. The scatter observed about the mean values is due to azimuthal variations in the ratio of H_2/HI surface densities, and like the $\mu(H\alpha)/\sigma(H_2)$ ratio, this scatter is larger in the outer disk.

One interpretation of the radial decrease in the $\sigma(H_2)/\sigma(HI)$ ratio is that there is a decrease in the H_2 production efficiency. Since the ionizing flux (as determined from the $H\alpha$ data) is also decreasing with radius, the decrease in the $\sigma(H_2)/\sigma(HI)$ ratio cannot be attributed to an increase in the dissociation rate of H_2. However, a lower gas volume density in the outer parts of the disk would cause a corresponding drop in the molecular production rate, since this rate is proportional to the first power of the gas volume density (Hollenbach, Werner, and Salpeter 1971).

An alternative interpretation of the $\sigma(H_2)/\sigma(HI)$ ratio is that the HI represents the envelopes of molecular clouds. In this scenario, the HI is largely a by product of H_2 destruction. Shaya and Federman (1987) have reproduced decreasing H_2 distributions and flat HI distributions in galaxies under the assumption that HI is in part a destruction product of H_2. Further discussion of this is found in Chapter 6.

4.4 Azimuthal Variations and Spiral Structure

4.4.1 Optical Spiral Arms

NGC 6946 does not exhibit a simple two armed grand design spiral pattern, but rather a very complicated spiral structure, as can be seen in the grayscale images of the B- and I-band data (Figures 4.7a and b). From the appearance of the B- and I-band images, Elmegreen and Elmegreen (1984) have assigned a spiral arm class of 9 to this galaxy. In their classification scheme a galaxy with an arm class of 6 has flocculent spiral arms, whereas a galaxy with an arm class of 12 exhibits two-armed grand design spiral structure. M51 and M81 are examples of the latter arm class. A spiral arm class 9 galaxy, such as NGC 6946, has a multiple-armed spiral structure with a true underlying stellar density enhancement; that is, the arms are delineated by the older, low mass stars as well as by the HII regions and O and B stars.

There appear to be six separate spiral arms emanating from the central region of NGC 6946. Three of the arms originate in the northeast quadrant of the galaxy, while the other three lie in the southwest. The most striking of the spiral arms is the strongly developed, luminous arm in the NE, in contrast with the poorly defined spiral structure to the SW.

The differences between the eastern and western spiral arms have been quantified by Bonnarel, Boulesteix, and Marcelin (1986). They find that both the largest and brightest HII regions are associated with the eastern spiral arms. Neither the HI nor

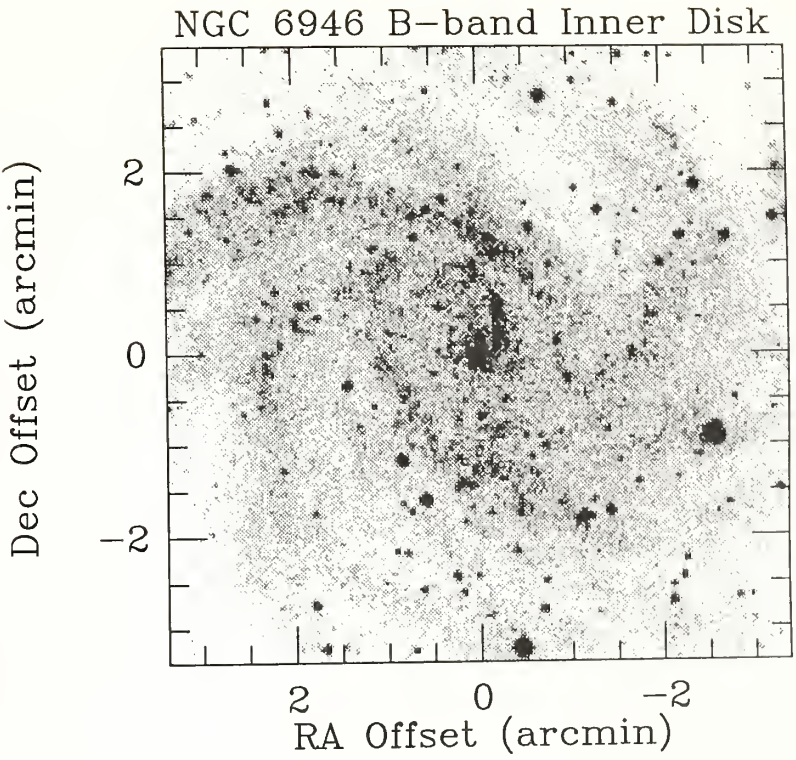

Figure 4.7a: A grayscale representation of the inner 6.75 arcminutes of Elmegreen and Elmegreen's B-band image of NGC 6946.

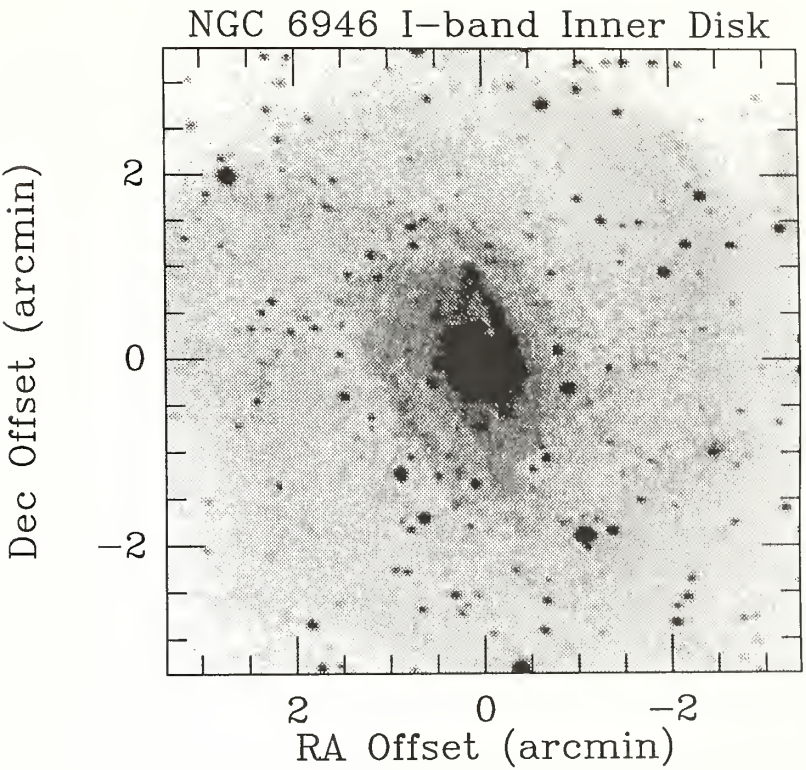

Figure 4.7b: A grayscale representation of the inner 6.75 arcminutes of Elmegreen and Elmegreen's I-band image of NGC 6946.

CO distributions show any striking asymmetry between the east and west portions of the galaxy, however (see Chapter 3). It is possible, then, that the difference between the east and the west spiral arms is due to differences in the HII region properties or perhaps in the massive star formation rates. The contrasting properties of the east and west spiral arms are discussed in detail in the following section.

4.4.2 Observed Azimuthal Fluctuations

A very important part of this study of the detailed distribution of the ISM in NGC 6946 is to determine the azimuthal variations in the gas at several different galactocentric radii and to compare the locations of the gas surface density enhancements with enhancements in the optical flux, and also with the locations of the spiral arms. For each of the four CO annuli at radii of 0'.75, 1'.50, 2'.25, and 3'.00, we have compared the azimuthal distributions of H_2, HI, Hα, B-, and I-band fluxes all at 45" resolution; these distributions are shown in Figures 4.8-4.11 along with the variations in the Hα/H_2, H_2/HI, and Hα/B ratios. At each of the four radii we have defined the spiral arm locations from specified flux levels in the unsmoothed I-band image. The I-band spiral arms are indicated by solid lines at the bottom of each panel in Figures 4.8-4.11.

The spiral structure is not well defined at radii of 0'.75 and 1'.5. At r = 0'.75 nearly all azimuths contain spiral arms by our definition. In these inner regions possible arm-interarm contrasts will not be obvious at 45" resolution. The spiral structure is fairly well defined at radii of 2'.25 and 3'.00, however. At these radii 45" resolution is

Figure 4.8a: The azimuthal variations of the H_2 and HI surface densities, the relative blue surface brightness, and the Hα surface brightness for the 0.75 arcminute annulus. Azimuths are defined from north through east with north at 0°. To more easily see the variations in the north, the azimuths shown here range from -90° to 450° rather than just 0° to 360°. The solid horizontal lines at the bottom of each panel indicate the locations of the I-band spiral arms at this radius. 1σ error bars are indicated on the points where appropriate.

R = 0′.75
σ(H2) (×10^20 atoms cm^-2)
σ(HI) (×10^20 atoms cm^-2)
μ(Hα) (×10^-13 erg s^-1 cm^-2)
Relative Blue Flux
Azimuth (degrees)
0
100
200
300
400
50
100
150
4
6
8
10
200
400
600
1
1.1
1.2
1.3
1.4

Figure 4.8b: The azimuthal variations of the relative I-band surface brightness, and the H_2/HI, Hα/H_2, and Hα/B ratios for the 0.75 arcminute annulus. All features are the same as in Figure 4.8a.

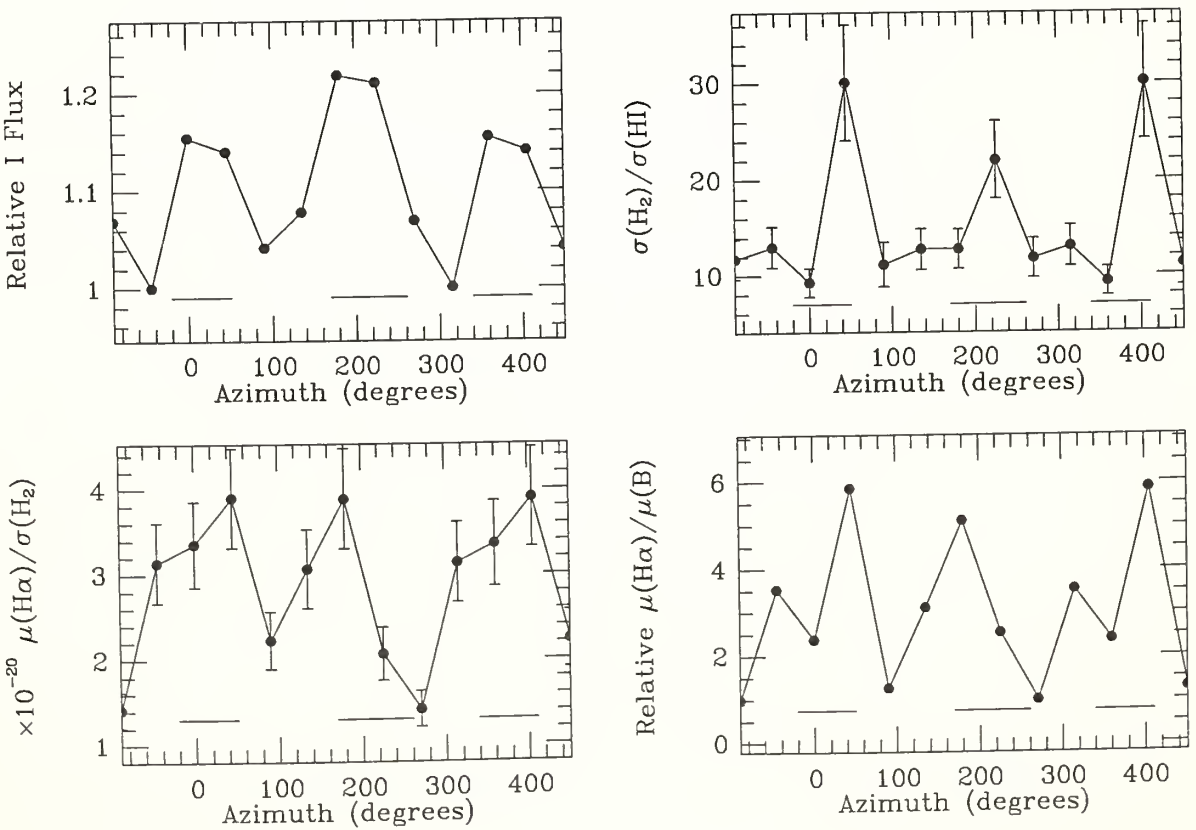
R = 0′.75
Relative I Flux
1.2
1.1
1
0
100
200
300
400
Azimuth (degrees)
σ(H₂)/σ(HI)
30
20
10
0
100
200
300
400
Azimuth (degrees)
×10⁻²⁰ μ(Hα)/σ(H₂)
4
3
2
1
0
100
200
300
400
Azimuth (degrees)
Relative μ(Hα)/μ(B)
6
4
2
0
0
100
200
300
400
Azimuth (degrees)

Figure 4.9a: The azimuthal variations of the H_2 and HI surface densities, the relative blue surface brightness, and the Hα surface brightness for the 1.50 arcminute annulus. Azimuths are defined from north through east with north at 0°. To more easily see the variations in the north, the azimuths shown here range from -90° to 450° rather than just 0° to 360°. The solid horizontal lines at the bottom of each panel indicate the locations of the I-band spiral arms at this radius. 1σ error bars are indicated on the points where appropriate.

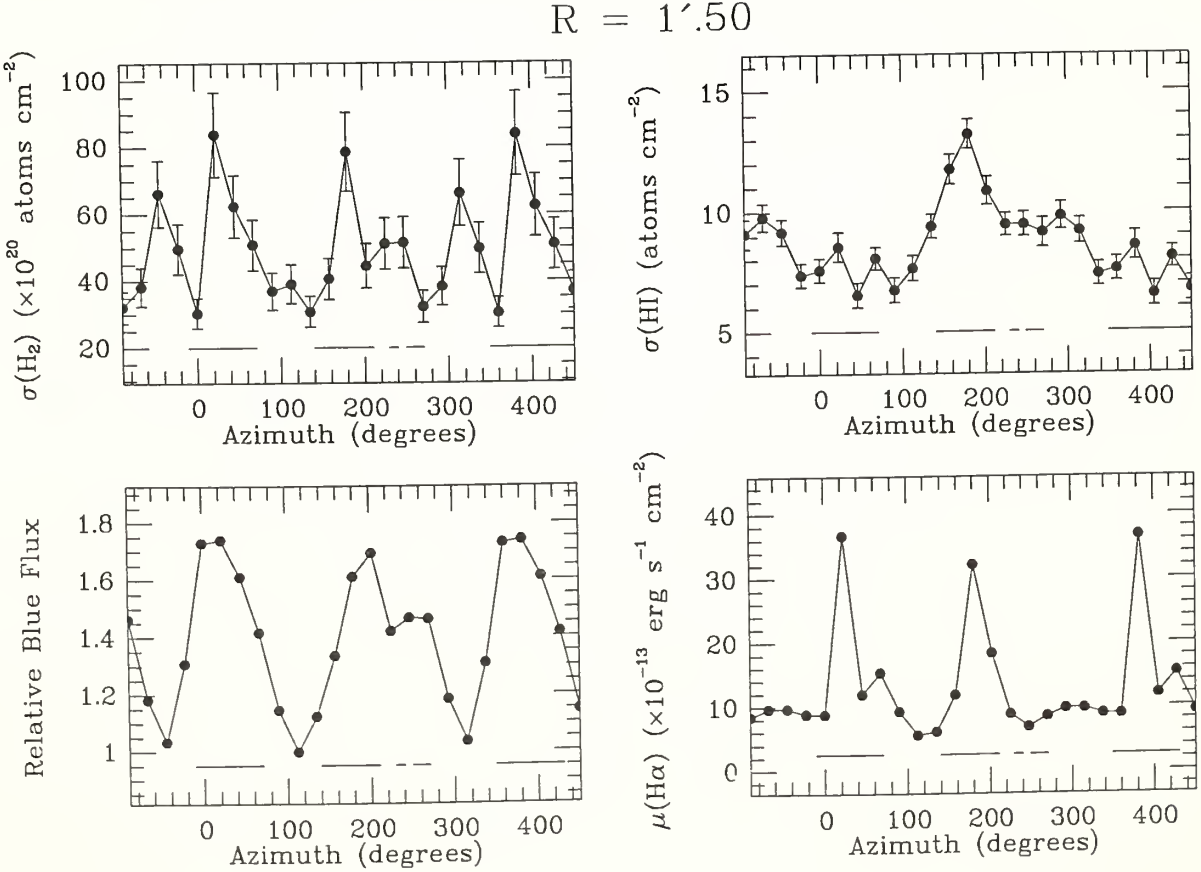
R = 1′.50
σ(H2) (×10^20 atoms cm^-2)
σ(HI) (atoms cm^-2)
Relative Blue Flux
μ(Hα) (×10^-13 erg s^-1 cm^-2)
Azimuth (degrees)
Azimuth (degrees)
Azimuth (degrees)
Azimuth (degrees)

Figure 4.9b: The azimuthal variations of the relative I-band surface brightness, and the H_2/HI, Hα/H_2, and Hα/B ratios for the 1.50 arcminute annulus. All features are the same as in Figure 4.9a.

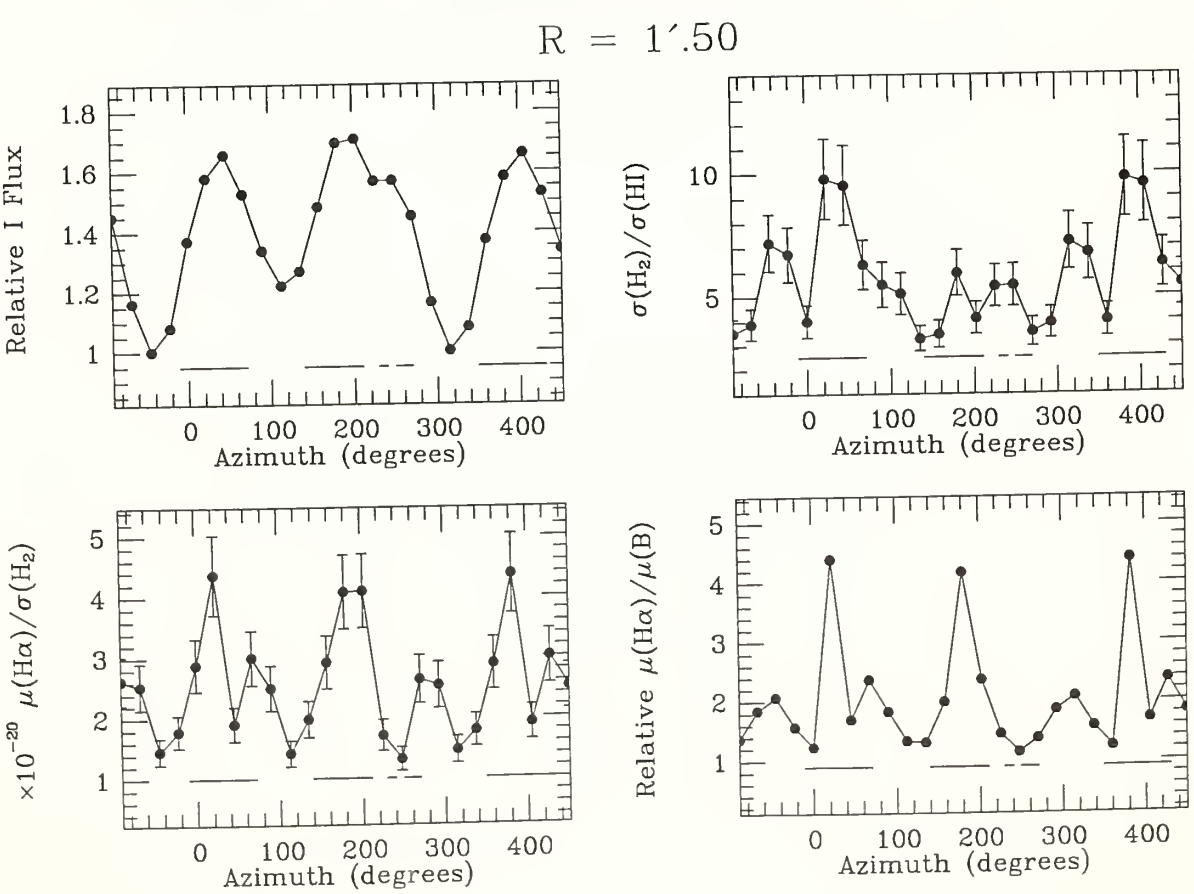
R = 1′.50
Relative I Flux
1.8
1.6
1.4
1.2
1
0
100
200
300
400
Azimuth (degrees)
σ(H2)/σ(HI)
10
5
0
100
200
300
400
Azimuth (degrees)
×10^-20 μ(Hα)/σ(H2)
5
4
3
2
1
0
100
200
300
400
Azimuth (degrees)
Relative μ(Hα)/μ(B)
5
4
3
2
1
0
100
200
300
400
Azimuth (degrees)

Figure 4.10a: The azimuthal variations of the H_2 and HI surface densities, the relative blue surface brightness, and the Hα surface brightness for the 2.25 arcminute annulus. Azimuths are defined from north through east with north at 0°. To more easily see the variations in the north, the azimuths shown here range from -90° to 450° rather than just 0° to 360°. The solid horizontal lines at the bottom of each panel indicate the locations of the I-band spiral arms at this radius. 1σ error bars are indicated on the points where appropriate.

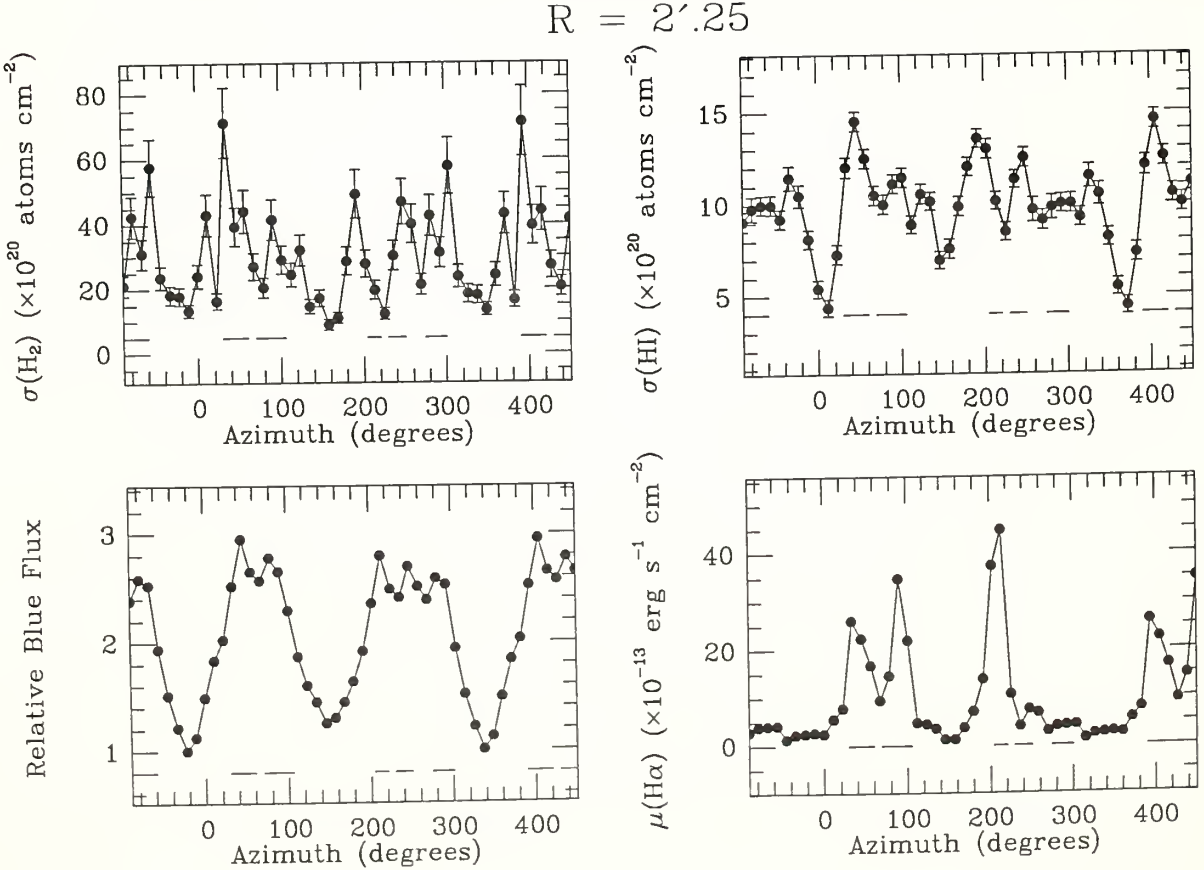
R = 2'.25
σ(H2) (×10^20 atoms cm^-2)
σ(HI) (×10^20 atoms cm^-2)
Relative Blue Flux
μ(Hα) (×10^-13 erg s^-1 cm^-2)
Azimuth (degrees)
0
100
200
300
400

Figure 4.10b: The azimuthal variations of the relative I-band surface brightness, and the H_2/HI, Hα/H_2, and Hα/B ratios for the 2.25 arcminute annulus. All features are the same as in Figure 4.10a.

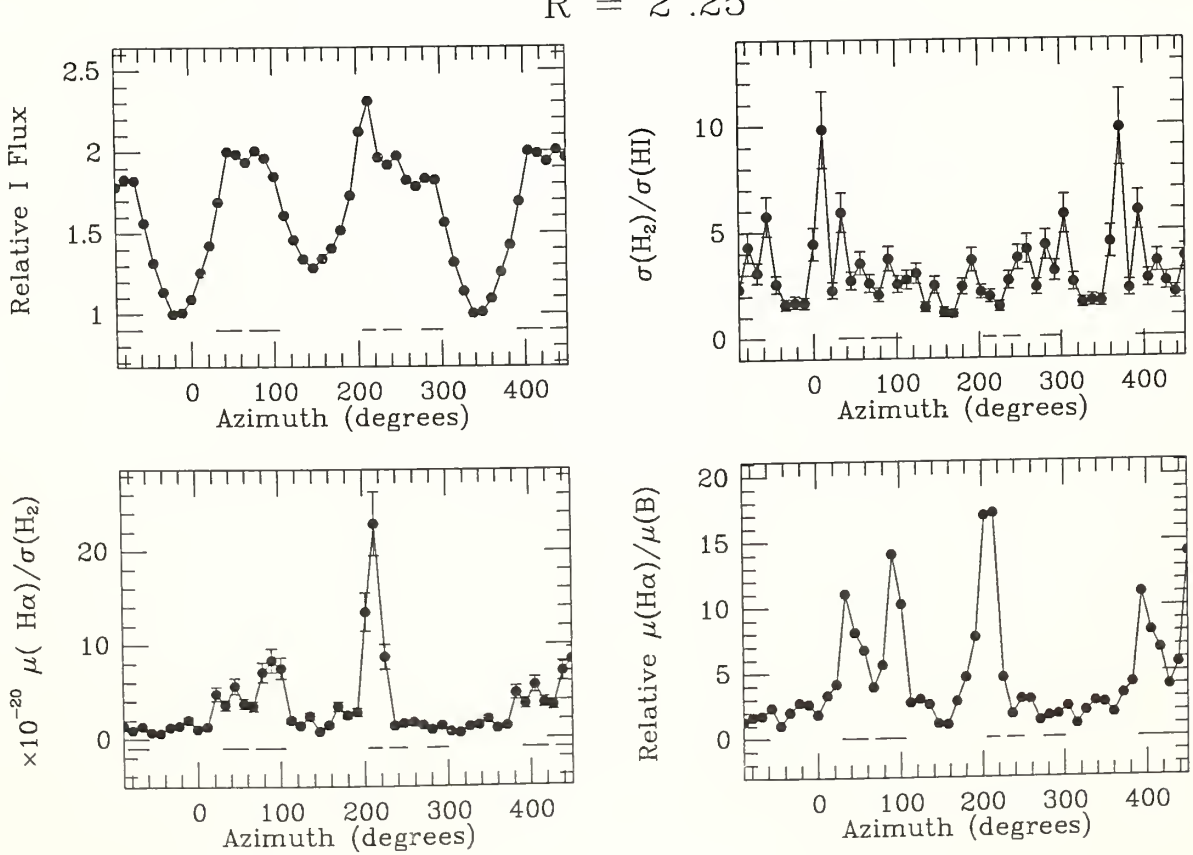
R = 2′.25
Relative I Flux
2.5
2
1.5
1
0
100
200
300
400
Azimuth (degrees)
σ(H2)/σ(HI)
10
5
0
0
100
200
300
400
Azimuth (degrees)
×10−20 μ(Hα)/σ(H2)
20
10
0
0
100
200
300
400
Azimuth (degrees)
Relative μ(Hα)/μ(B)
20
15
10
5
0
0
100
200
300
400
Azimuth (degrees)

Figure 4.11a: The azimuthal variations of the H_2 and HI surface densities, the relative blue surface brightness, and the Hα surface brightness for the 3.00 arcminute annulus. Azimuths are defined from north through east with north at 0°. To more easily see the variations in the north, the azimuths shown here range from -90° to 450° rather than just 0° to 360°. The solid horizontal lines at the bottom of each panel indicate the locations of the I-band spiral arms at this radius. 1σ error bars are indicated on the points where appropriate. Positions with H_2 2σ upper limits are coded with open circles.

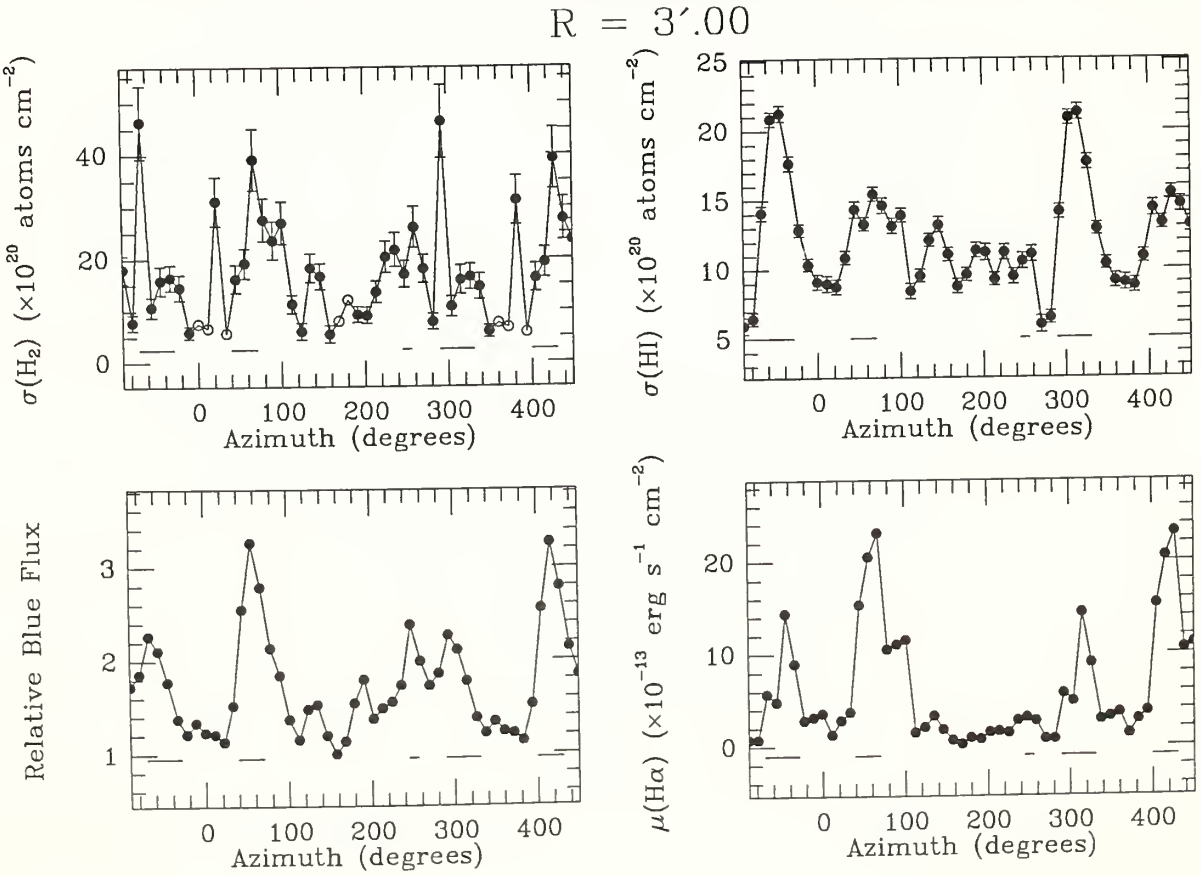
R = 3′.00
σ(H₂) (×10²⁰ atoms cm⁻²)
σ(HI) (×10²⁰ atoms cm⁻²)
Relative Blue Flux
μ(Hα) (×10⁻¹³ erg s⁻¹ cm⁻²)
Azimuth (degrees)
0
100
200
300
400
0
20
40
5
10
15
20
25
1
2
3

Figure 4.11b: The azimuthal variations of the relative I-band surface brightness, and the H_2/HI, Hα/H_2, and Hα/B ratios for the 3.00 arcminute annulus. All features are the same as in Figure 4.11a.

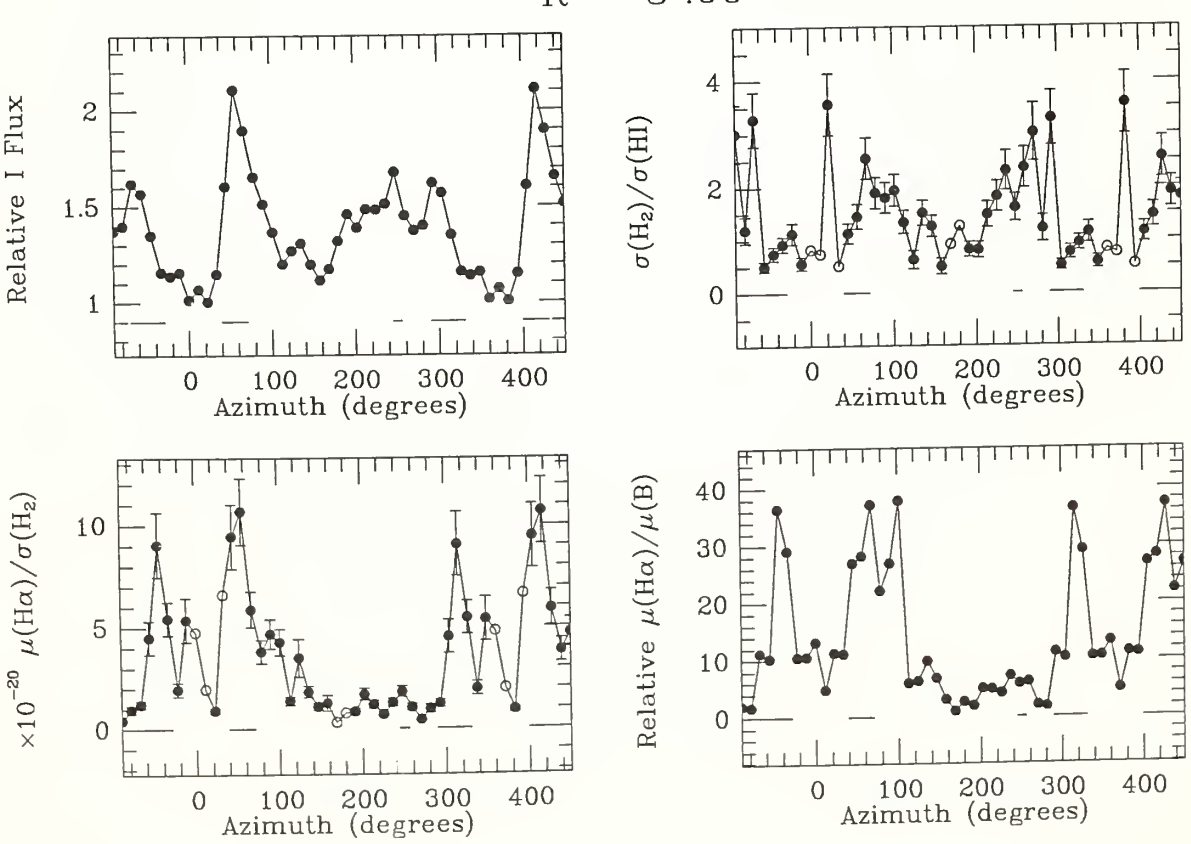
R = 3′.00
Relative I Flux
Azimuth (degrees)
σ(H2)/σ(HI)
Azimuth (degrees)
×10^-20 μ(Hα)/σ(H2)
Azimuth (degrees)
Relative μ(Hα)/μ(B)
Azimuth (degrees)

sufficient to discern several of the spiral arms. Analysis of the azimuthal fluctuations of the ISM at these radii is therefore particularly important to determine the effects of the spiral arms on the gas in NGC 6946. We will now discuss the azimuthal fluctuations of the stars and gas in NGC 6946 at each of the 4 radii.

4.4.2.1 R = 0.'75

At a radius of 0.'75, a fairly good correlation exists between the I-band spiral arms and peaks in the H_2, HI, Hα, and blue emission (see Figure 4.8a). The I-band arms appear quite broad in this figure because at this radius the spiral arms appear to blend together into two distinct regions. The arm-interarm contrasts are greatest for the Hα emission, with a ratio of nearly 4:1, compared to less than 2:1 for all the other components. This difference can be understood, since massive star formation occurs predominantly on spiral arms (Georgelin and Georgelin 1976), and one does not expect to see O and B stars between spiral arms given their short main sequence lifetimes. The older stars, which presumably contribute largely to the B- and I-band light, are found both on and off spiral arms; thus the arm-interarm contrasts are smaller at these wavelengths.

The azimuthal variations in the Hα/H_2, Hα/B, and H_2/HI ratios are also shown for the 0.75 arcminute annulus in Figure 4.8b. The Hα/H_2 ratio measures the massive star formation efficiency and the H_2/HI ratio may be a measure of the molecule production efficiency as previously discussed. The ratio of Hα/B is a measure of the recent star formation rate relative to the past 10^9 years since the Hα emission arises from the

ionization regions surrounding young, massive stars, while the blue light arises largely from stars from stars < 2×10^9 years old (Searle, Sargent, and Bagnuolo 1973). Both the Hα/H_2 and Hα/B enhancements are coincident at the locations of the I-band arms, implying that at this radius the massive star formation efficiency is higher on the spiral arms than in the interarm regions. A coincidence of the high H_2/HI ratios and the optical spiral arms is much less apparent. While it is true that the peaks in the H_2/HI ratio do lie on the I-band arms, the dips in this ratio also seem to coincide with the arms. Given the confusion in determining the locations of the spiral arms at this radius, and the resolution of the data, we make no attempt to interpret this result here. The relationship between the H_2/HI ratios and the optical spiral arms will be more easily determined for the outer annuli in NGC 6946.

4.4.2.2 R = 1.'50

The I- band spiral arms are somewhat better defined in the 1.'50 annulus. However, as can be seen in Figures 4.9a and 4.9b, the relationship between the H_2, HI, and Hα azimuthal distributions and the optical spiral arms is somewhat complicated. In the northeast, peaks in the H_2 and Hα are correlated with spiral arm locations, but no HI peaks are evident in these regions. The I-band arms in the northeast appear as one continuous feature in these figures since there is overlap in azimuth in all three arms. Between 140° and 210° in azimuth, there is an obvious correlation between H_2, HI, and Hα enhancements and a well defined B- and I-band spiral arm. At azimuths of 230° and 260°, there are two less obvious optical spiral arms. While there is a

small H_2 enhancement towards these regions, there is no corresponding enhancement in the Hα or HI emission. These spiral arms do not appear to have any obvious current star formation associated with them.

The differences in the northeast, south, and southwest spiral arms are even more evident in the comparisons of the Hα/H_2, Hα/B, and H_2/HI ratios with the I-band arms. While there are peaks in the Hα/H_2, Hα/B, and H_2/HI ratios toward both the northeast and south arm regions indicating a high efficiency of massive star formation and molecule production on these arms, the Hα/H_2 Hα/B ratios actually have their *lowest* values on the southwest arms. It appears that the presence of spiral arms does not guarantee a high massive star formation efficiency in NGC 6946.

4.4.2.3 R = 2.'25

Of all four annuli that we are considering, the annulus at 2'.25 has the most well defined optical spiral structure. As was found for the 1'.5 ring, the northeast and south spiral arms are regions of H_2 surface density and Hα flux enhancements, while there is a dearth of Hα emission along the southwest I-band spiral arms (see Figures 4.10a and 4.10b); there are peaks in the H_2 density associated with these arms, however. The HI emission is not well correlated with any of the optical spiral arms at this radius.

In complete analogy with the 1'.5 ring, high massive star formation efficiencies are observed along the northeastern and southern spiral arms, but *low* star formation efficiencies are found on the western I-band arms. The variations in the H_2/HI ratios are very interesting at this radius. While there are enhancements in this ratio on the I-

band arms, there are also peaks in the H_2/HI ratio that are not associated with any optical spiral arms. In particular, the strongest peak in the H_2/HI ratio is located at roughly 0° azimuth, in the direction of a large HI hole; the origin of this depletion of the atomic gas is unknown, but it is not associated with any obvious optical features.

4.4.2.4 R = 3.'00

In the outermost annulus (at R = 3.'00), several of the I-band spiral arms are no longer prominent, and only three obvious features remain: the bright northeast arm at azimuth between 40° and 80°, and two of the southwest arms, which are located at 240° to 260° and 290° to 330° in azimuth, respectively. Once again, all of the components of NGC 6946 are well correlated with the I-band spiral arm in the northeast, and less well correlated with the faint arm in the southwest. There is also a fairly good agreement between the H_2, HI, and Hα enhancements and the I-band arm which extends to the northwest. As might be expected, the two arms which have H_2 and Hα enhancements also have a high massive star formation efficiency relative to the interarm regions.

At this point in the discussion, it is useful to summarize trends in the azimuthal structure of NGC 6946 which are evident in all four annuli. At all radii, the optical spiral structure is well defined in the northeastern part of the galaxy. Enhancements in H_2 surface densities and Hα fluxes are found to be associated with the spiral arms in this part of the galaxy. Accordingly, there are increases in the efficiencies of star formation and molecule production on these spiral arms. In contrast, the western half

of the galaxy has very poorly defined spiral structure. While these arms often exhibit H_2 surface density enhancements, these are often not followed by corresponding enhancements in either the Hα fluxes or massive star formation efficiencies. Typical spiral arm-interarm variations in the stars and gas are between factors of 2 and 20. The arm-interarm variations are discussed further in the next section.

4.4.3 Azimuthal Variations as a Function of Radius

In order to estimate the effect of the spiral arm strength on the H_2 and HI surface densities, the Hα surface brightnesses, and the various ratios discussed in section 4.4.2, we have compared the azimuthal profiles of these quantities with the B- and I-band fluxes at each radius in Figures 4.12 - 4.19. In Figures 4.12-4.19 each of the four panels share a common linear y-range. Thus these figures reflect the radial distributions of each quantity as well as the arm-interarm contrasts at each radius. Since the spiral arm-interarm resolution increases with radius(see Section 4.4.2), it is possible that the observed radial variations in the arm-interarm contrasts that are discussed below could be attributed partly to the changing resolution. The B- and I-band azimuthal distributions show prominent spiral arms in the outer disk. From the smoothed I-band azimuthal profiles, we have measured spiral arm and interarm azimuth ranges for the two easily discernible spiral spiral arm complexes in Figure 4.12. The obvious complex in the northeast is hereafter referred to as "arm 1" in this discussion, and the southwest complex as "arm 2". For each quantity we have adopted the peak values over each of the two defined I-band arm azimuth ranges as the "arm"

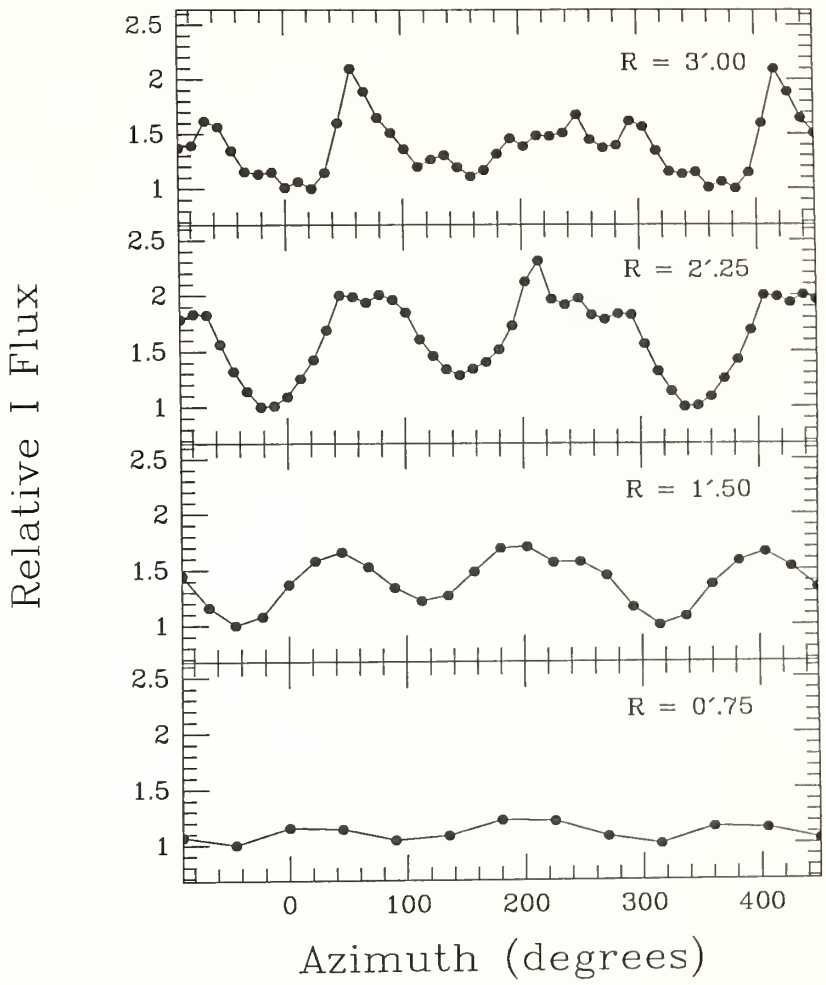

Figure 4.12: The azimuthal variations in the relative I-band surface brightnesses as a function of radius.

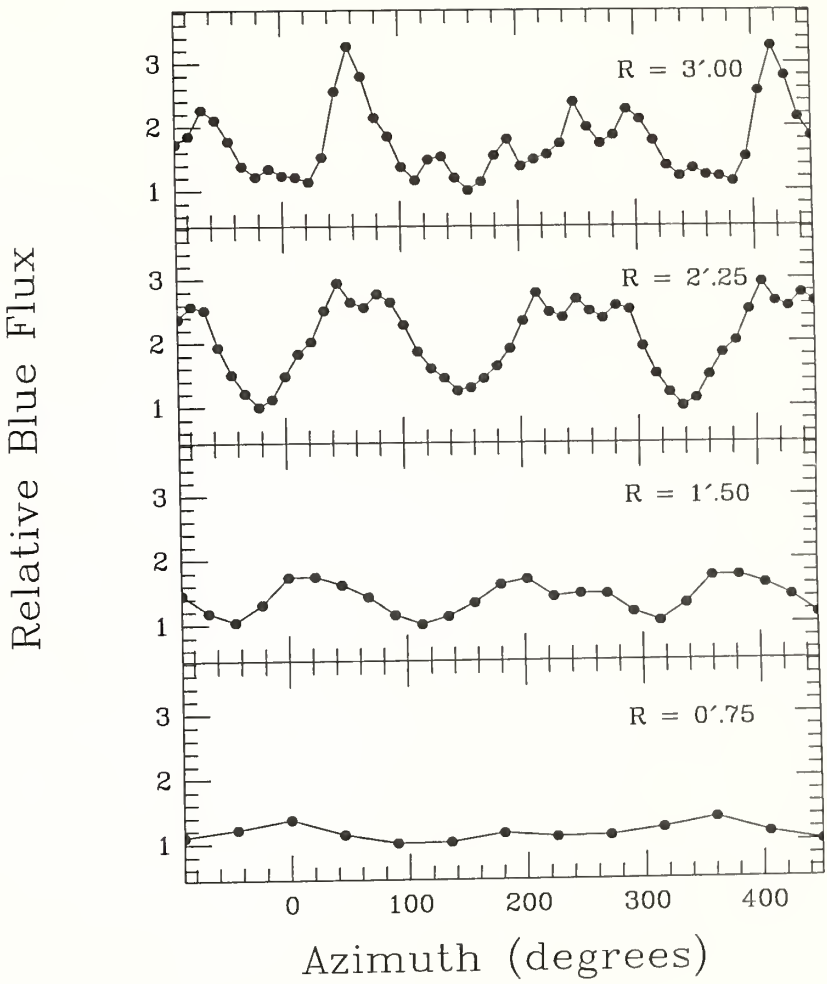

Figure 4.13: The azimuthal variations in the relative B-band surface brightnesses as a function of radius.

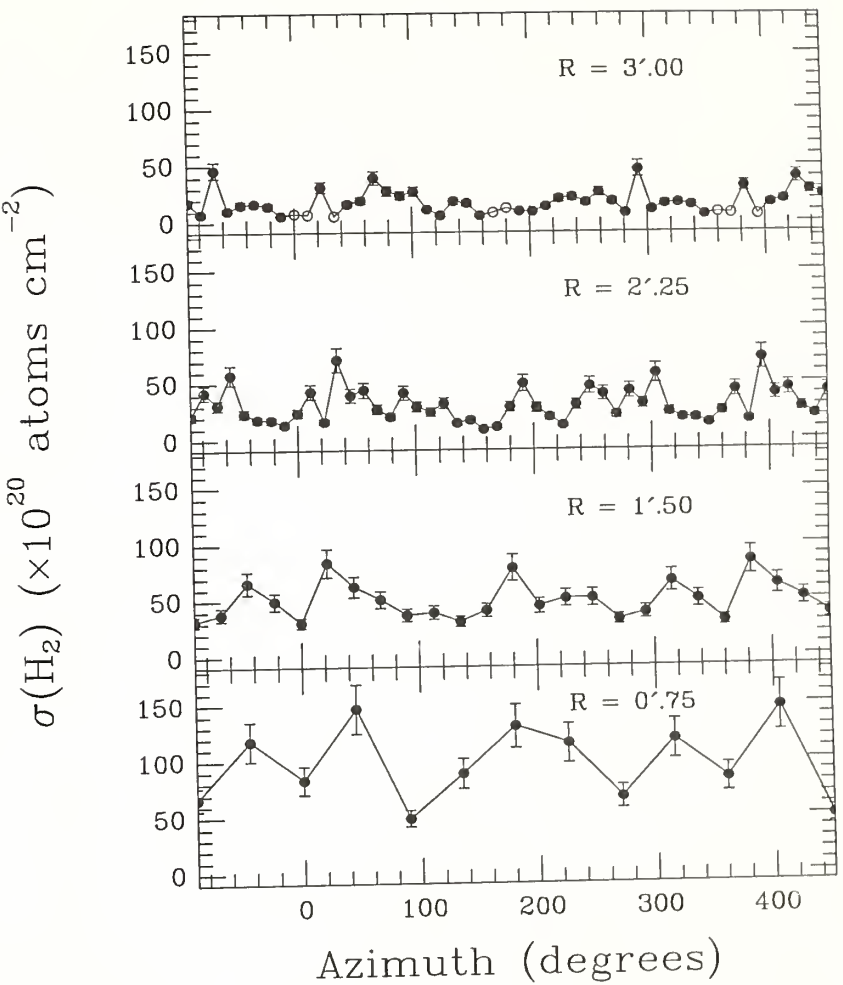

Figure 4.14: The azimuthal variations in the H_2 surface densities as a function of radius. Open circles indicate H_2 upper limits.

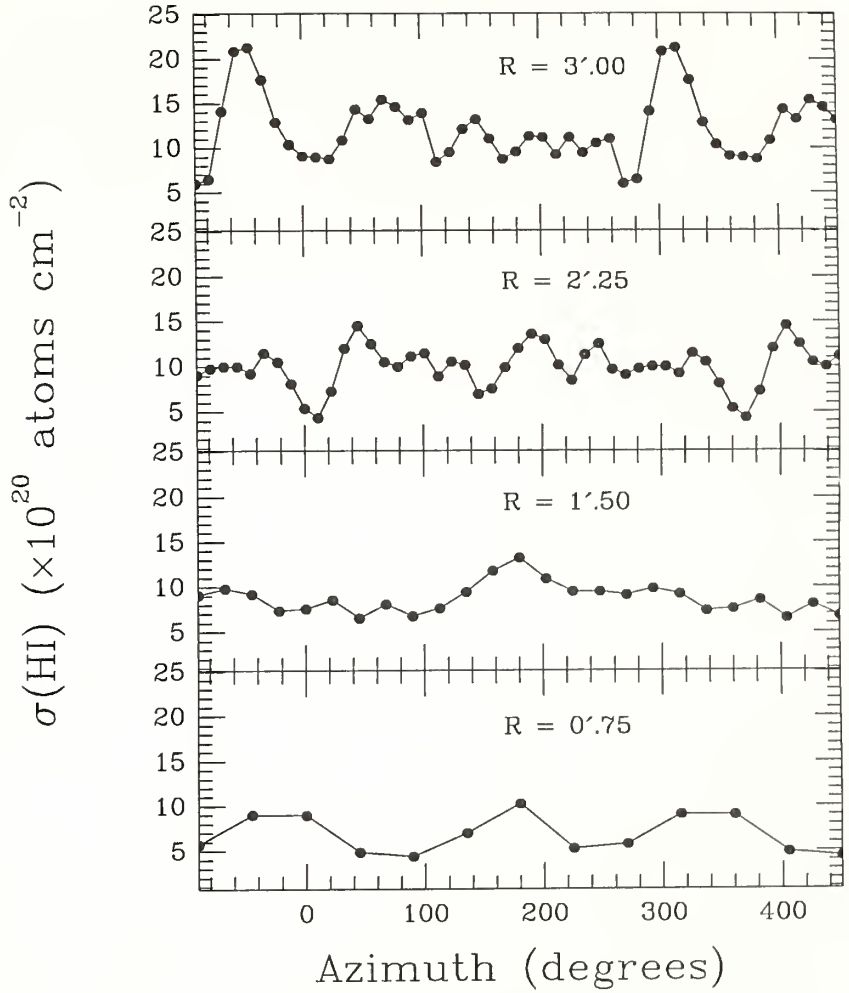

Figure 4.15: The azimuthal variations in the HI surface densities as a function of radius.

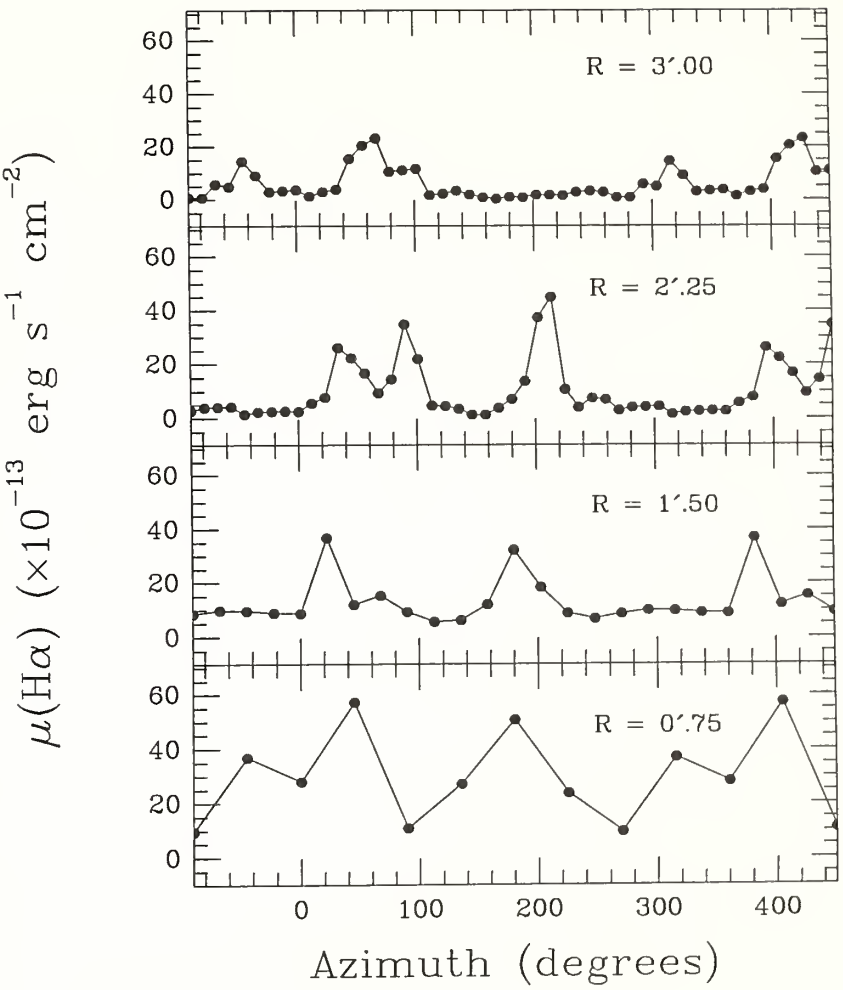

Figure 4.16: The azimuthal variations in the Hα surface brightnesses as a function of radius.

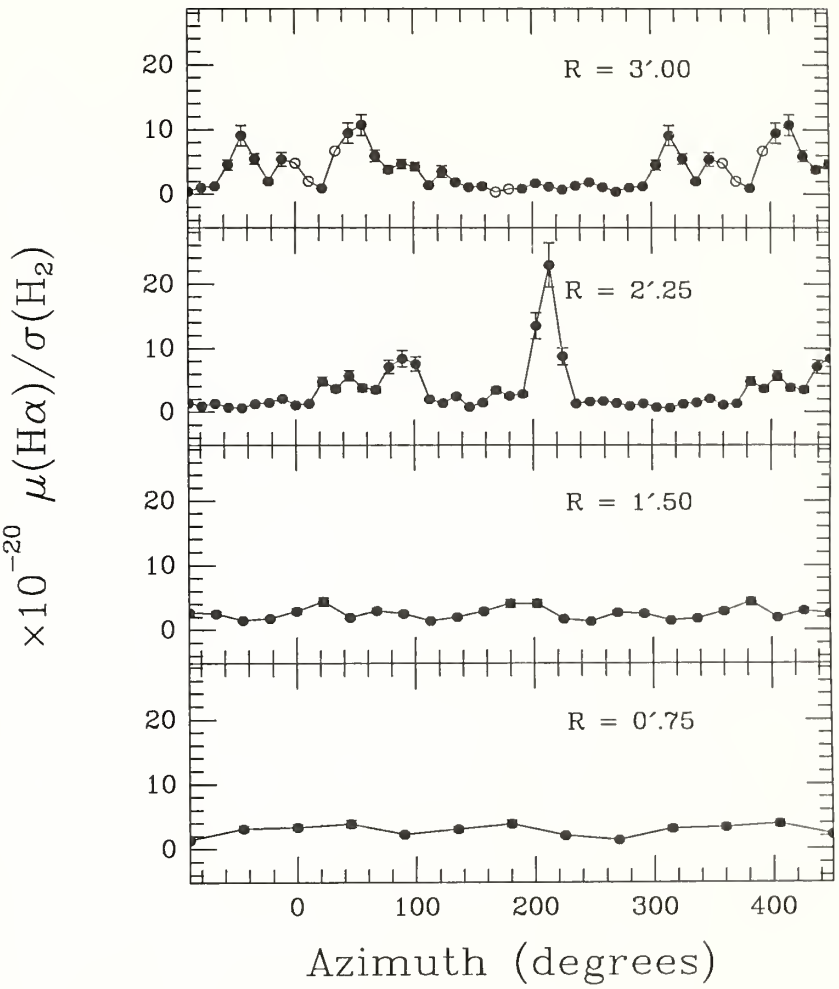

Figure 4.17: The azimuthal variations in the $\mu(H\alpha)/\sigma(H_2)$ ratios as a function of radius. Open circles indicate H_2 upper limits, and therefore lower limits in the $\mu(H\alpha)/\sigma(H_2)$ ratio.

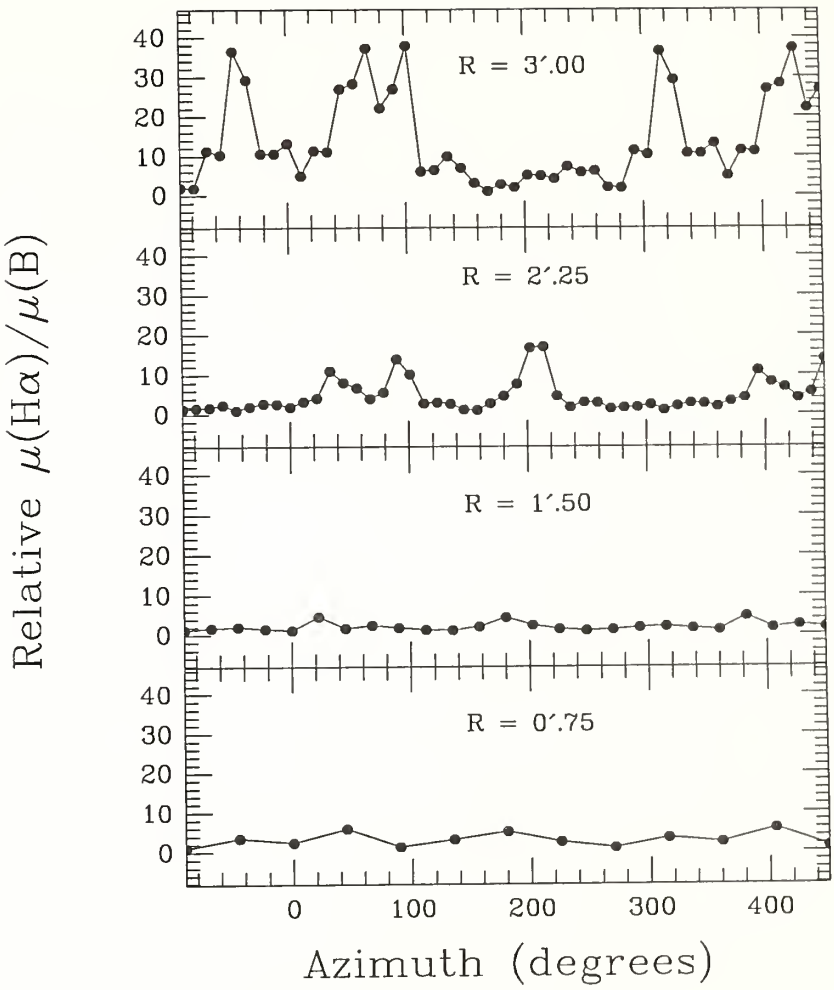

Figure 4.18: The azimuthal variations in the μ(Hα)/μ(B) ratios as a function of radius.

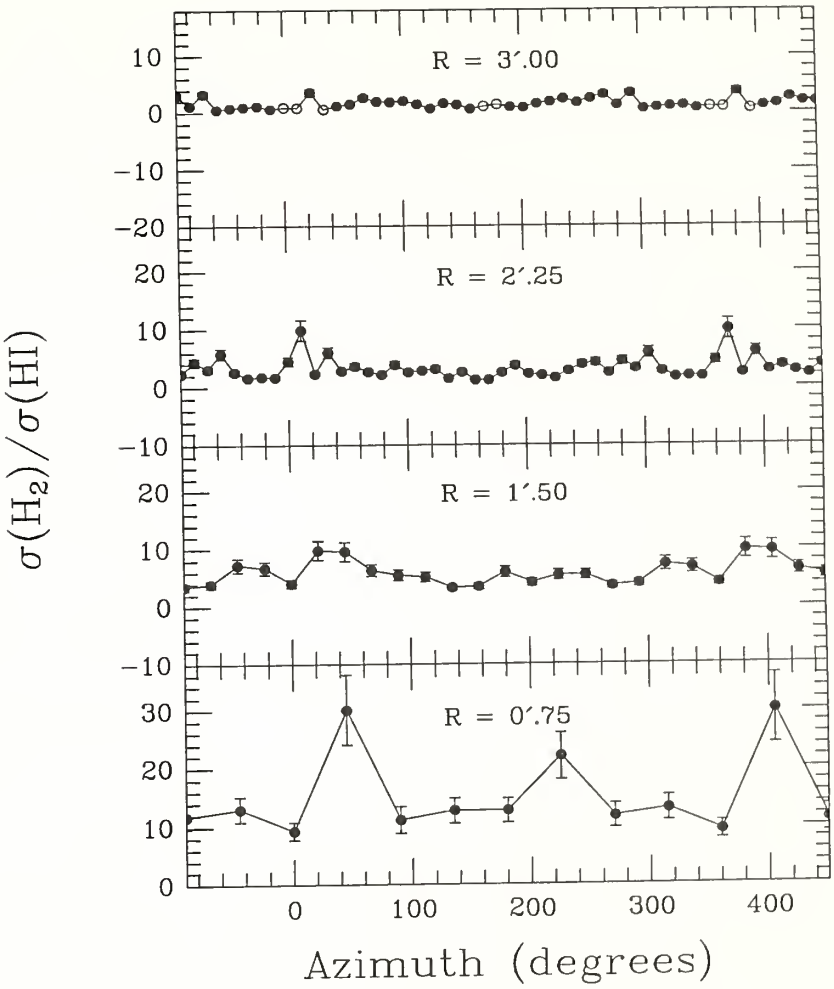

Figure 4.19: The azimuthal variations in the $\sigma(H_2)/\sigma(HI)$ ratios as a function of radius. Although the plotted range of the ratios is the same for each radius, it was necessary to slide the scales of the outer radii to avoid points crowding together. Open circles indicate H_2 upper limits.

values. Similarly, we have adopted an "interarm" value for each quantity as the average over both I-band interarm azimuth ranges. We define the arm-interarm contrast as simply the ratio of these two quantities. The regions which are not defined as either arm or interarm often show scatter of about a factor of 2, and do not always smoothly fit into a transition between the arm and interarm values. This is especially evident in the H_2 and HI data. Arm-interarm contrasts calculated in the above manner as well as the I-band arm azimuth ranges are listed in Table 4.2.

The arm-interarm contrasts present in both the B- and I-band azimuthal distributions increase with radius from the 0'.75 annulus to the 3'.00 annulus on the northeast arm complex. On the southwest arm complex, there is an increase with radius in the B- and I-band arm-interarm contrasts from R = 0'.75 to 2'.25, and slight decreases at R = 3'.00 (see Figures 4.12-4.13). The radial increase in the arm-interarm contrasts of the I-band data is indicative of an increase in the spiral arm amplitude; integrated over the lifetime of the galaxy, more star formation has occurred on the arms relative to the interarm regions in the outer disk.

In a photometric study of the spiral structure of six Sb and Sc galaxies, Schweizer (1976) found that the ratio of arm intensity to disk intensity increased roughly linearly with radius out to the point of the outermost HII region, with a possible decline beyond that point. He interprets this radial increase as an increase in spiral arm strength. The radial increases observed in the arm-interarm contrasts of the B- and I-band profiles in NGC 6946 are consistent with Schweizer's results, although we only

Table 4.2

Arm-Interarm Contrasts

Quantity	R = 0.75 $\frac{A_1}{\langle I \rangle}^{a,b}$	R = 0.75 $\frac{A_2}{\langle I \rangle}^{a,b}$	R = 1.50 $\frac{A_1}{\langle I \rangle}^{a,c}$	R = 1.50 $\frac{A_2}{\langle I \rangle}^{a,c}$
I	1.14±0.11	1.20±0.12	1.49±0.15	1.53±0.15
B	1.30±0.13	1.09±0.11	1.71±0.17	1.67±0.17
H_2	2.58±0.45	2.24±0.45	2.43±0.42	2.29±0.38
HI	1.78±0.22	1.97±0.23	1.21±0.12	1.84±0.16
Hα	5.56±0.55	4.97±0.49	5.14±0.51	4.44±0.44
H_2/HI	2.63±0.51	1.93±0.40	2.72±0.64	1.65±0.31
Hα/H_2	2.17±0.31	2.17±0.38	3.03±0.50	2.83±0.45
Hα/B	5.15±0.51	4.48±0.45	3.46±0.35	3.27±0.33

Quantity	R = 2.25 $\frac{A_1}{\langle I \rangle}^{a,d}$	R = 2.25 $\frac{A_2}{\langle I \rangle}^{a,d}$	R = 3.00 $\frac{A_1}{\langle I \rangle}^{a,e}$	R = 3.00 $\frac{A_2}{\langle I \rangle}^{a,e}$
I	1.75±0.18	2.03±0.20	1.99±0.20	1.58±0.16
B	2.61±0.26	2.47±0.25	3.05±0.31	2.22±0.22
H_2	3.84±0.68	4.11±0.69	6.95±1.84	8.20±2.11
HI	2.42±0.21	2.09±0.18	1.70±0.12	1.58±0.11
Hα	19.4±1.94	25.0±2.50	29.5±2.95	7.30±0.73
H_2/HI	2.75±0.51	3.20±0.56	4.98±1.37	6.45±1.72
Hα/H_2	8.71±1.37	23.8±3.45	17.3±2.59	7.31±1.38
Hα/B	9.82±0.98	11.9±1.19	12.5±1.25	3.81±0.38

[a] Arm 1/2 refers to the northeast/southwest arm complex.

[b] Arm azimuths at R = 0.75 are from 0° to 45° and 180° to 225°; interarm azimuths are from 90° to 135° and 280° to 315°.

[c] Arm azimuths at R = 1.50 are from 22° to 68° and 160° to 270°; interarm azimuths are from 90° to 135° and 293° to 340°.

[d] Arm azimuths at R = 2.25 are from 45° to 100° and 200° to 293°; interarm azimuths are from 125° to 170° and 325° to 0°.

[e] Arm azimuths at R = 3.00 are from 45° to 80° and 240° to 300°; interarm azimuths are from 350° to 45° and 145° to 170°.

observe a small decline in the arm-interarm contrasts in the southwest region of this galaxy.

There is a general trend of increasing arm-interarm contrast with radius evident in the H_2 surface densities and Hα surface brightnesses (Figures 4.14 and 4.16). This is the same trend that is seen in the I- and B-band arm-interarm contrasts. The HI surface density arm enhancements do not seem to be increasing with radius, however (see Figure 4.15). The atomic gas is the only component of the ISM which does not seem to be affected by the strength of the spiral arms in the inner parts of NGC 6946.

In Figures 4.17-4.18, both the $\mu(H\alpha)/\sigma(H_2)$ and $\mu(H\alpha)/\mu(B)$ ratios show a general radial increase in their arm-interarm contrast ratios, indicating that the massive star formation efficiency on spiral arms increases with radius. There are two obvious features which deviate from this general trend, however. At R = 2'.25, there is a very strong spiral arm enhancement in the $\mu(H\alpha)/\sigma(H_2)$ ratio which peaks at an azimuth of about 210°. The enhancement of the $\mu(H\alpha)/\sigma(H_2)$ ratio on this arm is much greater than for any other spiral arm in the galaxy. The arm enhancement of the I-band flux or the $\mu(H\alpha)/\mu(B)$ ratio is small on this arm. With the exception of the high $\mu(H\alpha)/\sigma(H_2)$ ratio on the spiral arm at ~210 azimuth, there is very little difference between the strengths of the spiral arm enhancements in the $\mu(H\alpha)/\sigma(H_2)$ ratios at radii of 2'.25 and 3'.00. Thus, the azimuthal variations of this ratio with radius mimic those of the I-band fluxes.

Figure 4.19 shows the azimuthal profiles of the $\sigma(H_2)/\sigma(Hl)$ ratios as a function of radius in NGC 6946. Here, a small increase in the arm-interarm enhancements is observed from R = 0'.75 to R = 3'.00. The $\sigma(H_2)/\sigma(HI)$ ratio may be less sensitive to spiral arm strength than the $\mu(H\alpha)/\sigma(H_2)$ and $\mu(H\alpha)/\mu(B)$ ratios because enhancements in the former ratio are often found away from optical spiral arm locations.

To better illustrate the radial variations in the spiral arm enhancements in NGC 6946, the arm-interarm contrasts in each of the previously discussed quantities are plotted as a function of radius for the two major spiral arms (Figures 4.20a and b). Figure 4.20a illustrates the arm-interarm contrasts with radius in arm 1. In this region of spiral structure, radial increases of nearly a factor of 2 from R = 0'.75 to 3'.00 in I-band arm enhancements, and more than a factor of 2 in the blue arm enhancements, are quite evident. Correspondingly, nearly a factor of 3 increase in the H_2 surface density and a factor of 6 increase in the Hα arm-interarm contrasts are observed from 0'.75 to 3'.00 in radius. As previously stated, the HI appears to have very small arm-interarm contrasts, and these contrasts do not vary in an orderly fashion with radius. If the I-band spiral arm amplitudes represent a true enhancement in the mass surface density as delineated by the underlying stellar population, then both the recent star formation and the molecular gas have responded to the density enhancement.

The arm-interarm contrasts in the $\sigma(H_2)/\sigma(HI)$, $\mu(H\alpha)/\sigma(H_2)$, and $\mu(H\alpha)/\mu(B)$ ratios for the northeast spiral arm complex are also shown in Figure 4.20a. These

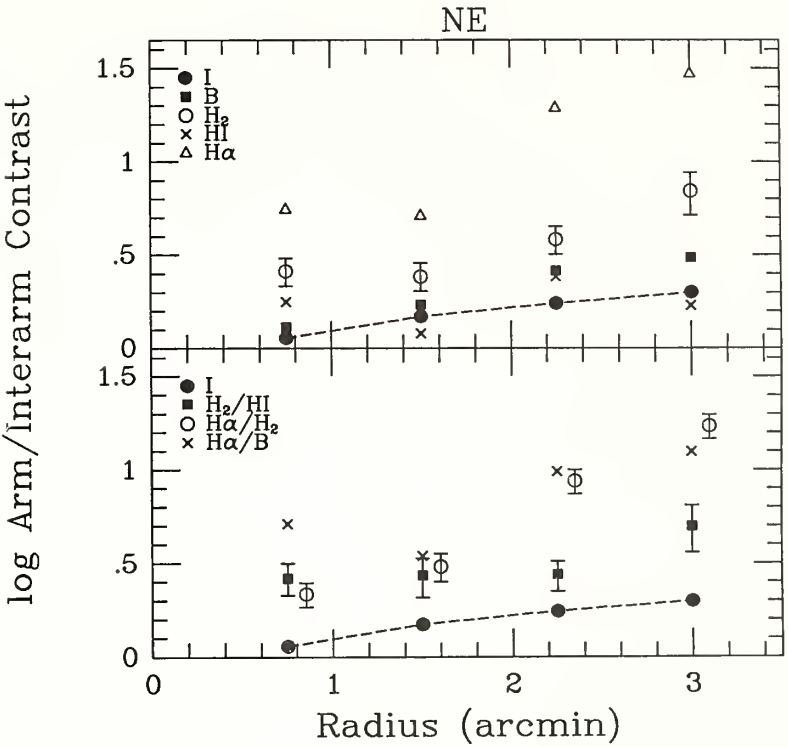

Figure 4.20a: The arm-interarm contrast ratios as a function of radius for the northeast arm complex. The points are coded as indicated to distinguish between different quantities. Error bars are shown where the uncertainties are larger than the points.

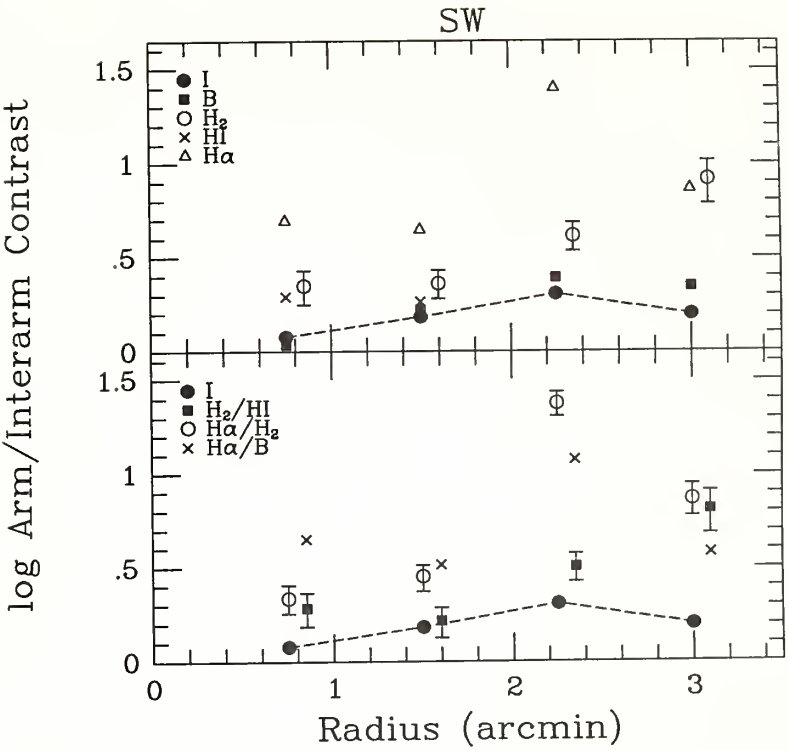

Figure 4.20b: The arm-interarm contrast ratios as a function of radius for the southwest arm complex. The points are coded as indicated to distinguish between different quantities. Error bars are shown where the uncertainties are larger than the points.

ratios exhibit radial increases of factors of 2 to 9 from R = 0'.75 to 3'.00. The most noticeable increase is evident in the $\mu(H\alpha)/\sigma(H_2)$ ratio. We infer from the radial variation in this ratio that the massive star formation efficiency is increasing with increasing spiral arm amplitude in this spiral arm region of NGC 6946. If the $\sigma(H_2)/\sigma(HI)$ ratio is a measure of the molecule production efficiency, then molecule production is not as sensitive to the spiral potential.

The arm-interarm contrasts in arm 2 are illustrated in Figure 4.20b and Table 4.2. In this region, the strongest I-band spiral arm amplitudes are found at a radius of 2'.25. There is a smooth increase in both the B- and I- band amplitudes out to this radius and then a slight decline at R = 3'.00. Radial increases of roughly factors of 2 are again observed in the B- and I- band amplitudes in this spiral arm complex. The Hα amplitudes show the most significant radial variation, with an increase of a factor of 5 evident from R = 0'.75 to 2'.25, while the H_2 surface density arm enhancements exhibit less than a factor of 2 increase over the same radius range. In arm 2, the HI surface densities exhibit very small, chaotic radial variations in the arm-interarm contrast ratio, as was also seen in arm 1. The arm-interarm contrasts in the $\mu(H\alpha)/\sigma(H_2)$ and $\mu(H\alpha)/\mu(B)$ ratios follow the B- and I-band arm amplitudes on arm 2. The greatest arm contrasts are observed in the $\mu(H\alpha)/\sigma(H_2)$ ratio, indicating that the massive star formation efficiency is very sensitive to an increase in spiral arm strength. The $\sigma(H_2)/\sigma(HI)$ ratio is found to be much less sensitive to radial variations in the I-band arm amplitude.

Following the method of Schweizer (1976), we have calculated the radial distributions of the HI and H_2 surface densities, and B- and I-band surface brightnesses for the spiral arms and the underlying disk using the arm and interarm values for the two arm complexes in NGC 6946. The resulting distributions are shown in Table 4.3 and Figure 4.21. The H_2, I- and B- disks are all found to fall off more steeply with radius than the arms. There is very little difference between the HI arms and disk, however. In his photometric study of the spiral structure of six spiral galaxies, Schweizer (1976) found that the optical disks of these galaxies exhibited a much more rapid radial decrease in surface brightness than did the spiral arms. Our study shows that the molecular disk and arms show this same radial behavior.

4.5 Discussion

In the original theory of Lin and Shu (1964), the density waves trigger the formation of gas clouds and stars. Recently, there has been a series of studies completed which suggest that the primary effect of a spiral density wave is to organize the ISM into a global spiral pattern, and that the observed spiral variation in the OB star formation efficiency on the spiral arms both in our galaxy and in other galaxies is due to orbit crowding in the spiral potential (Scoville, Sanders, and Clemens 1986; Elmegreen 1987 and references therein). In this picture the concentration of molecular gas is a purely kinematic concentration, and star formation in the arms results from cloud-cloud collisions (Scoville and Hersh 1979; Kwan and Valdes 1983). The effect of the orbit crowding is to cause smaller clouds to coalesce into

Table 4.3

Arm and Disk Scale Lengths

Component	Arm[a] (kpc)	Disk[a] (kpc)
H_2	5.3	2.7
HI	-14	-15
B	13	5.0
I	7.1	4.7

[a] Typical uncertainties are ±1 kpc.

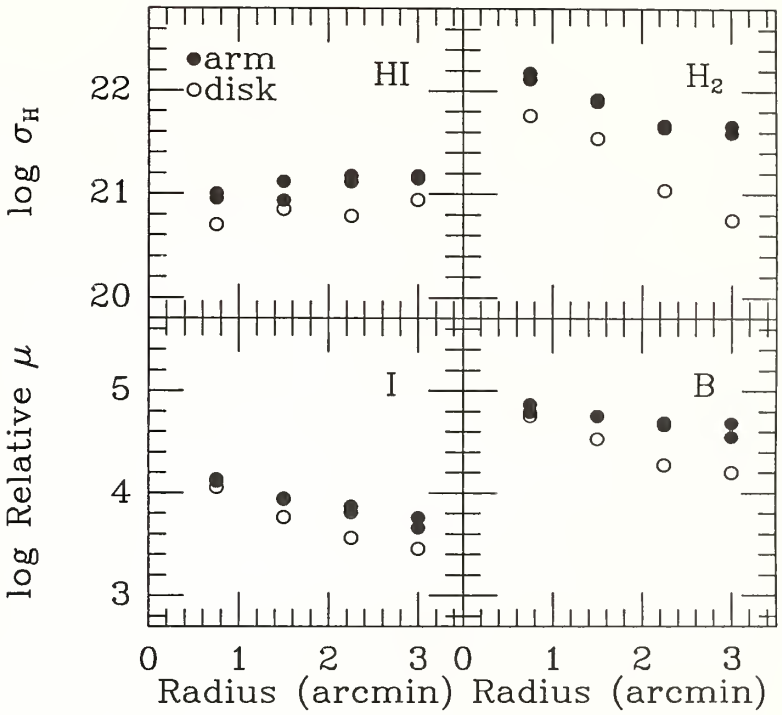

Figure 4.21: The arm and disk radial distributions for the HI and H_2 surface densities and I- and B-band surface brightnesses for NGC 6946. The arm and disk scale lengths have been calculated to be 1.'8 and 0.'92 for the H_2 surface density, -4.'8 and -5.'0 for the HI surface density, 2.'4 and 1.'6 for the I-band surface brightness, and 4.'5 and 1.'7 for the B-band surface brightness. Typical uncertainties in the scale lengths are ±0.'5.

giant cloud complexes, which will then fragment back into smaller clouds as a result of star formation (Scoville and Hersh 1979).

Elmegreen (1987) suggests that excess star formation in a spiral arm due to density wave triggering is much more probable in strong armed galaxies than in weak ones. The premise is that there are two effects which limit the formation of gas density enhancements from gravitational instabilities in spiral arms. The first effect is the rate of shear due to differential rotation. However, the timescale for shear should be long inside of a spiral arm, since the arm flow causes the rotational velocities to be solid body. A second limiting factor is the spiral arm flow-through time. Star formation (and cloud formation) can commence only after the gas is able to dissipate a large fraction of its kinetic and magnetic energy. If the arm flow-through time is long enough to allow for this dissipation of energy while the gas is compressed, then an excess of star formation (or cloud formation) will be observed. Since Elmegreen derives that the flow-through time is longer for strong density waves, he suggests that strong armed galaxies will have some excess star and cloud formation, but weaker armed galaxies will not show this effect.

Previous studies of NGC 6946 have attempted to determine the importance of density waves for star formation. DeGioia-Eastwood *et al.* (1984) have compared derived star formation rates (from Hα fluxes) with the amount of compression suffered by the gas due to the spiral shock. From density wave theory, DeGioia-Eastwood *et al.* assumed that the quantity $(\Omega - \Omega_P)\, r \sin(i)$ is a measure of the spiral shock strength

(Roberts, Roberts, and Shu 1980), where i is the pitch angle, Ω is the angular velocity of the stars and gas, and Ω_P is the spiral pattern speed. If the star formation rate were influenced by the density waves, DeGioia-Eastwood *et al.* expected to see a correlation between the SFR and $(\Omega - \Omega_P)\, r \sin(i)$. Since only a very weak correlation was observed, they concluded that the star formation rate was much more strongly influenced by other factors, such as the local gas density, than by the spiral density wave shock.

Klein *et al.* (1982) find from their 2.8 cm radio continuum maps that density waves are relatively unimportant in NGC 6946. Their maps show no indication for gas compression regions in this galaxy as has been found for other spiral galaxies at comparable spatial resolution. They argue that the lack of compression regions combined with the ill-defined spiral arms favor stochastic self-propagating star formation (SSPSF; Gerola and Seiden 1978) over density waves as the triggering mechanism for star formation.

Although the angular resolution of the data in this thesis is higher than that of Klein *et al.* and comparable to that of DeGioia-Eastwood *et al.*, we note that it is impossible to discern which of the above mentioned triggering mechanisms are responsible for regulating the massive star and molecule formation efficiencies in NGC 6946. Based on the azimuthal variations found in the previous section, we will discuss our results in light of these theories to lend evidence for or against the proposed mechanisms.

The differences between the brightest northeast spiral arm and the poorly defined spiral structure in the southwest are intriguing in relation to any triggering mechanism. At all four radii, there are peaks in the H_2, Hα, B-, and I-band emission on the bright northeast arm complex. Furthermore, the (Hα)/$\sigma(H_2)$, μ(Hα)/μ(B), and $\sigma(H_2)/\sigma$(HI) ratios are also high on the bright arm, indicating that the massive star formation and molecule production efficiencies may be higher on this arm complex compared to the interarm regions.

In the cloud-cloud collision models, the orbit crowding towards the spiral potential minimum causes small gas clouds to coalesce into massive cloud complexes (Scoville and Hersh 1979; Kwan and Valdes 1983, 1987). Colliding giant molecular clouds can then trigger massive star formation in their interface region (Scoville, Sanders and Clemens 1986). A definite increase in the massive star formation efficiency would then be observed on the spiral arms. Moreover, a slight enhancement in the gas density on the spiral arms is predicted due to the orbit crowding, although molecular clouds are expected to exist in the interarm regions as well, as they do in our Galaxy (Solomon, Sanders and Rivolo 1985; Kwan and Valdes 1987). These models are consistent with what we observe at 45" resolution in the northeastern regions of NGC 6946. There are arm-interarm contrasts of greater than a factor of 25 in the Hα fluxes, but no more than a factor of 8 in the H_2 surface densities. The spiral arm enhancements evident in the μ(Hα)/$\sigma(H_2)$, μ(Hα)/μ(B), and $\sigma(H_2)/\sigma$(HI) ratios are also expected in the cloud-cloud collision model. Smaller peaks are present in the H_2

and HI surface densities in the interarm regions; the presence of clouds between the spiral arms is consistent with a scenario in which cloud-cloud collisions may play an important role in the star formation history of NGC 6946.

The situation is more complex in the southwestern regions of the galaxy. Two of the three I-band spiral arms exhibit no enhancements in the Hα flux, $H\alpha/H_2$ or Hα/B ratios at several radii even though there are enhancements in the H_2 surface densities, and B and I intensities. Scoville, Sanders, and Clemens suggest that the confinement of the massive star formation to a spiral arm should depend on the amplitude of the spiral potential and the abundance of molecular clouds. The massive star formation efficiency should also depend on the width of the spiral potential since a broad arm will not have as strong an effect on the triggering of massive star formation as a narrow one. Since we observe similar B- and I-band arm-interarm contrasts in the northeastern and southwestern spiral arms (see Figures 4.8-4.11), we suggest that the differences in the star formation efficiencies in these two arm regions could be due to a broader spiral potential in the southwestern arm complex.

In the models of star formation resulting from cloud-cloud collisions in a spiral potential, an increase in the star formation efficiency is predicted with increasing spiral shock strength (Scoville, Sanders and Clemens 1986; Kwan and Valdes 1987; Elmegreen 1987). As previously discussed, the $\mu(H\alpha)/\sigma(H_2)$ ratio is a measure of the massive star formation efficiency, and the I-band arm-interarm contrasts are a measure of the spiral shock strength. The fact that the radial variations of the $\mu(H\alpha)/\sigma(H_2)$

arm-interarm contrasts mimic those of the I-band fluxes as shown in Figures 4.12 to 4.21 presents one of the most interesting conclusions of this chapter. The massive star formation efficiency seems to be a very sensitive function of the spiral arm amplitude, as evidenced by I-band arm increases of roughly a factor of two but $\mu(H\alpha)/\sigma(H_2)$ increases of up to a factor of 12 over a 3'.00 radius range. The increase in massive star formation efficiency with spiral arm strength in NGC 6946 lends very strong evidence for a scenario of star formation in which cloud-cloud collisions play an important role.

The radial variations in the $\mu(H\alpha)/\mu(B)$ spiral arm enhancements are much less straightforward to interpret. The arm-interarm contrasts in this ratio continue to increase from the 2'.25 to the 3'.00 annulus, even though there is no corresponding increase in the spiral shock strength. An increase in the $\mu(H\alpha)/\mu(B)$ ratio with radius may be due to an increase with radius in the amount of diffuse Hα emission which is missing from the Hα fluxes used in this thesis. A calibrated Hα image of NGC 6946 is needed to address this issue.

4.6 Conclusions

From this comparison study of the molecular and atomic gas distributions in NGC 6946 we have found:

1. The H_2 and HI surface densities do not appear to be globally correlated. When comparing the H_2 and HI surface densities with Hα, blue, and near infrared surface brightnesses, there is a good correlation between the H_2 surface density and all

three optical components, while the HI shows no correlation with the optical surface brightnesses.

2. The $\mu(H\alpha)/\sigma(H_2)$ ratio is roughly constant as a function of radius, indicating that the massive star formation efficiency is constant with radius averaging over azimuthal structures. The $\sigma(H_2)/\sigma(HI)$ ratio, on the other hand, is found to decrease steeply with radius. One interpretation is that there is a radial decrease in the molecule production efficiency. An alternative interpretation is that the HI is a destruction product of H_2, and is largely found in the envelopes of molecular clouds (Shaya and Federman 1987). A flat HI distribution results from having one cloud in every line of sight.

3. Complex spiral structure is evident in NGC 6946. The well defined, luminous spiral arms in the northeast are contrasted with the poorly defined spiral structure in the southwestern regions of this galaxy. In the regions of well defined spiral structure in the northeast, we find enhancements in the H_2 surface densities, $H\alpha$ surface brightnesses, $\mu(H\alpha)/\sigma(H_2)$, and $\sigma(H_2)/\sigma(HI)$ ratios on the arms. In the southwest, however, enhancements in the H_2 surface density on the arms are not often followed by enhancements in the $H\alpha$ flux, or the $\mu(H\alpha)/\sigma(H_2)$ ratio.

4. At a given radius, the spiral arm-interarm contrasts are much greater in the $H\alpha$ surface brightness and $\mu(H\alpha)/\sigma(H_2)$ ratios than in the H_2 surface density. From the $H\alpha/H_2$ ratios, we infer that the massive star formation efficiency is greater in the spiral arms than in the interarm regions. This large increase in massive star formation

efficiency in spiral arms, along with slightly increased H_2 surface densities in the arms, and the presence of small peaks in the HI and H_2 surface densities in the interarm regions are all consistent with a scenario where cloud-cloud collisions play an important role in the star formation process.

5. There are increases with radius evident in the spiral arm amplitudes as derived from B- and I-band spiral arms. Large radial increases in the arm-interarm contrasts in the Hα flux and massive star formation efficiency are also prominent, with smaller increases observed in the H_2 surface density contrasts. No radial variations in the HI arm-interarm contrasts are seen. We suggest that the massive star formation efficiency is a sensitive function of the spiral arm strength.

CHAPTER 5

THE CO CONTENTS OF DWARF IRREGULAR GALAXIES

5.1 Introduction

Although dwarf galaxies may be the most abundant type of galaxy in the universe, they are among the least studied. Their intrinsically small sizes, faint luminosities and low surface brightnesses make all but the closest dwarfs extremely difficult to study at most wavelengths. Because of this, dwarf galaxies are poorly represented in the standard catalogs of galaxies, and thus their properties are not very well understood.

Irregular dwarf galaxies are known to contain considerable amounts of atomic gas (*e.g.* Fisher and Tully 1975; Thuan and Seitzer 1979; Gordon and Gottesman 1981; Thuan and Martin 1981) and to be characterized by roughly exponential light distributions like spirals (*e.g.* Ables 1971; Karachentseva, Schmidt and Richter 1984; Hunter and Gallagher 1985). They span a wide range of observed colors from red, low surface brightness objects to blue, high surface brightness compact galaxies.

The metal deficiencies of dwarf irregular galaxies have led investigators to suggest that either the very blue systems are young galaxies which have recently formed out of protogalactic gas clouds, or that both red and blue dwarf irregular galaxies undergo intermittent bursts of star formation followed by periods of quiescence over the lifetimes of the galaxies (Searle, Sargent and Bagnuolo 1972; Huchra 1977). These authors and others (*e.g.* Gerola, Seiden and Schulman 1980) suggest that the red irregular galaxies are the quiescent counterparts of the blue, high surface brightness

dwarf systems. More recently, Thronson and Telesco (1986) have calculated current and recent star formation rates from IR and blue fluxes for a sample of blue compact dwarf galaxies, and find that at least 5 to 10 percent of their sample show current star formation rates which are much greater than those of the past ~6×10^9 years.

Since stars form in molecular clouds, measurements of the amount of molecular gas in dwarf galaxies are essential to the understanding of the potential for star formation in these systems and to their overall evolution. A galaxy which has just undergone an intense episode of star formation may have had its supply of molecular gas depleted, whereas a galaxy which has been quiescent for a long period may be rebuilding its molecular reservoir.

To determine the amount of molecular gas in a sample of dwarf galaxies, we have observed the central 45" of 15 objects in the ^{12}CO line at 2.6 mm, and detected CO in five. Previous observations of *giant* irregular galaxies have shown them to be deficient in CO emission by factors of 30 to 70 compared to spiral galaxies (*e.g.* Elmegreen, Elmegreen and Morris 1980; Young, Gallagher and Hunter 1984; Tacconi and Young 1985). Our sample was chosen to span wide ranges in galaxy color and infrared luminosity among those dwarfs with detectable 21-cm line emission, in order to enable determination of the total gas contents of these galaxies. The 15 program galaxies chosen are listed in Table 5.1 along with their global properties.

Table 5.1

Global Properties of Dwarf Galaxies

References to Table 5.1

1 Christian and Tully 1983

2 deVaucouleurs, deVaucouleurs and Buta 1981

3 deVaucouleurs, deVaucouleurs and Corwin 1976

4 Fisher and Tully 1975

5 Fisher and Tully 1979

6 French 1980

7 Kraan-Kortweg and Tammann 1979

8 Sargent, Sancisi and Lo 1983

9 Schild 1980

10 Thuan 1983

11 Thuan and Martin 1979

12 Thuan and Martin 1981

Table 5.1

Global Properties of Dwarf Galaxies

Name	RA	Dec	V_{sun}	D	D_{25}	$10^7 L_B$	B-V	Refs
	hh mm ss.s	dd mm ss	km s^{-1}	Mpc	arcmin	L_o		
LGS-3	01 01 12.0	21 37 00	-280	0.82	2.00	0.06	0.70	1,9,11
IIZw40	05 53 04.8	03 23 06	806	14.0	0.33	17	-0.13	3,6,12
DDO47	07 39 03.0	16 55 06	266	4.30	4.67	4.5	0.46	2,3,4
DDO50	08 13 43.2	70 52 18	158	3.25	7.59	95	0.32	2,3,4
M81DwA	08 18 42.0	71 11 36	113	3.25	1.70	0.36	0.51	8
DDO69	09 56 31.8	30 59 12	27	1.60	4.90	4.0	0.21	2,3,4,7
Mkn35	10 42 16.2	56 13 24	865	17.3	1.48	270	0.47	3,12
DDO95	11 21 51.0	03 36 18	1394	20.0	2.04	640	0.37	2,3,4
IZw36	12 23 50.4	48 46 06	287	7.52	0.87	5.7	0.39	3,10,12
DDO135	12 31 17.4	15 26 36	263	20.0	2.63	130	0.37	2,3,4
DDO155	12 56 10.2	14 29 12	222	2.34	1.20	3.1	0.30	2,3,4
IIZw70	14 48 54.0	35 47 00	1147	22.9	0.83	110	-0.32	3,6,12
DDO210	20 44 07.8	-13 02 00	-130	1.50	2.09	0.26	----	3,4,5
DDO216	23 26 03.0	14 28 18	-178	1.60	4.57	6.1	0.65	2,3,4,5
DDO218	23 32 22.2	17 57 00	1395	31.6	1.51	380	0.40	2,3,4

5.2 Observations

5.2.1 CO Emission

The 15 dwarf galaxies were observed in the ^{12}CO line at 2.6 mm with the 14-meter antenna of the Five College Radio Astronomy Observatory (FCRAO)[1] during 1986 April-June. The telescope was equipped with a 3-mm cooled mixer receiver with $T_{SSB} \approx$ 200 K. At the frequency of the ^{12}CO J=1→0 transition (115.271203 GHz), the half-power beam width of the telescope is 45". Telescope pointing was checked at the beginning of each run by observing the standard sources IRC+10216, OrionHV, or planets, and was found to have an accuracy of ±5" rms. Data were obtained by position switching every 30 seconds to locations 5'-7' east and west of the center of each galaxy, for a total of 3-4 hours of integration per point. Antenna temperature calibration was performed using the chopper wheel method, and the data were scaled by η_{fss} such that the center of the Orion Nebula (KL) has $T_R^* = 72$ K. The spectra were resolved with 512 1-MHz channels for those galaxies whose HI half-power line widths are greater than 50 km s^{-1}, and with 512 250-kHz channels for those objects with HI line widths less than 50 km s^{-1}.

Of the 15 objects in our sample, we have detected ^{12}CO in five galaxies and marginally detected CO (at the 3σ level) in one galaxy, with integrated intensities

1. FCRAO is operated with support from the National Science Foundation under grant AST-82-12252 and with permission of the Metropolitan District Commission, Commonwealth of Massachusetts.

ranging from 0.5 to 2.0 K km s^{-1}. Since the observed CO features are very weak, all detections were reobserved on a different day to confirm that the features were real. In Table 5.2 we compare the CO and HI velocities and linewidths, and show fair agreement in all cases. The differences in the CO and HI linewidths can be attributed to the fact that while the CO beam is only sampling gas in the inner 45" of the galaxy, the HI is often extended far beyond that. The CO spectra of three of the detected galaxies are shown in Figure 5.1.

The detected galaxies surprisingly span the entire range in IR luminosity and colors of our sample. Three of the CO detections were in the blue compact dwarf galaxies, IIZw40, IZw36, and Mkn 35, which are presently undergoing intense star formation activity as evidenced by their large numbers of HII regions; one galaxy which has an intermediate level of star formation, DDO 218, was also detected. Additionally, we have detected CO in two dwarf galaxies which exhibit no real signs of present day star formation, LGS-3 and DDO 69 (a 3σ detection). We note that these last two objects are members of the Local Group and thus are more easily detectable than their more distant counterparts.

We have calculated the CO luminosities for the central 45" region of each galaxy assuming $L_{CO} = I_{CO}(\pi r^2)$ (K km kpc^2), where r is the radius of the 45" beam on the galaxy in kpc. The true CO luminosity may be somewhat larger, since we have not completely sampled the galaxy, but in the majority of cases we have sampled ≥50% of the optical disk. We have also estimated the H_2 masses of these galaxies based on the

Table 5.2

CO and HI Velocities[a]

Name	V_{HI} km s^{-1}	ΔV_{HI} km s^{-1}	V_{CO} km s^{-1}	ΔV_{CO} km s^{-1}
LGS-3	-280	73	-310	15
11Zw40	895	143	850	42
DDO69	23	19	20	25
Mkn35	944	96	917	41
IZw36	279	47	288	32
DDO218	1400	70	1457	130

[a]All velocities are with respect to the sun. HI data are from Fisher and Tully (1975), Thuan and Martin (1979 and 1981), and Sargent, Sancisi and Lo (1983).

Figure 5.1: CO spectra for three of the dwarf galaxies in our sample. The spectra were Hanning smoothed to 7 km s^{-1} for LGS-3, 15 km s^{-1} for IIZw40, and 20 km s^{-1} for DDO 218.

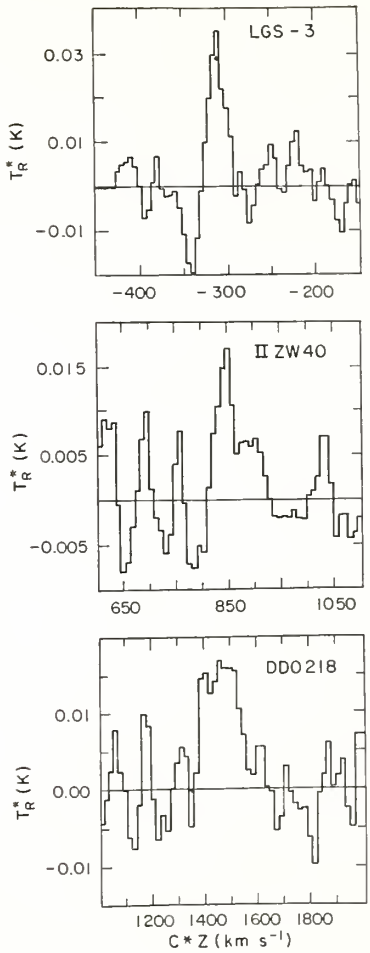
LGS - 3
0.03
0.01
-0.01
T_R^* (K)
-400
-300
-200
II ZW40
0.015
0.005
-0.005
T_R^* (K)
650
850
1050
DDO 218
0.01
0.00
-0.01
T_R^* (K)
1200
1400
1600
1800
C*Z (km s^{-1})

conversion between H_2 column densities and CO integrated intensities derived by Bloeman *et al.* (1986) of 2.8×10^{20} (H_2 cm^{-2})/(K km s^{-1}). Additionally, to convert the CO integrated intensities to H_2 surface densities, the data must be corrected to a T_R scale, to account for the coupling of the main beam to the source. To do this, the I_{CO} values must be divided by η_c, the beam coupling efficiency. The source beam coupling efficiency is roughly unity for observations of Milky Way molecular clouds taken at FCRAO such that $T_R = T_R^*$. For small galaxies, like the dwarf irregulars studied here, η_c has been estimated to be about 0.5 (Kenney 1987 and Kenney and Young 1987). Since the metallicities of these galaxies are lower than that in the solar neighborhood by factors of 5-10, the standard CO/H_2 conversion may underestimate the H_2 mass in galaxies of low metallicity (Elmegreen, Elmegreen and Morris 1980; Young, Gallagher and Hunter 1984; Tacconi and Young 1985). Additionally, Israel *et al.* (1986) find that CO emission from the Magellanic clouds is much weaker than that from Galactic objects. These authors attribute the low CO abundance to relatively low C and O abundances, relatively low dust-to-gas ratios, and relatively strong UV radiation fields, and also suggest that using CO to trace the molecular gas content in irregular galaxies may lead to underestimates in the molecular gas mass in these systems. Based on dust mass estimates from 150 μm observations, Thronson *et al.* (1986) suggest that the conversion between I_{CO} and N_{H_2} may underestimate the H_2 mass in irregular galaxies by an order of magnitude. We compute the H_2 masses here primarily for comparison purposes among the dwarf galaxies. CO fluxes,

luminosities, and the associated errors are listed in Table 5.3, and H_2 masses are given in Table 5.4.

5.2.2 Infrared Emission

The 12, 25, 60 and 100 μm fluxes of the dwarf galaxies were determined from coadded IRAS survey data using the Addscan routine with the February 1986 calibration factors. In all cases, the median scan was used to determine the flux densities; none of the objects were found to have extended emission. Eight of the fifteen dwarf galaxies in our sample were found to have 60 and 100 μm emission at the 3σ level or greater, while only four objects were detected at 12 or 25 μm (see Young *et al.* 1987). Two sigma upper limits were calculated for the remaining objects. The total IR luminosity from 40 μm to 300 μm was calculated for each galaxy using the 60 and 100 μm flux densities by the method described in the IRAS Extragalactic Catalogue (Lonsdale *et al.* 1985), and is listed in Table 5.3, along with the 60 μm and 100 μm flux densities.

5.3 Results

As shown in Table 5.3, those galaxies with the highest IR luminosities, such as DDO 218 and Mkn 35, also have the highest CO luminosities, while those objects with low IR luminosities, such as LGS-3 and DDO 69, also have low CO luminosities. In addition, the dwarf galaxies with high IR luminosities are also those galaxies with high blue luminosities, while the reverse is true for the galaxies with low IR

Table 5.3

CO and IR Properties of Dwarf Galaxies

Notes to Table 5.3:

[a] Errors are 1σ based on the peak-to-peak noise; upper limits are 2σ.

[b] IR fluxes for IZw36 are extremely uncertain due to the lack of IRAS sky coverage.

Table 5.3

CO and IR Properties of Dwarf Galaxies

Name	I_{CO}[a]	L_{CO}[a]	S(60μm)[a]	S(100μm)[a]	L_{IR}[a]
	K km s^{-1}	K km s^{-1} kpc^2	Jy	Jy	10^7 L_o
Class I					
IIZw40	0.62	4.54	6.16	6.17	256
	0.15	1.10	0.17	0.71	9.7
Mkn35	0.74	8.26	5.16	6.57	324
	0.18	2.35	0.05	0.06	2.3
[b]IZw36	0.61	1.40	0.57	0.50	<6.8
	0.15	0.19			
IIZw70	<0.52	<10	0.72	1.20	89
			0.04	0.09	4.0
Class II					
DDO47	<0.61	<0.26	0.14	0.64	1.4
			0.03	0.07	0.15
DDO50	<0.61	<0.28	1.53	2.38	3.7
			0.08	0.11	0.14
DDO95	<1.10	<26	0.96	1.84	97
			0.05	0.09	3.5
DDO135	<0.76	<11	0.82	1.63	85
			0.04	0.11	3.4
DDO155	<0.32	<0.15	0.19	<0.22	<0.22
			0.04		
DDO218	2.43	91	0.76	1.58	201
	0.41	12	0.03	0.10	7.2
Class III					
LGS-3	0.76	0.02	<0.10	<0.28	<0.02
	0.15	0.005			
M81Dwa	<0.37	<0.17	<0.05	<0.19	<0.23
DDO69	0.47	0.05	0.09	0.27	0.08
	0.17	0.02	0.03	0.08	0.02
DDO210	<0.41	<0.03	<0.09	<0.18	<0.05
DDO216	<0.38	<0.03	<0.09	<0.18	<0.06

Table 5.4

Derived Properties of Dwarf Galaxies

Name	M_{H_2}	M_{HI}[a]	$10^7 L_{IR}/L_{CO}$	L_{IR}/L_B	$M(HI)/L_B$	$M(H_2)/L_B$
	$10^7 M_o$	$10^7 M_o$			M_o/L_o	M_o/L_o
Class I						
IIZw40	4.19	63	56	15.1	3.71	0.25
Mkn35	7.63	54	39	1.20	0.20	0.03
IZw36	1.19	4.1	<4.8	<1.20	0.72	0.21
IIZw70	<0.46	34	>8.9	0.81	0.31	<0.01
Class II						
DDO47	<0.25	30	>5.4	0.31	6.67	<0.06
DDO50	<0.26	69	>13	0.04	0.73	<0.01
DDO95	<23	370	<3.7	0.15	0.58	<0.04
DDO135	<11	170	>7.7	0.65	1.31	<0.08
DDO155	<0.13	0.46	----	<0.07	0.15	<0.04
DDO218	83	350	2.2	0.53	0.92	0.22
Class III						
LGS-3	0.01	0.02	<1.1	0.32	0.32	0.17
M81dwa	<0.16	1.1	----	<0.64	3.06	<0.44
DDO69	0.04	4.1	1.6	0.02	1.03	0.01
DDO210	<0.03	0.30	----	<0.19	1.15	<0.12
DDO216	<0.03	0.65	----	<0.01	0.11	<0.01

[a] HI masses are from Fisher and Tully (1975), Thuan and Martin (1978, 1981), and Sargent, Sancisi, and Lo (1983).

luminosities. This is the well known property that larger galaxies have more of each component.

We have compared the CO and IR properties of our sample of 15 dwarf irregular galaxies with those of the four previously studied giant irregular galaxies, NGC 1569, NGC 3738, NGC 4214, and NGC 4449 (Young, Gallagher and Hunter 1984; Tacconi and Young 1985), with a sample of luminous spiral galaxies (Young *et al.* 1986a, Table 5.4), and with the isolated and interacting galaxy samples of Young *et al.* (1986b). Figure 5.2 illustrates that the entire sample spans a range of more than six orders of magnitude in both CO and infrared luminosity.

We have made power law fits to the data for the sample of dwarf and giant irregulars, and for the entire sample shown in Figure 5.2, and find fairly good agreement in the relationship between IR and CO luminosity for the data sets. For the giant and dwarf irregulars, we find that

$$L_{IR} = 1.2(\pm 0.5) \times 10^8 \, L_{CO}^{\,1.24\pm0.16} \qquad (1)$$

with a correlation coefficient of 0.88; the relationship for the entire sample is

$$L_{IR} = 0.8(\pm 0.3) \times 10^8 \, L_{CO}^{\,1.03\pm0.05} \qquad (2)$$

with a correlation coefficient of 0.93. Within the errors, the infrared luminosity goes as the first power of the CO luminosity for all classes of late type galaxies. The dwarf galaxies extend by more than four orders of magnitude in luminosity the correlation of

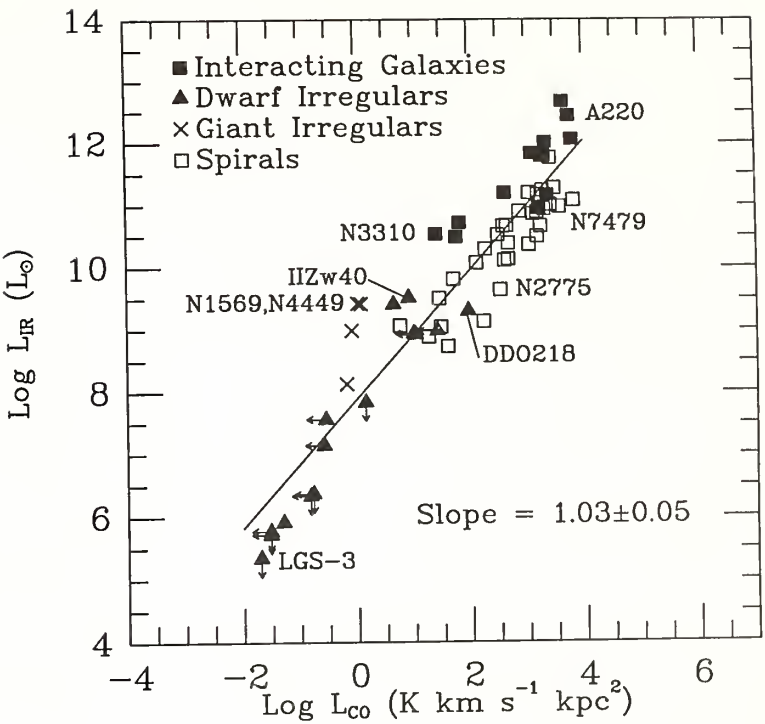

Figure 5.2: A comparison of IR and CO luminosities for the 15 dwarf irregular galaxies of this study (filled triangles), 4 giant irregular galaxies from Tacconi and Young (1985) and Young, Gallagher and Hunter (1984) (crosses), a sample of interacting galaxies from Young *et al.* (1986b) (filled squares) and a sample of spiral galaxies from Young *et al.* (1986a and b) (open squares). The fit to the entire sample is indicated. Upper limits were assigned their 2σ values in the fit.

IR and CO luminosities found previously for the luminous spiral galaxies alone (Young *et al.* 1986a).

There is, however, a fair amount of scatter in Figure 5.2, which can be investigated by determining the ratio of L_{IR}/L_{CO} for each galaxy. The dwarf galaxies studied here have L_{IR}/L_{CO} ratios which range over more than an order of magnitude, while the previously studied giant irregular galaxies have higher ratios of L_{IR}/L_{CO} than the dwarf galaxies, with an overall range in L_{IR}/L_{CO} similar to that found for spiral galaxies (Young *et al.* 1986a). We demonstrate in the next two sections that the *red* dwarfs have the lowest L_{IR}/L_{CO} ratios, while the blue dwarfs have the highest values of this ratio. We interpret this as evidence for depleted molecular reservoirs in the blue galaxies which have already experienced bursts of star formation, and the build-up of molecular gas in the pre-burst red dwarfs.

In Figure 5.3, we have plotted the ratio of L_{IR}/L_{CO} as a function of the far-infrared luminosity for the galaxies shown in Figure 5.2. The interacting galaxies shown in Figure 5.3, which are among the most infrared luminous of the sample, have high L_{IR}/L_{CO} ratios (Young *et al.* 1986b), and several of the giant and dwarf irregular galaxies have comparable or *higher* L_{IR}/L_{CO} ratios, while having far infrared luminosities which are *two orders of magnitude lower* than those found for the interacting sample of galaxies. It is not necessary to have a high far infrared luminosity to have a high ratio of L_{IR}/L_{CO}.

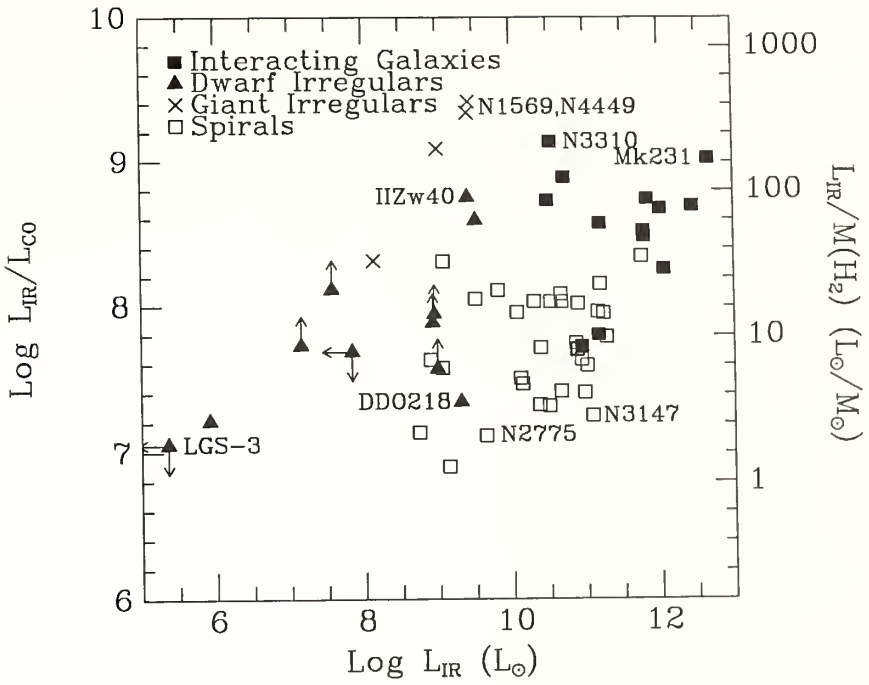

Figure 5.3: A comparison of the L_{IR}/L_{CO} ratio plotted as a function of L_{IR} for the same samples of galaxies as in Figure 5.2. Symbols for the different types of galaxies are coded as in Figure 5.2. Upper limits are 2σ.

If the far infrared luminosity is due to dust heated by young stars embedded in molecular clouds (*e.g.* Telesco and Harper 1980), thereby tracing the young stellar population, and if the CO luminosity is a measure of the available supply of molecular gas, then Young *et al.* (1986a) argue that the quantity L_{IR}/L_{CO} is a measure of the star formation efficiency (SFE) in a galaxy. While this is probably true in galaxies with $M(H_2) > M(HI)$, the IR luminosity in galaxies whose ISM is largely atomic may be primarily from dust in atomic clouds. In this case, the ratio L_{IR}/L_{CO} may not be a measure of the efficiency of star formation, since the heating sources for the dust may not be young stars, but the ambient radiation field. Given the variety of possible sources for the IR luminosity in a galaxy, and the uncertainty in H_2 masses for dwarfs relative to spiral galaxies, it is remarkable that the data in Figure 5.2 indicate as smooth a trend as they do from low to high luminosity galaxies.

5.4 Properties of Dwarf Galaxies

We now describe specific features of those dwarf galaxies in which CO was detected. We have divided the galaxies into three classes according to their star formation properties.

5.4.1 Class III: Galaxies with No HII Regions

LGS-3 and DDO 69 show the least evidence for present day star formation of any of the dwarf galaxies in which CO was detected. Both are presumably Local Group members, and are very low surface brightness objects. LGS-3 is perhaps the best

example known of a quiescent dwarf irregular galaxy where the most recent star formation occurred several billion years ago. Schild (1980) and Christian and Tully (1983) note that this galaxy is unique among gas rich dwarf galaxies in the sense that it resolves into stars better on R plates than either U or B plates, which is consistent with the idea that no star formation has occurred in the recent past.

LGS-3 and DDO 69 have the lowest CO luminosities of any galaxies in which CO has been detected. DDO 69 has been marginally detected at 60 μm and 100μm with the IRAS satellite; no far IR emission was detected from LGS-3. Low IR luminosities in these two galaxies are consistent with very low present day star formation rates. Additionally, the very low L_{IR}/L_{CO} ratios in these two galaxies may indicate that stars at the present epoch are forming with very low efficiency. However, the fact that we do observe some CO emission is indicative that there is a reservoir for a future burst of star formation in both galaxies.

5.4.2 Class II: Galaxies With an Intermediate Level of Star Formation

DDO 218 is the only object in our "intermediate level of star formation" class in which we have detected CO. It is the largest system in our sample, and also the most distant. The CO and IR luminosities of DDO 218 are among the highest of the dwarf galaxies in our sample. Despite its high IR and CO luminosity, Hunter and Gallagher (1985) find a very low global star formation rate for this galaxy (relative to other dwarf galaxies of roughly the same IR luminosity) with only four obvious star forming regions. We also find that DDO 218 has a L_{IR}/L_{CO} ratio between that of galaxies

in Classes I and III, indicating that it is not forming stars very efficiently at the present epoch.

5.4.3 Class I: Dwarf Galaxies With Intense Star Formation

Our Class I galaxies are labeled by Thuan and Martin (1981) and other authors as blue compact dwarf galaxies. They are all characterized by blue U-B and B-V colors and compact regions of intense star forming activity. Of the three galaxies we have detected here, IIZw40 is perhaps the most extreme example of a blue compact dwarf galaxy (BCDG). Based on near infrared observations, IIZw40 shows very little evidence for an old stellar population, and unlike other BCDG's, it exhibits a very strong nonthermal component to its radio spectrum (Wynn-Williams and Becklin 1986). IZw36 and Mkn 35 are more typical of BCDG's in that although they are also presently undergoing intense star formation activity, near IR observations indicate an older population of G, K and M giants (Viallefond and Thuan 1983; Thuan 1983). The radio spectra of BCDG's are also dominated by free-free emission, and show few signs of synchrotron radiation (Viallefond and Thuan 1983; Klein, Wielebinski and Thuan 1984).

These galaxies, like the other dwarf galaxies in our sample have very weak CO emission, although their infrared luminosities are somewhat higher than those of the quiescent galaxies in our sample (see Table 5.3). IZw36 lies in a region of the sky which had poor IRAS coverage, and we have calculated an upper limit to the IR luminosity based on two passes made by IRAS at 60 and 100 μm. IIZw40 and Mkn 35

have the highest L_{IR}/L_{CO} ratios of our sample, indicating that they may be presently forming stars more efficiently than any of the other dwarf galaxies. Because of our very uncertain estimate of the IR luminosity in IZw36, its star formation efficiency cannot be determined based on the present data.

5.4.4 The ISM of Dwarf Irregular Galaxies

We have compared the inferred H_2 masses with previously determined total HI masses (Fisher and Tully 1975; Sargent, Sancisi and Lo 1980; Thuan and Martin 1979, 1981) to determine the percentages of the ISM in the molecular and atomic phase. The H_2/HI ratios vary over two orders of magnitude and are not correlated with the IR luminosity of the galaxy (see Table 5.4). LGS-3, with an IR luminosity of $<2.5\times10^5$ $L_\odot$, has an H_2/HI ratio of 0.5, and thus has 33% of its ISM mass in molecular form, whereas DDO 69, also a very infrared faint galaxy, has an H_2/HI ratio of 0.008 and only ≈1% of its ISM mass in molecular form. IIZw40 and Mkn 35, both of which have large IR luminosities, also have very low H_2/HI ratios and very small fractions of their ISM in molecular form. We suggest that most dwarf irregular galaxies have not been able to convert their large reservoirs of atomic gas into molecular gas, which results in the small H_2/HI ratios. A possible explanation for this is that there may be a lack of dust grains on which to form H_2 from HI. Dwarf galaxies are known to have low metallicities and few dark nebulae relative to spirals (*e.g.* Hunter and Gallagher 1985; Hunter 1982). A second explanation as to why HI would be inefficiently converted into H_2 in dwarf galaxies as outlined in Young, Gallagher and Hunter

(1984), is that the gas volume density in irregulars is lower than in spirals, assuming that the gas scale height is proportional to the reciprocal of the mass density. Since irregular dwarf galaxies have lower mass densities than spirals, they presumably also have larger gas scale heights, and thus lower volume densities. Large gas scale heights and low gas volume densities have also been invoked to explain the low H_2/HI ratios observed in the outer disks of spiral galaxies (Chapter 2).

5.5 Evidence For Bursts of Star Formation

In Figure 5.4 we show a histogram of the L_{IR}/L_{CO} ratio for each of out three star formation classes. This figure illustrates that the Class III (low star formation rate) dwarf galaxies have the lowest L_{IR}/L_{CO} ratios, while Class I (high star formation rate) objects have the highest value of this ratio. This trend is exactly what would be expected from systems which form stars in brief, but intense episodes followed by long periods of relative quiescence.

Since stars form in molecular clouds, a galaxy which has just undergone an intense burst of star formation may have had its supply of gas depleted or dissociated. Assuming that the infrared luminosity is largely due to dust heated by young stars, and that the CO luminosity is tracing the molecular gas, such a galaxy would be expected to have a high infrared luminosity and a low CO luminosity, thereby resulting in a high L_{IR}/L_{CO} ratio. This is exactly what we observe in the active blue compact galaxies such as IIZw40 and Mkn 35. On the other hand, a pre-burst galaxy may have had time to replenish its supply of molecular gas, but not yet show signs of present day

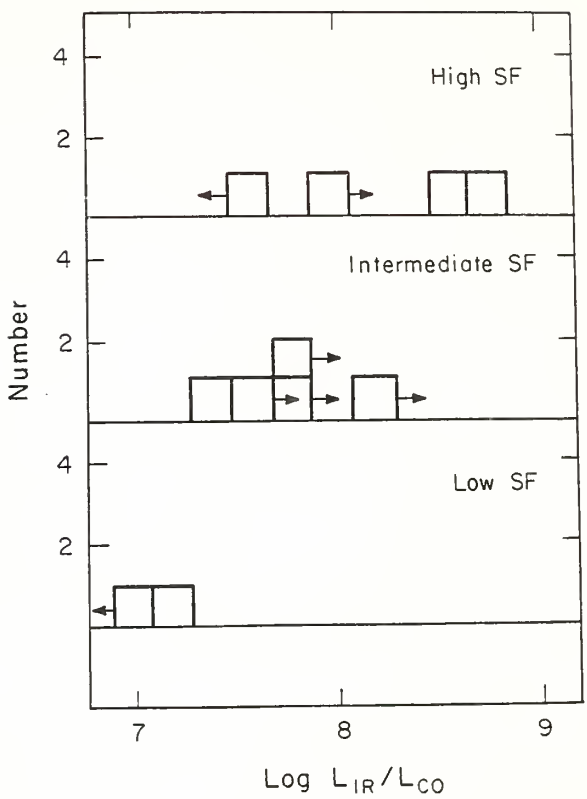

Figure 5.4: A histogram comparison of the L_{IR}/L_{CO} ratio for 11 of the 15 dwarf galaxies in our sample.

star formation. In this case, a low L_{IR}/L_{CO} ratio would be observed. As shown in Figure 5.4, we see the lowest L_{IR}/L_{CO} ratios in the red dwarf galaxies such as LGS-3. We interpret Figure 5.4, therefore, as support for a bursting mode of star formation in dwarf galaxies, where Class I galaxies are presently undergoing a burst of star formation, and Class III systems are candidates for a future burst of star formation.

One particularly interesting dwarf galaxy is IIZw40; it has the highest L_{IR}/L_{CO} ratio found for the dwarf galaxies, and resembles its giant irregular counterparts in that it is presently forming stars more efficiently than other dwarf galaxies. In fact, the L_{IR}/L_{CO} ratio of this galaxy is very similar to those found for the interacting galaxies shown in Figure 5.3 (Young *et al.* 1986b). IIZw40 also has an L_{IR}/L_{B} ratio of almost 15, which may be further evidence that the galaxy is presently undergoing a burst of star formation (*e.g.* Searle,Sargent and Bagnuolo 1973). IIZw40 is interesting in another sense; optical photographs of this galaxy reveal faint tails extending to the south and southeast of the nucleus. These tails could be an indication that IIZw40 is the result of a merger of two dwarf galaxies (*e.g.* Joy 1986 and references therein). The present burst of star formation could have been induced by such a merger, although we cannot rule out the stochastic processes normally held responsible for enhancements of star formation in dwarf galaxies.

5.6 Conclusions

From our study of the CO contents of 15 dwarf irregular galaxies we find:

1. CO was detected in six dwarf galaxies spanning the entire range in optical color and IR luminosity, from the red, inactive dwarf LGS-3, to the blue compact galaxy, IIZw40.

2. The dwarf galaxies extend by three orders of magnitude in luminosity the correlation between IR and CO luminosities found for spiral galaxies, The IR luminosity is proportional to the first power of the CO luminosity for all classes of late-type galaxies, although there is a fair amount of scatter in the relationship.

3. For the dwarf galaxy sample alone, those galaxies with the least evidence for ongoing star formation have the lowest L_{IR}/L_{CO} ratios, while the active, blue dwarfs have the highest values of this ratio. We interpret this as evidence for depleted molecular reservoirs in the blue galaxies which have already experienced bursts of star formation, and a build-up of molecular gas in the pre-burst, red dwarfs.

4. For galaxies with L_{IR} between 10^8 and 10^{12} $L_{\odot}$, we find the full range of L_{IR}/L_{CO} values at each luminosity. Thus, it is not necessary to have a high far infrared luminosity to have a high ratio of L_{IR}/L_{CO}. If L_{IR}/L_{CO} is a measure of the efficiency of star formation, the blue dwarf galaxies may be forming stars as efficiently as the IR luminous galaxies Arp 220 and NGC 6240.

5. The ratio of L_{IR}/L_{CO} in IIZw40 is the highest of any galaxy in the present sample, and is comparable to the values found in interacting galaxies (Young *et al.* 1986b). Along with the optical evidence for tidal tails (*cf.* Joy 1986), IIZw40 may be an example of a merger remnant among dwarfs.

CHAPTER 6

THE ROLES OF THE ATOMIC AND MOLECULAR GAS COMPONENTS OF NGC 6946 AND DWARF IRREGULAR GALAXIES

6.1 Introduction

The difference between the HI radial distributions and the radial distributions of the star light and molecular gas in spiral galaxies has been a topic that has recently received much attention. In this thesis we have demonstrated that the distribution of HI differs quite dramatically from the distributions of H_2, B- and I-band light, and Hα emission in the Scd galaxy NGC 6946. The azimuthally averaged radial profiles of H_2, B, I, and Hα are all centrally peaked and then decrease with radius in the disk (see Chapters 2 and 3). The azimuthally averaged HI distribution, however, is quite flat and extended with a central depression. These same trends in the radial distributions of stars and gas have been found in other late type spiral galaxies (*e.g.* Young and Scoville 1982a, 1982b; Solomon *et al.* 1983; Kenney and Young 1986, 1987). Shaya and Federman (1987) have recently presented an interpretation for the flat HI distributions in galaxies. They suggest that most of the atomic gas in galaxies is contained within constant column density envelopes of molecular clouds. They argue that the mean column density of HI that is observed depends on the amount of UV radiation present and the volume density of the clouds. It has also been suggested in this thesis and elsewhere (Seiden 1983; Tacconi and Young 1986) that the H_2 and HI distributions in galaxies can be understood in terms of a molecular cloud formation

efficiency. In the inner parts of many spiral galaxies where the H_2 surface density dominates that of HI, molecular cloud formation may be proceeding very efficiently, whereas in the outer parts molecular clouds do not seem to be able to form as efficiently, perhaps due to a decrease in the total gas volume density.

In this chapter we discuss the roles of atomic and molecular gas in relation to what is observed in NGC 6946 and the sample of dwarf irregular galaxies. The idea that the $\sigma(H_2)/\sigma(HI)$ ratio is an indicator of the molecular cloud formation efficiency is discussed in Section 6.2. In Section 6.3 we discuss Shaya and Federman's model and show how differences in the gas volume density, the UV dissociation field, the dust-to-gas ratio, metallicity, and IMF may affect the thicknesses of atomic hydrogen envelopes around molecular clouds within a particular galaxy and from galaxy to galaxy. Global properties of the gas and optical luminosity of NGC 6946 and the dwarf irregular galaxies are presented in Section 6.4. A discussion of the possible uncertainties in determining molecular hydrogen masses from CO integrated intensities is given in Section 6.5. In Section 6.6 we analyze the relative amounts of atomic and molecular hydrogen in dwarf irregular galaxies and NGC 6946 in relation to the two possible roles of HI in these galaxies.

6.2 The Role of HI as a Reservoir for Molecular Cloud Formation

In Chapters 2 and 4 we discussed the possibility that the atomic gas in galaxies may be the reservoir from which new molecular clouds will form (see also Tacconi and Young 1986). In this scenario the ratio of the H_2 to HI surface densities is

interpreted as an efficiency of molecular cloud formation. For NGC 6946, we inferred that the sharp decrease in the $\sigma(H_2)/\sigma(HI)$ ratio with radius indicated that molecular cloud formation has proceeded with much greater efficiency in the central regions than in the outer parts of this galaxy. A decrease in the gas volume density due to an increase in the scale height of the HI was suggested to be a likely cause for the decreased cloud formation efficiency in the outer disk. We also suggested that a low gas volume density could explain the small $\sigma(H_2)/\sigma(HI)$ ratios that were observed in the dwarf irregular galaxies (see Chapter 5). In these low mass systems, the molecular cloud formation efficiency could be very low.

Along the same ideas, Seiden (1983) has recently proposed a theory of stochastic self-propagating cloud formation based on a two-component gas model. In this model, atomic hydrogen coalesces into molecular clouds prior to the onset of star formation. After stars form, the molecular clouds are disrupted and much of the material returns to the atomic phase. In this model, cloud formation is regulated since if the molecular cloud formation rate is too high, the HI reservoir will begin to run dry, thereby resulting in a decrease in the cloud formation rate. This type of cloud formation feedback mechanism will continue to operate until gas is returned to the atomic phase after star formation.

6.3 The Role of HI as an H_2 Destruction Product

Shaya and Federman (1987) have analyzed the physical conditions that may be responsible for the flat radial distributions of HI observed in the disks of many spiral

galaxies. Federman, Glassgold, and Kwan (1979) and Hollenbach, Werner, and Salpeter (1971) have calculated the column densities necessary to shield H_2 from the surrounding ultraviolet radiation. Based on these calculations, Shaya and Federman argue that the majority of atomic gas observed in galaxies is located in envelopes around molecular clouds. They suggest that evidence for this model may lie in the fact that the peak values of the HI surface density observed in galaxies is generally 1-2 times the critical column densities for H_2 self-shielding calculated by Federman, Glassgold, and Kwan.

To estimate the amount of HI that is in the envelopes of molecular clouds it is first necessary to understand the process by which the H_2 is dissociated. The dissociation is a two-step process involving the absorption of a UV photon by a molecule in a low rotational level of the ground electronic state giving rise to a Lyman band electronic transition, followed by a decay of the excited state. This process leads to a dissociation about 10% of the time. The theory of Federman, Glassgold, and Kwan suggests that the column densities in the transition region depends only on the ratio G/n, where the quantity G is the integral over frequency of the UV flux times the cross section in the H_2 Lyman lines, and n is the gas volume density. This formulation ignores attenuation of the dissociating radiation. In this picture the column density of the HI envelope surrounding a molecular cloud cannot be greater than the critical column density for self-shielding, since above that all the gas would be molecular. On the other hand, if there is some molecular gas present, the HI column density cannot

be less than that required to shield the molecular gas from dissociation, otherwise the gas would be all atomic. The range of HI surface densities that are associated with clouds that will be observed in a galaxy are therefore determined by the intensity of the radiation field, the gas volume density, the geometry of the cloud envelopes, and the cloud size distribution. Because of the dependence on gas volume density, any low density intercloud gas will not be subject to these constraints.

To put all of the above quantitatively, a cloud becomes a molecular cloud when its radius exceeds the size scale of the HI-H_2 transition layer in that

$$R_{tr} = \frac{N_{tr}}{2\, n_{gas}} \tag{6.1}$$

where R_{tr} is the thickness of the neutral hydrogen transition layer and N_{tr} is the column density of that layer (Federman Glassgold and Kwan 1979 ; Shaya and Federman 1987). As stated before (ignoring the attenuation of the radiation by dust)

$$N_{tr} \propto \left[\frac{G}{n_{gas}}\right]^{1.4}. \tag{6.2}$$

The factor of 2 in Equation 6.1 arises from the fact that two neutral hydrogen atoms are created from the dissociation of one H_2 molecule. Therefore,

$$R_{tr} \propto \frac{G^{1.4}}{n_{gas}^{2.4}} \tag{6.3}$$

which is a very strong function of the gas volume density.

With the above relations between the transition thickness, the UV dissociation field, and the gas density, Shaya and Federman argue that the relatively flat HI distributions observed in spiral galaxies are the results of the HI being largely contained in the molecular cloud envelopes. The clouds are distributed in such a way that the area filling factor across the galaxy is constant and roughly equal to unity when the galaxy is viewed face-on. This is equivalent to having one cloud present in every line of sight passing through the plane of the galaxy.

The H_2-HI transition model is used to explain many recent observations of galaxies. Wevers (1984) has shown that peak HI surface densities are larger for later type galaxies. Shaya and Federman calculate the Hα surface brightnesses from the data of Kennicutt and Kent (1983) assuming that the Hα extends out to D_{25}, and find that Sc galaxies have 20% higher surface brightnesses than Sb galaxies. Assuming that the Hα emission is also a measure of the amount of UV radiation, they estimate that for a constant gas volume density, the increased dissociating flux in Sc galaxies would result in a 30% larger transition column density compared to that in Sb galaxies. Thus, larger HI peak surface densities observed in late type galaxies by Wevers (1984) could be the result of a more intense UV radiation field in these galaxies compared to early type systems. The HI column densities are necessarily larger in late type galaxies to shield the molecular gas from the dissociating radiation.

The thickness of the transition layer is strongly dependent on the gas volume density. Since this quantity is very difficult to measure observationally, it is only

possible to speak in terms of the gas surface densities and to infer the behavior of the scale height of the gas. Radio observations of our galaxy indicate that the HI scale height increases in the outer parts of the galaxy (Jackson and Kellman 1974). Shaya and Federman point out that a decrease in the volume density of the molecular gas with radius due to an increase in the gas scale height will result in an increase in the thicknesses of the HI transition layers around clouds. An increase in the number of totally atomic hydrogen clouds would then be observed. It should be noted, though, that both the theory of Shaya and Federman and the HI reservoir theory predict the same effect for the outer disks of galaxies.

There are subtle effects which may explain some of the differences in the relative amounts of atomic and molecular gas that are observed at particular locations within a galaxy and also from galaxy to galaxy. One effect is the amount of dust present in the clouds which will act to attenuate the dissociating radiation field. Shaya and Federman ignore the attenuation of the UV radiation by dust in their model. Federman, Glassgold, and Kwan (1979) have calculated the effects of dust on the thickness of the HI transition layer around a cloud and find that in most cases including dust attenuation will only affect the transition thickness by 15-20%. They suggest that since the scattering properties of dust are not well determined, particularly for the far-UV region, this small difference is probably not important in most clouds, given the inherent uncertainties. It is expected that a galaxy with a high dust-to-gas ratio would have thinner transition layers surrounding its molecular clouds

than a galaxy with a low dust-to-gas ratio, all else being equal. This effect would be observable as slightly lower peak HI surface densities in very dusty galaxies. Such an effect is observed by Rogstad and Shostak among Scd galaxies. The low luminosity, metal-poor galaxy, M33 has a higher peak HI surface density than the high luminosity, metal-rich galaxies, M101 and NGC 6946.

Another galaxy property that may play a subtle role in determining the transition thickness around molecular clouds is the metallicity of the gas. It is a well known fact that metals are the main coolants for interstellar clouds. In a galaxy with a low metallicity, the gas temperature in a cloud may be higher than the gas temperature in a cloud in a high metallicity galaxy. For the same gas density, the lower metallicity clouds will have a higher Jeans mass, since $M_{Jeans} \sim T^{3/2}/n^{1/2}$. Silk (1986) has posited that in interacting galaxies, a high gas temperature gives rise to large Jeans mass fragments. The higher Jeans mass of the clouds could then give rise to the high rate of massive star formation that is observed in these systems. In a similar fashion, a higher Jeans mass in low metallicity systems may give rise to the formation of more massive stars in these systems than in higher metallicity galaxies. One result of an increase in the number of massive stars would be a corresponding increase in the H_2 dissociating photon production rate, which would, in turn, give rise to thicker HI envelopes around molecular clouds. Thus a correlation is expected between the $\sigma(H_2)/\sigma(HI)$ ratio and the metallicity of the galaxy.

One effect of a higher Jeans mass may be to increase the upper mass cutoff of the initial mass function (IMF). The magnitude of this effect can be estimated by integrating a given IMF with two different upper mass cutoffs. Based on properties of zero-age main sequence O and B stars from Panagia (1973), Waller (1988) has derived a relationship between the mass of a star and its Lyman continuum photon production rate, $N_{Ly}(M)$. We have determined the total Lyman continuum production rate by integrating this production rate over a Miller-Scalo (1979) IMF and assuming that only stars with $M \geq 10\ M_{\odot}$ contributed to the Lyman continuum flux. The IMF was normalized such that

$$\int_{0.1}^{M_u} \Phi(M)\, dM = 1.$$

Using upper mass cutoffs of 50 and 100 $M_{\odot}$, we find that the IMF with the 100 $M_{\odot}$ cutoff will produce 7 times more hydrogen ionizing photons than one with a 50 $M_{\odot}$ cutoff. Since Lyman continuum photons can also dissociate H_2, a galaxy which has an IMF with a 100 $M_{\odot}$ upper mass cutoff will have HI transition layers which are thicker on the average than one with a 50 $M_{\odot}$ cutoff, assuming that they both have the same gas volume density.

6.4 A Comparison of NGC 6946 and Dwarf Irregular Galaxies

It is very important to compare and understand the global properties of the dwarf irregular galaxies that were discussed in Chapter 5 with those those of NGC 6946 in order to better understand the roles of the different phases of the ISM in these two

very different types of systems. Because all the objects that we have studied in this thesis are all at different distances, we wish to compare ratios of quantities, to minimize the distance effects. Table 6.1 list several global ratios for NGC 6946 and the dwarf irregular galaxies in which we have detected CO (see Chapter 5). Typical uncertainties in these ratios are between 10-15% for NGC 6946 and 20-30% for the dwarf galaxies, assuming that the CO-H_2 conversion is constant from galaxy to galaxy. The consequences of a nonconstant conversion will be discussed in the next section.

The global masses and luminosities for the dwarf irregulars and NGC 6946 were calculated as in Chapters 2 and 5. For NGC 6946, we have estimated the total CO luminosity by summing the azimuthally averaged CO integrated intensity distribution over all radii such that

$$L_{CO} = \sum_{l} A_l \langle I_{CO} \rangle_l \cos(i). \qquad (6.3)$$

Here, as in Chapter 3, the CO integrated intensities have been corrected to a T_R^* scale (Kutner and Ulich 1981) by scaling the data by the forward scattering and spillover efficiency (N_{fss}=0.70), and for the elevation dependence of the opacity. Additionally, global 60 and 100 μm fluxes for NGC 6946 were determined from coadded IRAS survey data by the method described in Chapter 5. The total IR luminosity from 40 μm to 300 μm was calculated for each galaxy in Table 6.1 using the 60 and 100 μm flux densities by the method outlined in the IRAS Extragalactic Catalogue (Lonsdale *et al.* 1985).

Table 6.1

Derived Global Properties of NGC 6946 and Dwarf Irregular Galaxies

Galaxy	$\frac{L_{IR}}{L_{CO}}$ [a]	$\frac{L_{IR}}{L_B}$ [b]	$\frac{L_{CO}}{L_B}$ [c]	$\frac{M_{H_2}}{M_{HI}}$ [d]	$\frac{M_{dust}}{M_{ISM}}$ [e,f]	$\frac{M_{H_2}}{M_{ISM}}$ [e]
NGC 6946	2.8	2.2	8.0	1.2	4.0	0.55
LGS-3	<1.1	<0.32	2.7	0.50	---	0.33
IIZw40	56	15	0.31	0.07	9.8	0.07
Mkn 35	39	1.2	2.5	0.14	21	0.12
IZw36	<4.9	<1.2	2.1	0.29	---	0.22
DDO 218	2.2	0.53	2.4	0.24	4.2	0.19

[a] Units of L_{IR} are $L_{\odot}$; units of L_{CO} are K km s^{-1} kpc^2; L_{IR}/L_{CO} ratios are in units of 10^7 L_{IR}/L_{CO}. $M(H_2) = 6\times10^6 L_{CO}$.

[b] L_B from Ables (1971) for NGC 6946; from Christian and Tully (1983), Thuan and Martin (1981), and de Vaucouleurs, de Vaucouleurs, and Buta (1981) for the dwarf irregular galaxies.

[c] Units of L_B are $L_{\odot}$; units of L_{CO} are K km s^{-1} kpc^2; L_{CO}/L_B ratios are in units of 10^{-8} L_{CO}/L_B.

[d] HI masses for the dwarf galaxies from Thuan and Martin (1979, 1981) and from Fisher and Tully (1975).

[e] M_{ISM} is defined as $M_{HI} + M_{H_2}$. M_{dust}/M_{ISM} ratios are given in units of 10^{-4} M_{dust}/M_{ISM}.

[f] Warm dust masses were not computed for LGS-3 or IZw36 because of very uncertain 60 and 100 μm fluxes.

We have also estimated the warm dust masses for NGC 6946 and the dwarf irregular galaxies in Table 6.1 using the far infrared flux densities. From Hildebrand (1983), as outlined in Young *et al.* (1986a), the dust masses can be expressed as

$$M_D = \frac{4\,a\,\rho}{q_\nu}\left[\frac{S_\nu D^2}{B(\nu,T)}\right], \qquad (6.4)$$

where a is the grain size, ρ is the grain density, Q_ν is te grain emissivity, S_ν is the flux density at frequency ν, D is the distance, and $B(\nu, T)$ is the blackbody intensity at frequency ν and temperature T. The grain size, density, and emissivity were taken from Hildebrand (1983). The dust temperatures were derived from the 60 and 100 μm flux densities and assuming a λ^{-1} emissivity law; $B(\nu, T)$ was then evaluated for each galaxy based on these dust temperatures and 100 μm fluxes. The derived warm dust masses are compared with the total ISM mass in Table 6.1.

The far-infrared, blue, and CO luminosities of these galaxies span a wide range of values. When comparing the L_{IR}/L_{CO} ratios, the two active dwarf galaxies IIZw40 and Mkn 35 have the highest values of this ratio. It was pointed out in Chapter 5 that these systems may be presently undergoing intense bursts of star formation, which would result in high IR luminosities when compared with CO. Globally, NGC 6946 does not have a significantly different L_{IR}/L_{CO} ratio than the inactive dwarfs. This result is consistent with what we found in Chapter 5, that the infrared luminosity is linearly proportional to the CO luminosity for all classes of late type galaxies. The scatter that was observed in this relationship may be due in part to galaxies like

IIZw40, which appear to have enhanced present day star formation efficiencies. The high L_{IR}/L_B for IIZw40 relative to the other galaxies in our sample is also consistent with this picture.

The dwarf galaxies appear to be somewhat deficient in CO compared to NGC 6946. This is evident when comparing the L_{CO}/L_B ratios in Table 6.1. For a given blue luminosity, NGC 6946 has at least a factor of 3 more CO than any of the dwarf irregular galaxies. Many previously studied giant irregular galaxies also exhibit CO deficiencies relative to their blue luminosities (*cf.* Elmegreen, Elmegreen, and Morris 1980; Young, Gallagher, and Hunter 1984; Tacconi and Young 1985). The global CO deficiency may be indicative of a deficiency of molecular gas in these galaxies, if the CO-H_2 conversion is a universal constant. We will discuss the uncertainties in the CO-H_2 conversion in the next section.

Assuming a constant conversion between CO intensities and H_2 surface densities, differences in the relative amounts of atomic and molecular gas between NGC 6946 and the dwarf irregular galaxies are evident. Globally, the M_{H_2}/M_{HI} ratio is larger than one only in NGC 6946. We have also compared the total H_2 mass with the ISM mass, defined as $M_{HI} + M_{H_2}$, to estimate the percentage of the ISM which is in the molecular form in each galaxy. NGC 6946 has the highest fraction of its ISM in molecular form of any of the galaxies in the sample. Of the dwarf irregular galaxies, the inactive system, LGS-3, has a significantly larger fraction of its ISM in molecular form than do the other dwarf galaxies. The most extreme galaxy is IIZw40, with less

than 10% of its ISM in molecular gas. This galaxy may have dissociated much of its molecular gas in the present burst of star formation. Dwarf galaxies in general may not have a molecular gas dominated ISM. A predominantly neutral ISM in actively star forming dwarf galaxies is predicted by Shaya and Federman (1987) if these galaxies have higher UV fluxes and/or lower gas volume densities than a luminous spiral galaxy such as NGC 6946.

The actively star forming dwarfs, IIZw40 and Mkn 35, have significantly larger M_{dust}/M_{ISM} ratios than either NGC 6946 or DDO 218. This is somewhat surprising, since dwarf irregular galaxies are known to have very low metallicities; a lower ratio of M_{dust}/M_{ISM} might be expected in the dwarf systems than in NGC 6946. A likely explanation is that an increase in the UV radiation fields will lead to higher dust temperatures in active dwarf galaxies. All of the dust in these systems may be warm dust which was detected by IRAS, while a substantial fraction of the dust mass could be at a lower temperature in NGC 6946 (Smith, Harper and Lowenstein 1984) and DDO 218.

In Table 6.2 we have shown some ISM properties within 45" regions for NGC 6946 and the dwarf irregular galaxies. For comparison with the dwarf irregular galaxies we have taken values of $\sigma(H_2)$, σ(HI), and L_B from the central 45" and from the average value at a radius of 3 arcminutes in the disk of NGC 6946. With the exception of IZw36, 45" resolution HI data are not presently available for the dwarf irregular galaxies. To estimate HI surface densities in the central 45" of these

Table 6.2

ISM Properties in 45" Regions

Galaxy	Position	$\frac{\sigma(H_2)}{\sigma(HI)}$	$\frac{\sigma(H_2)}{\sigma(ISM)}$	$\frac{M_{HI}}{L_B}\left[\frac{M_\odot}{L_\odot}\right]$	$\frac{M_{H_2}}{L_B}\left[\frac{M_\odot}{L_\odot}\right]$	$\frac{M_{ISM}}{L_B}\left[\frac{M_\odot}{L_\odot}\right]$
NGC 6946	Center	94	0.99	0.02	1.75	1.77
NGC 6946	Disk (R=3:00)	1.5	0.60	0.36	0.51	0.87
LGS-3		10	0.90	0.10	1.19	1.29
IIZw40		0.05	0.05	0.47	0.25	0.72
Mkn 35		2.5	0.71	0.02	0.11	0.13
IZw36		0.53	0.35	0.08	0.28	0.36
DDO 218		4.4	0.81	0.10	0.89	0.99

systems, we have assumed that the HI distributions are flat and that the HI extends over a region $3 \times D_{25}$ across. These assumptions are reasonable to within a factor of 2 in light of the 30" resolution HI observations of IZw36 (Viallefond and Thuan 1983, see below). High resolution HI observations are urgently needed to place better constraints on the relative amounts of atomic and molecular gas present in these objects.

From Table 6.2 it is evident that the H_2/HI surface density ratios are significantly higher in the center of NGC 6946 than in any of the dwarf galaxies. Nearly all of the gas present in the center of this galaxy is in molecular form. The central 45" of LGS-3 also appears to be rich in molecular gas. The disk position of NGC 6946 has a $\sigma(H_2)/\sigma(HI)$ ratio which is more similar to those of the majority of the dwarf galaxies. Within the uncertainties, the H_2 and HI surface densities appear to be roughly comparable in Mkn 35, IZw36, and DDO 218. The ISM of IIZw40 is unlike that of any regions of NGC 6946. With a $\sigma(H_2)/\sigma(HI)$ ratio of <0.1, it is the most H_2 deficient galaxy of the sample (see also Chapter 5). ISM mass-to-blue light ratios for the same 45" regions in the sample galaxies show similar trends. For example, the center of NGC 6946 and LGS-3 have the largest values of M_{H_2}/L_B, while having small M_{HI}/L_B ratios. If the true HI distributions are somewhat peaked, as they are in the 30" resolution observations of IZw36 (Viallefond and Thuan 1983) rather than being flat as we have assumed, the central 45" HI mass-to-light ratios could be much larger. We estimate that there could be a factor of 2 difference between the HI mass-

to-light ratios as quoted in Table 6.2 and their values if the HI distributions were centrally peaked.

6.5 Uncertainties in the I_{CO} to $\sigma(H_2)$ Conversion Factor

Before suggesting possible explanations for the differences seen in the relative amounts of atomic and molecular gas in NGC 6946 and the 5 dwarf irregular galaxies, we must discuss the problems in applying the Galactic CO integrated intensity to H_2 surface density conversion to other galaxies. If the molecular cloud properties of other galaxies are very different from those of our own, the use of a Galactic conversion may lead to serious misconceptions about the molecular gas distribution and abundance in these systems. The problems may be particularly troublesome in the dwarf irregular galaxies, where metallicities could affect the CO abundance.

The correlation between CO integrated intensities and H_2 column densities has been derived empirically and theoretically for our Galaxy, with agreement to within a factor of two among the various studies. Theoretically, Dickman, Snell, and Schloerb (1986) have related CO integrated intensity to the mass surface density for an ensemble of clouds. There are two basic assumptions implicit to the derivation: (1) the molecular clouds are virialized and (2) the CO line profile can be treated as a superposition of independent, spatially averaged molecular cloud profiles. The global CO integrated intensity formed by the ensemble average is then

$$\langle I_{CO} \rangle = \frac{N_c \pi T}{4 A_B} \langle l^2 \Delta V \rangle, \tag{6.5}$$

where N_c is the number of clouds subtended by the telescope beam, A_B is the beam area, T is the mean radiation temperature of the clouds, l is the cloud diameter, and is the mean velocity dispersion of each cloud measured at half power. In a similar fashion, Dickman, Snell, and Schloerb relate the mass surface density to the mean cloud properties such that

$$\langle \sigma \rangle = \frac{N_c \pi}{6 A_B} \langle l^3 \rho \rangle, \tag{6.6}$$

where ρ is the average cloud density. Assuming the clouds are virialized yields

$$b = \frac{\langle I_{CO} \rangle}{\langle \sigma \rangle} = C T \frac{\langle l^3 \rho^{1/2} \rangle}{\langle l^3 \rho \rangle}, \tag{6.7}$$

where C is a constant. Assuming a size-linewidth relationship and a power law distribution for the cloud sizes (Sanders *et al.* 1985; Larson 1981), and a mean cloud radiation temperature of $T_R = 10$ K, Dickman, Snell, and Schloerb find that b = $2.4 \pm 0.1 \times 10^{20}$ H_2 cm^{-2} (K km s^{-1})$^{-1}$.

The results of many empirical studies have also yielded a linear relationship between CO integrated intensities and H_2 column densities in our Galaxy. Based on visual extinction and ^{12}CO measurements for dark clouds and a virial theorem analysis for giant molecular clouds, Young and Scoville (1982a) have derived a conversion factor of $4 \pm 2 \times 10^{20}$ H_2 cm^{-2} (K km s^{-1})$^{-1}$. From their survey of the inner galaxy, Sanders, Solomon, and Scoville (1984) find a value for the conversion factor

of $3.6\pm1 \times 10^{20}$ H_2 cm^{-2} (K km $s^{-1})^{-1}$ by taking mean ^{12}CO to ^{13}CO ratios, and from visual extinction measurements and virial theorem cloud masses. More recently, Bloemen *et al.* (1986) have compared the distribution of γ-rays and CO emission in the Galaxy and find a linear conversion factor of 2.8×10^{20} H_2 cm^{-2} (K km $s^{-1})^{-1}$ between radii of 2 and 15 kpc. Based on the Massachusetts-Stonybrook Galactic plane CO survey, and assuming virial theorem cloud masses, Scoville *et al* (1987) and Solomon *et al.* (1987) have independently determined mean values for the CO-H_2 conversion factor of 3.6×10^{20} H_2 cm^{-2} (K km $s^{-1})^{-1}$ and 3.0×10^{20} H_2 cm^{-2} (K km $s^{-1})^{-1}$, respectively.

There is agreement to within a factor of two among all of the above CO integrated intensity to H_2 surface density conversion factors discussed above. The use of one of the Galactic conversion factors should therefore yield reliable H_2 surface density estimates for those cloud ensembles in our Galaxy, and possibly the disks of spiral galaxies, where cloud properties may be similar to those of the Milky Way clouds. However, there are regions within other galaxies where there may be reason to doubt H_2 masses obtained with a Galactic conversion factor. One parameter which may affect the CO integrated intensities is the radiation temperature of the clouds. Dickman, Snell, and Schloerb (1986) assumed a mean radiation temperature of 10 K in their analysis. If there are regions in a galaxy where this is not the case, such as areas of high star formation efficiency, the use of a Galactic CO-H_2 conversion factor

will result in overestimates of the H_2 mass in these regions. Higher radiation temperatures might also be expected in centers of luminous spiral galaxies.

Use of a Galactic CO-H_2 conversion factor in metal-poor galaxies may also yield erroneous H_2 masses since the CO abundance relative to H_2 will almost certainly be different from that in the Milky Way. We have addressed this issue previously, in Chapter 5, but justified the use of the Bloemen *et al.* (1986) conversion factor since we were comparing the molecular gas properties of all metal-poor systems. Israel *et al.* (1986) have made numerous observations of ^{12}CO in the Large and Small Magellanic Clouds, and have found the CO emission from these galaxies tends to be weaker than that from Galactic clouds. They propose that low metallicities can explain the weak CO emission seen in many irregular galaxies (*e.g.* Elmegreen, Elmegreen, and Morris 1980; Young, Gallagher, and Hunter 1984; Tacconi and Young 1985; Thronson and Bally 1987; Chapter 5).

Even though an underabundance of CO may not affect the ^{12}CO intensity significantly, since the ^{12}CO low J level transitions are optically thick, a low metallicity may have a much more subtle effect. First, the dust-to-atomic gas ratios are much lower in the LMC and SMC than in the Galaxy (Koornneef 1982; Lequeux *et al.* 1984). Secondly, peak UV energy densities in several regions in both Magellanic Clouds are about an order of magnitude higher than the mean Galactic value (*e.g.* Morgan, Nandy, and Carnochan 1979). Since CO is dissociated by UV radiation shortward of 1120 Angstroms, Israel *et al.* suggest that the effects of a low

dust-to-gas ratio combined with a strong UV flux can explain weak CO emission in actively star forming irregular galaxies such as the Magellanic Clouds by providing less shielding and higher dissociation rates for the CO molecules.

Israel *et al.* also propose that high rates and efficiencies of massive star formation may be prevalent in irregular galaxies, resulting in destruction of molecular cloud complexes. It is possible, then, for molecular clouds to have much shorter lifetimes than those in our Galaxy. Israel *et al.* note that this explanation can account for the lack of CO emission that they observed towards the 30 Doradus complex.

Recently, Cohen *et al.* (1987) have completed a ^{12}CO survey of molecular clouds in the LMC at an angular resolution of 8'.8, corresponding to a linear resolution of ~140 pc at the distance of the LMC. They identify 40 molecular clouds in this galaxy, and look for a correlation between CO intensity and linewidth for these clouds. For a given linewidth, the LMC molecular clouds are found to be a factor of 6 fainter in CO. Alternatively, this result can be expressed as the CO linewidths being too large for a given CO luminosity. Cohen *et al.* suggest that in attempting to estimate H_2 masses from CO integrated intensities in metal-poor irregular galaxies it is more appropriate to apply a CO-H_2 conversion factor of ~6 $\times$ the Galactic conversion.

There is evidence, however, that Cohen *et al.*'s finding of a larger CO-H_2 conversion factor may be in error. Observations of M33 made with the FCRAO 14-meter telescope with roughly the same linear resolution (140 pc) as the 8'.8 Columbia observations of the Magellanic Clouds, indicate a CO luminosity-linewidth

relationship which differs from the galactic one. However, using CO observations made with the Owens Valley interferometer, with ~5 times better resolution, Wilson and Scoville (private communication) find a much smaller linewidth for individual clouds than the linewidth in a 140 pc region. This suggests that galactic rotation or random motions among clouds cause the linewidth measured over 140 pc to be much larger than for an individual cloud, and ascribing the CO linewidths observed in the LMC to individual clouds is misleading. The only proper way to address the question of the CO luminosity-linewidth relationship in other galaxies is with observations which resolve individual clouds.

6.6 The Roles of Molecular and Atomic Hydrogen

Two scenarios were presented in Sections 6.2 and 6.3 which described the possible roles that the atomic gas plays in the star formation process in a galaxy: that of a reservoir from which molecular clouds will form (hereafter, Picture 1) and that of a destruction product of star formation (hereafter, Picture 2). Based on the current knowledge of the atomic and molecular distributions in galaxies, it is impossible to discern which scenario is the correct one, and in all likelihood they may both play a role in determining the relative amounts of atomic and molecular gas. We now wish to discuss these two pictures in relation to the $\sigma(H_2)/\sigma(HI)$ ratios that we have derived from observations of NGC 6946 and the sample of dwarf irregular galaxies.

In NGC 6946, we have inferred that the radial distribution of H_2 is centrally peaked and then falls off monotonically with radius. The HI distribution, on the other

hand, is characterized by a central depression, a peak at around 8 kpc from the center and a slow monotonic decrease with radius from there. In Picture 1, this distribution is explained by high cloud formation efficiency in the center of the galaxy, and a decrease in the cloud formation efficiency with radius. If the scale height of the gas is increasing with radius, a decrease in the cloud formation efficiency can be understood in terms of a corresponding decrease in the gas volume density.

In the Shaya and Federman (1987) picture (Picture 2) the flatness of the observed HI distribution relative to H_2 is explained by the HI being contained largely in constant column density envelopes around molecular clouds. Very little variation in the HI surface densities is seen because once the critical column density is achieved, the atomic gas will become molecular. It is known that the Hα radial distribution, as well as the H_2 distribution, is centrally peaked. Since an increase in the Hα flux presumably implies an increase in the UV radiation field, an HI central hole and an H_2 peak can only be explained in the Shaya and Federman picture if very dense clouds are present (see Equation 6.3). In NGC 6946, typical clouds would have to be ~10 times denser in the central 2 kpc of this galaxy than at a radius of 6.5 kpc to account for the HI hole and Hα flux that is observed. The slow decrease in the HI surface densities with radius can be attributed to a possible radial decrease in the gas volume density in this picture. A decrease in the gas density will result in an increase in the thickness of the transition layer, and therefore an increase in the number of totally

atomic clouds observed. This could explain why HI dominates the H_2 gas in the outer disk of NGC 6946.

One problem in interpreting the HI and H_2 distributions in relation to either picture is that the H_2 surface densities could be overestimated in the central regions of NGC 6946 due to a higher gas radiation temperature. Dickman, Snell, and Schloerb (1986) have derived a linear dependence of the CO intensity, and therefore the H_2 surface density, on the radiation temperature of the gas. The gas temperatures would have to be an order of magnitude higher, however, to change our conclusion that H_2 is the dominant component of the ISM in NGC 6946.

When comparing the dwarf irregular galaxies with NGC 6946, we found that NGC 6946 and the inactive dwarf galaxy LGS-3 had globally much larger fractions of their ISM in molecular form than did the actively star forming dwarf galaxies. If the H_2 masses have been underestimated because of the low metallicities in the dwarf galaxies (see previous section), then the above statement may not hold, and one would be lead to the possible conclusion that the ISM mass fractions are the same in the dwarf irregular galaxies and in NGC 6946, and that the dwarf irregular galaxies are just scaled down versions of their luminous, massive cousin. If we have underestimated the H_2 masses by a factor of 6 as suggested by Cohen *et al.* (1987) for the LMC, then LGS-3 would have H_2/HI ratios comparable to that of NGC 6946. However, even a factor of 6 underestimate in the H_2 mass could not account for the difference in the H_2/HI ratios between NGC 6946 and IIZw40. Moreover, the CO-H_2

conversion factor of Cohen *et al.* (1987) is probably artificially high. We are thus led to the conclusion that the differences in the observed H_2/HI ratios between NGC 6946 and at least the actively star forming dwarf galaxies, such as IIZw40 and giant irregular galaxies, such as NGC 1569 (Young, Gallagher and Hunter 1984), are real.

We suggest that the observed differences between the active dwarf irregulars and NGC 6946 can most easily be explained by the Shaya and Federman picture. In the metal-poor systems the gas might not be able to cool itself very efficiently. The resulting higher gas temperature will give rise to a larger Jeans mass, which could in turn result in a higher rate of massive star formation. When a metal-poor galaxy does form stars, it may form stars with a higher upper mass cutoff in the IMF or with an IMF that is weighted toward more massive stars. An increase in the UV radiation field of the metal-poor galaxy relative to that of the metal-rich galaxy would then follow. In fact, this effect has been observed in the Large and Small Magellanic Clouds. Morgan, Nandy, and Carnochan (1979) observe peak UV energy densities in several regions of the Clouds which are about an order of magnitude higher than the mean Galactic value. The increase in the UV field will give rise to thicker HI transition layers in metal poor galaxies, such as IIZw40, than those found in metal-rich systems, such as NGC 6946. The effect is not present in an inactive dwarf galaxy, like LGS-3, because no recent star formation has occurred in this galaxy. If star formation does commence in this galaxy in the future, it is quite possible that it would show evidence for thick HI transition layers.

Another explanation for the differences in the ISM mass fractions inferred in NGC 6946 and the dwarf irregular galaxies is that the gas volume densities may be lower in the dwarf systems. Since dwarf irregular galaxies have lower mass densities than spirals, they presumably also have larger gas scale heights, and thus lower volume densities. In Picture 2, lower gas volume densities in the dwarf galaxies relative to those in NGC 6946 would lead to thicker transition layers in these systems, *i.e.* more HI and less H_2.

To better address the possible differences between spiral and dwarf irregular galaxies, many more observations are needed. High resolution HI observations of dwarf galaxies are warranted to determine the true distribution of the atomic gas in the regions where CO is observed. Better statistics are needed for the dwarf irregular galaxies. Furthermore, a molecular cloud size-linewidth analysis in irregular galaxies at high spatial resolution would be very valuable to determine whether CO can be used reliably as a tracer of molecular hydrogen in low metallicity irregular galaxies.

CHAPTER 7

SUMMARY

In this thesis we have looked at the distributions of the atomic and molecular components of the ISM in NGC 6946 and a sample of dwarf irregular galaxies with the hope of gaining insight into the role that each component plays in the star formation process. In Chapters 2-4 we presented a study of the detailed distributions of both the molecular and atomic components of the ISM in NGC 6946, which were obtained with similar resolution. Chapter 5 dealt with the properties of atomic and molecular gas in dwarf irregular galaxies. In Chapter 6, two scenarios for the role of HI in the star formation history of a galaxy were discussed; these pictures were related to the atomic and molecular gas contents of NGC 6946 and the dwarf irregular galaxies. The main results of this thesis are summarized below.

Global properties of NGC 6946 and a complete 40" HI map of this galaxy were presented in Chapter 2, and a fully sampled ^{12}CO map of the inner 6'.75 of NGC 6946 was presented in Chapter 3. Detectable HI emission was observed out to a radius of 30 kpc, roughly twice D_{25}. The HI emission exhibits several clumpy structures larger than 2 kpc across, with evidence for HI spiral structure in the outer disk. The HI map shows the presence of a large central depression with several other resolvable HI depressions to the north and southwest of the center. The CO integrated intensities are very strongly peaked in the center of NGC 6946, with smaller peaks evident to the

northeast and southwest of the center. These smaller peaks lie in the direction of optical spiral arms.

We have compared the azimuthally averaged radial distributions of CO and HI with B- and I-band, Hα, and radio continuum profiles in the literature. All of the radial distributions, except HI, are centrally peaked and then decrease monotonically with radius. The HI distribution has a central depression, a peak at a radius of ~ 8 kpc, and then a very shallow monotonic decrease with radius. We infer from this that the atomic gas component may play only a passive role in the evolution of high luminosity, late-type spiral galaxies such as NGC 6946.

In Chapter 4, we presented comparisons of H_2 and HI surface densities, and B, I, and Hα surface brightnesses in the same 45" regions. Globally, the H_2 and HI surface densities do not appear to be correlated. When comparing the H_2 and HI surface densities with the optical surface brightnesses, there is a good correlation between the H_2 surface densities and the Hα, B, and I surface brightnesses, while the HI surface densities show no correlation with the optical components. From these results, we suggest that the star formation efficiency has remained roughly constant on 2 kpc scales over the past several billion years. We infer that the $\mu(H\alpha)/\sigma(H_2)$ ratio is a measure of the massive star formation efficiency. Averaging over azimuthal structures, the $\mu(H\alpha)/\sigma(H_2)$ ratio is roughly constant with radius, indicating that the massive star formation efficiency is constant with radius. On the other hand, the

$\sigma(H_2)/\sigma(HI)$ ratio decreases steeply with radius. One interpretation of this is that there is a radial decrease in the molecular cloud formation efficiency. An alternative interpretation is that the HI is a destruction product of H_2, and is largely found in the envelopes of molecular clouds (Shaya and Federman 1987).

Azimuthal profiles of the H_2 and HI surface densities, and Hα, B and I surface brightnesses were also presented in Chapter 4. In regions of well defined spiral structure in the northeast, we find enhancements in the H_2 surface densities, Hα surface brightnesses, and $\mu(H\alpha)/\sigma(H_2)$ and $\sigma(H_2)/\sigma(HI)$ ratios of the spiral arms. In the southwest where the spiral structure is poorly defined, enhancements in the H_2 surface density on the arms are not followed in some instances by enhancements in the Hα flux or the $\mu(H\alpha)/\sigma(H_2)$ ratio. At a given radius the arm-interarm contrasts are much greater in the Hα surface brightness and $\mu(H\alpha)/\sigma(H_2)$ ratios than in the H_2 surface density. We infer that the massive star formation efficiency is greater in the spiral arms than in the interarm regions of NGC 6946. The large increase in massive star formation efficiency and slightly increased H_2 surface densities in the spiral arms, and the presence of small peaks in the H_2 and HI surface densities in the interarm regions are all consistent with a picture in which cloud-cloud collisions play an important role in the star formation process in NGC 6946.

Radial increases in the spiral arm amplitudes, as derived from B- and I-band spiral arms, are evident. Correspondingly, large radial increases in the arm-interarm

contrasts in the Hα surface brightness and massive star formation efficiency are also prominent, with smaller increases observed in the H_2 surface density contrasts. We suggest that the massive star formation efficiency is a sensitive function of the spiral arm strength.

A study of the CO contents of 15 dwarf irregular galaxies chosen to span a wide range in color and star formation activity was presented in Chapter 5; CO was detected in 6 of the objects. We have compared the CO luminosities of the dwarfs with their far-infrared luminosities as determined from IRAS 60 and 100 μm fluxes, and find that the dwarf galaxies extend by three orders of magnitude in luminosity the correlation between IR and CO luminosities found for spiral galaxies alone (Young *et al.* 1986a). The IR luminosity is proportional to the first power of the CO luminosity for all classes of late type galaxies, although we do find a fair amount of scatter in the relationship.

For the dwarf galaxy sample alone, the lowest L_{IR}/L_{CO} ratios are found in those galaxies with the least evidence for ongoing star formation, while the active blue dwarfs have the highest value of this ratio. We interpret this as evidence for depleted or dissociated molecular reservoirs in the blue galaxies which have already experienced burst of star formation, and a build up of molecular gas in the pre-burst, red dwarfs. From their high L_{IR}/L_{CO} ratios we also suggest that the blue dwarf

galaxies may be forming stars as efficiently as the IR luminous galaxies Arp 220 and NGC 6240.

In Chapter 6 we suggested that the observed differences in the H_2/HI mass ratios found between the dwarf irregular galaxies and NGC 6946 can be understood in terms of a scenario where HI is a destruction product of H_2. In this picture, low gas volume densities combined with low metallicities in the dwarf galaxies would combine to yield thick transition layers in actively star forming dwarf systems. The higher metallicity gas clouds in NGC 6946 may produce a smaller fraction of massive stars and resulting in a less intense UV dissociation field in this galaxy than in the dwarf systems. A smaller UV field combined with higher gas volume densities may result in thinner transition layers of HI in NGC 6946 than in actively star forming dwarf galaxies.

BIBLIOGRAPHY

Ables, H.D. 1971, *Publ. U.S. Naval Obs.*,**vol. 20**.

Arp, H.C. 1966, *Ap.J. Suppl.*, **14**, 1.

Athanassoula, E. (ed.) 1983, *IAU Symposium 100, Internal Kinematics and Dynamics of Galaxies*, (Dordrecht: Reidel).

Ball, R., Sargent, A.I., Scoville, N.Z., Lo, K.Y., and Scott, S.L. 1985, *Ap.J. (Lett.)*, **298**, L21.

Bloemen J.B.G.L *et al.* 1986, *Astr. Ap.*, **238**, 148.

Bohlin, R.C., Savage, B.D., and Drake, J.F. 1978, *Ap.J.*, **224**, 132.

Bonnarel, F., Boulesteix, J., and Marcelin, M. 1986, *Astr. Ap. Suppl.*, **66**, 149.

Boroson, T.A., Strom, K.M., and Strom, S.E. 1983, *Ap.J.*, **274**, 39.

Bosma, A. 1978, Ph.D. Dissertation (University of Groningen).

_____. 1981a, *A.J.*, **86**, 1791.

_____. 1981b, *A.J.*, **86**, 1825.

Christian, C.A. and Tully, R.B. 1983, *A.J.*,**88**, 934.

Clark, B.G. 1980, *Astr. Ap.*, **89**, 377.

Cohen, R.S., Dame, T.M., Garay, G., Montani, J., Rubio, M., and Thaddeus, P. 1987, *Ap.J. Lett.*, submitted.

Condon, J.J., Condon, M.A., Gisler, G., and Puschell, J.J. 1982, *Ap.J.*, **252**, 102.

DeGioia-Eastwood, K., Grasdalen, G.L., Strom, S.E., and Strom, K.M. 1984, *Ap.J.*, **278**, 564.

deVaucouleurs, G. 1979, *Ap.J.*, **227**, 380.

deVaucouleurs, G., deVaucouleurs, A., and Buta, R. 1981, *A.J.*, **86**, 1429.

deVaucouleurs, G., deVaucouleurs, A., and Corwin, H.G. 1976, *Second Reference Catalogue of Bright Galaxies* (Austin: University of Texas Press).

Dickman, R.L., Snell, R., and Schloerb, F.P. 1986, *Ap.J.*, **309**, 326.

Dressel, L.L. and Condon, J.J. 1976, *Ap.J. Suppl.*, **31**, 187.

Ekers, R. 1981 in *The Structure and Evolution of Normal Galaxies*, ed. S.M. Fall and D. Lynden-Bell (New York: Cambridge University Press), p.169.

Elmegreen, B.G. 1988, to be published in "Comets to Cosmology", ed. A. Lawrence, Springer-Verlag.

Elmegreen, D.M. and Elmegreen, B.G. 1984, *Ap.J. Suppl.*, **54**, 127.

Elmegreen, B.G., Elmegreen, D.M., and Morris, M. 1980, *Ap.J.*, **240**, 455.

Federman, S.R., Glassgold, A.E., and Kwan, J. 1979, *Ap.J.*, **227**, 466.

Fisher, J.R. and Tully, R.B. 1975, *Astr. Ap.*, **44**, 151.

_____. 1979, *Astr. Ap.*, **84**, 62.

French, H.B. 1980, *Ap.J.*, **240**, 41.

Georgelin, Y.M. and Georgelin, Y.P. 1976, *Astr. Ap.*, **49**, 57.

Gerola, H. and Seiden, P.E. 1978, *Ap.J.*, **223**, 129.

Gerola, H., Seiden, P.E., and Schulman, L.S. 1980, *Ap.J.*, **242**, 517.

Gordon, D. and Gottesman, S.T. 1981, *A.J.*, **86**, 161.

Henkel, C., Wouterloot, J.G.A., and Bally, J. 1986, *Astr. Ap.*, **155**, 193.

Hildebrand, R.H. 1983, *Q.J.R.A.S.*, **24**, 267.

Hodge, P.W. 1969, *Ap.J. Suppl.*, **157**, 73.

Hodge, P and Kennicutt, R. 1983, *A.J.*, **88**, 296.

Hollenbach, D.J., Werner, M.W., and Salpeter, E.E. 1971, *Ap.J.*, **163**, 165.

Huchra, J.P. 1977, *Ap.J.*, **217**, 928.

Hunter, D.A. 1982, *Ap.J.*, **260**, 81.

Hunter, D.A. and Gallagher, J.S. III 1985, *Ap.J. Suppl.*, **58**, 533.

Hunter, D.A., Gallagher, J.S. III, and Rautenkranz, D. 1982, *Ap.J. Suppl.*, **49**, 53.

Israel, F.P. and Burton, W.B. 1986, *Astr. Ap.*, **168**, 369.

Israel, F.P., de Graauw, T., van de Stadt, H, and de Vries, C.P. 1986, *Ap.J.*, **303**, 186.

Israel, F.P. and Rowan-Robinson, M. 1984, *Ap.J* , **283**, 81.

Jackson, P.D. and Kellman, S.A. 1974, *Ap.J.*, **190**, 53.

Jacoby, G.H., Ford, H., and Ciardullo, R. 1985 *Ap.J.*, **290**, 136.

Joy, M. 1986, Ph.D. Dissertation (University of Texas).

Karachentseva, V.E., Schmidt, R. and Richter, G.M. 1984, *Astr. Nachr.*, **305**, 59.

Kenney, J.D. 1987, Ph.D. Dissertation (University of Massachusetts).

Kenney, J.D. and Young, J.S. 1986, *Ap.J. Lett.*, **301**, L13.

_____. 1987, *Ap.J.*, submitted.

Kennicutt, R.C. and Kent, S.M. 1983, *A.J.*, **88**, 1094.

Klein, U., Beck, R., Buczilowski, U.R., and Wielebinski, R. 1982, *Astr. Ap.*, **108**, 176.

Klein, U., Wielebinski, R., and Thuan, T.X. 1984, *Astr. Ap.*, **141**, 241.

Koornneef, J. 1982, *Astr. Ap.*, **107**, 247.

Kraan-Kortweg, R. and Tammann, G. 1979, *Astr. Nach.*, **300**, 181.

Kulkarni, S.R., Blitz, L., and Heiles, C. 1982, *Ap.J. (Lett.)*, **259**, L63.

Kutner, M.L. and Ulich, B.L. 1981, *Ap.J.*, **250**, 341.

Kwan, J. and Valdes, F. 1983, *Ap.J.*, **271**, 604.

_____. 1987, *Ap.J.*, **315**, 92.

Larson, R.B. 1981, *M.N.R.A.S.*, **194**, 809.

Lequeux, J. 1971, *Astr. Ap.*, **15**, 42.

Lequeux, J., Maurice, E., Prévot, C., Prévot-Burnichon, M.-L., and Rocca-Volmerange, B. in *IAU Symposium 108, Structure and Evolution of the Magellanic Clouds*, eds. S. van den Bergh and K.S. de Boer (Dordrecht: Reidel), p. 405.

Lin, C.C. and Shu, F.H. 1964, *Ap.J.*, **140**, 646.

Lo, K.Y., Ball, R., Masson, C.R., Phillips, T.G., Scott, S., and Woody, D.P. 1987, *Ap.J. (Lett.)*, **317**, L63.

Lo, K.Y., Berge, G.L., Claussen, M.J., Heiligman, G.M., Leighton, C.R., Masson, C.R., Moffet, A.T., Phillips, T.G., Sargent, A.I., Scott, S.L., Wannier, P.G., and Woody, D.P. 1984, *Ap.J. (Lett.)*, **282**, L59.

Lonsdale, C.J., Helou, G., Good, J.C., and Rice, W.L. 1985, *"Catalogued Galaxies and Quasars Observed in the IRAS Survey"*, JPL preprint.

Lord, S.D. 1987, Ph.D. Dissertation (University of Massachusetts).

Lord, S.D. and Young, J.S. 1987, in preparation.

McCall, M.L. 1982, Ph.D Dissertation (University of Texas).

Mihalas, D. and Binney, J. 1981, *Galactic Astronomy* (San Francisco: W.H. Freeman and Company), pages 184-192.

Miller, G.E. and Scalo, J.M. 1979, *Ap.J. Suppl.*, **41**, 513.

Morgan, D.H., Nandy, K., and Carnochan, D.J. 1979, *M.N.R.A.S.*, **186**, 421.

Morris, M. and Lo, K.Y. 1978, *Ap.J.*, **223**, 803.

Morris, M. and Rickard, L.J. 1982, *Ann. Rev. Astr. Ap.*, **20**, 517.

Pagel, B.E.J. and Edmunds, M.G. 1981, *Ann. Rev. Astr. Ap.*, **19**, 77.

Panagia, N. 1973, *A.J.*, **78**, 929.

Peimbert, M and Jugaku, J (eds.) 1987, *IAU Symposium 115, Star Forming Regions* (Dordrecht: Reidel).

Rickard, L.J. and Palmer, P. 1981, *Astr. Ap. (Lett.)*, **102**, L13.

Rickard, L.J., Palmer, P., Morris, M., Zuckerman, B., and Turner, B. 1977, *Ap.J.*, **213**, 673.

Roberts, W.W. Jr., Roberts, M.S., and Shu, F.H. 1975, *Ap.J.*, **196**, 381.

Rogstad, D.H. and Shostak, G.S. 1972, *Ap.J.*, **176**, 315.

Rogstad, D.H., Shostak, G.S., and Rots, A.H. 1973, *Astr. Ap.*, **22**, 111.

Rowan-Robinson, M., Phillips, T.G., and White, G. 1980, *Astr. Ap.*, **82**, 381.

Rydbeck, G., Hjalmarsen, A., and Rydbeck, O.E.H. 1985, *Astr. Ap.*, **144**, 282.

Sanders, D.B., Scoville, N.Z., and Solomon, P.M. 1985, *Ap.J.*, **289**, 373.

Sanders, D.B., Scoville, N.Z., Young, J.S., Soifer, B.T., Schloerb, F.P., Rice, W., and Danielson, E. 1986, *Ap.J. (Lett.)*, **305**, L45.

Sanders, D.B., Solomon, P.M., and Scoville, N.Z. 1984, *Ap.J.*, **276**, 182.

Sargent, W.L.W., Sancisi, R., and Lo, K.Y. 1983, *Ap.J.*, **179**, 427.

Schild, R. 1980, *Ap.J.*, **242**, 63.

Schmidt, M. 1959, *Ap.J*, **129**, 243.

Schweizer, F. 1976, *Ap.J. Suppl.*, **31**, 313.

Scoville, N.Z. and Hersh, K. 1979, *Ap.J.*, **229**, 578.

Scoville, N.Z., Sanders, D.B., and Clemens, D.P. 1986, *Ap.J. (Lett.)*, **310**, L77.

Scoville, N.Z. and Young, J.S. 1983, *Ap.J.*, **265**, 148.

Scoville, N.Z., Yun, M.S., Clemens, D.P., Sanders, D.B., and Waller, W.H. 1987, *Ap.J. Suppl.*, **63**, 821.

Searle, L., Sargent, W.L.W., and Bagnuolo, W. 1973, *Ap.J.*, **179**, 427.

Seiden, P.E. 1983, *Ap.J.*, **266**, 555.

Shaya, E.J. and Federman, S.R. 1987, *Ap.J.*, **319**, 76.

Silk, J. 1986, in *IAU Symposium 116, Luminous Stars and Associations in Galaxies*, eds. C.W.H. De Loore, A.J. Willis, and P. Laskarides (Dordrecht: Reidel).

Smith, J., Harper, D.A., and Lowenstein, R.F. 1984, *Airborn Astronomy Symposium Proceedings*, NASA Conference Publication 2353, p.277.

Sofue, Y., Nakai, N., and Handa, T. 1987, *Publ. Astron. Soc. Japan*, **39**, 47.

Solomon, P.M., Barrett, J., Sanders, D.B., and de Zafra, R. 1983, *Ap.J. (Lett.)*, **266**, L103.

Solomon, P.M., Rivolo, A.R., Barrett, J., and Yahil, A. 1987, *Ap.J.*, **319**, 730.

Solomon, P.M., Sanders, D.B., and Rivolo, A.R. 1985, *Ap.J. (Lett.)*, **292**, L19.

Stark, A.A. 1979, Ph.D. Dissertation (Princeton University).

Stark, A.A., Elmegreen, B.G., and Chance, D. 1987, *Ap.J.*, **322**, 64.

Tacconi, L.J. and Young, J.S. 1985, *Ap.J.*, **290**, 602.

_____. 1986, *Ap.J.*, **308**, 600.

Telesco, C.M. and Harper, D.A. 1980, *Ap.J.*, **235**, 392.

Thronson, H.A. and Bally, J. 1987, in *Star Formation in Galaxies*, NASA Conference Publication 2466, page 267.

Thronson, H.A. Jr. and Telesco, C.M. 1986, *Ap.J.*, **311**, 98.

Thronson, H.A. Jr., Hunter, D.A., Telesco, C.M., Harper, D.A., and Decher, R. 1987, *Ap.J.*, 317, 180.

Thuan, T.X. 1983, *Ap.J.*, **268**, 667.

Thuan, T.X. and Martin, G.E. 1979, *Ap.J.(Lett.)*, **232**, L11.

_____. 1981, *Ap.J.*, **247**, 823.

Thuan, T.X. and Seitzer, P.O. 1979, *Ap.J.*, **231**, 680.

van der Kruit, P.C. and Allen, R.J. 1978, *Ann. Rev. Astr. Ap.*, **16**, 103.

van der Kruit, P.C., Allen, R.J., and Rots, A.H. 1977, *Astr. Ap.*, **55**, 421.

van Driel, W 1987, Ph.D. Dissertation (University of Gronigen).

Verter, F. 1983, Ph. D. Dissertation (Princeton University).

Viallefond, F. and Thuan, T.X. 1983, *Ap.J.*, **269**, 444.

Waller, W.H. 1988, Ph.D. Dissertation (University of Massachusetts).

Wevers, B.M.H.R. 1984, Ph.D. Dissertation (University of Groningen).

Wynn-Williams, C.G. and Becklin, E.E. 1986, *Ap.J.*, **308**, 620.

Young, J.S., Freier, P.S., Waddington, C.J., Brewster, N.R., and Fickle, R.K. 1981, *Ap.J.*, **246**, 1014.

Young, J.S., Gallagher, J.S., and Hunter, D.A. 1984, *Ap.J.*, **276**, 476.

Young, J.S., Kenney, J.D., Tacconi, L., Claussen, M.J., Huang, Y-L, Tacconi-Garman, L., Xie, S., and Schloerb, F.P. 1986b, *Ap.J.(Lett.)*, **311**, L17.

Young, J.S., Schloerb, F.P., Kenney, J., and Lord, S.D. 1986a, *Ap.J.*, **304**, 443.

Young, J.S. and Scoville, N.Z. 1982a, *Ap.J.*, **258**, 467.

_____. 1982b, *Ap.J. (Lett.)*, **260**, L11.

_____. 1984, *Ap.J.*, **287**, 153.

Young, J.S., Scoville, N.Z., and Brady, E. 1985, *Ap.J.*, **288**, 487.

Young, J.S., Xie, S., Kenney, J.D., and Rice, W.L. 1987, *in preparation.*